An In Silico Imaging Framework for Microstructure-Sensitive Myocardial Diffusion Weighted MRI

Mojtaba Lashgari

University of Leeds

School of Computing

Submitted in accordance with the requirements for transfer to the degree of

Doctor of Philosophy

August, 2023

This thesis is dedicated to my beloved wife, Narges, and my parents.

Declaration of Academic Integrity

The author attests that the work presented in this thesis is solely their own, except for any contributions made as part of jointly authored publications that have been included. The author also confirms that they have provided proper credit to the work of others where referenced within the thesis. The respective contributions of both the author and any other contributors to this work have been clearly indicated as follows.

All of the publications listed in this section were primarily authored by me. I was responsible for designing the study and writing the manuscript, which involved analyzing and discussing the results. Additionally, I wrote the code for analyzing the data, and I carried out the data processing, statistical analysis, and experiments. While the other authors assisted me in designing the study and their contributions mainly centered around discussing the results and reviewing the manuscript.

- Lashgari, Mojtaba, et al. "Three-dimensional micro-structurally informed in silico myocardium–Towards virtual imaging trials in cardiac diffusion-weighted MRI." Medical Image Analysis 82 (2022): 102592.
- Lashgari, Mojtaba, et al. "Myocardium numerical phantom at microscale: application in MRI simulation." ESMRMB 2021 Online 38th Annual Scientific Meeting.
- Lashgari, Mojtaba, et al. "SpinDoctor-IVIM: A virtual imaging framework for intravoxel incoherent motion MRI." submitted to a journal.

Acknowledgements

It is my pleasure to begin this thesis by expressing my deep gratitude to my supervisory team for their invaluable guidance and support throughout my PhD journey. I am fortunate to have had the opportunity to work with a team of exceptional scholars who have provided me with the necessary tools, resources, and guidance to succeed in my research.

First and foremost, I would like to thank my primary supervisor, Professor Alejandro F Frangi, for his exceptional mentorship and guidance. His extensive knowledge, expertise, and insights in the field have been instrumental in shaping my research questions and methodologies.

I would also like to express my appreciation to my co-supervisor, Professor Jurgen E Schneider, for his invaluable contributions to my research. His feedback and guidance have been invaluable in my accomplishment.

Furthermore, I am grateful to the other members of my supervisory team, Dr Nishant Ravikumar and Dr Irvin Teh, for their contributions to my research by providing feedback, guidance, and support throughout my PhD program.

I would like to take this opportunity to thank Marie Sklodowska-Curie Actions for awarding me the PhD scholarship that has enabled me to pursue my academic aspirations. The scholarship has been a life-changing opportunity for me, and I am deeply grateful for the support and resources that it has provided.

Finally, I would like to express my deepest gratitude to my beloved wife Narges. Her patience, understanding, and unwavering belief in me have been instrumental in enabling me to pursue my academic goals. Despite the many challenges that we faced as a family, she has always been my rock, providing me with the necessary emotional support and motivation to push through difficult times. I am deeply grateful to my parents for their unwavering support, encouragement, and love throughout my PhD journey. Their support has been a constant source of motivation for me, and I am indebted to them for their sacrifices and commitment to my success.

Abstract

Cardiovascular diseases (CVDs) are a major global health concern, responsible for more than a quarter of annual deaths (around 17.5 million). Non-invasive dMRI models, like apparent diffusion coefficient and diffusion tensor imaging, can assess changes in the myocardium due to CVDs. However, these models lack biophysical interpretations preferred by clinicians. To address this, biophysical models are being developed to better understand the myocardium's microstructure. A virtual imaging framework is essential to validate these models and analyze dMRI sensitivity to microstructural changes.

In this thesis, we present a virtual imaging framework to simulate dMRI signals in cardiac microstructure and microvasculature. The framework includes a numerical phantom mimicking cardiac microstructure and a solver for the generalized Bloch-Torrey equation, termed SpinDoctor-IVIM.

With the first objective, the morphometric study found no significant difference ($p > 0.01$) between the volume, length, and primary and secondary axes of the simulated and real cardiomyocyte data from the literature. Structural correlation analysis confirmed that the *in-silico* tissue shows a similar disorderliness as the real tissue. The absolute angle differences between the simulated helical angles (HA) and the input HA of the cardiomyocytes ($4.3^\circ \pm 3.1^\circ$) closely match the angle differences reported in previous studies using experimental cardiac diffusion tensor imaging (cDTI) and histology ($3.7^\circ \pm 6.4^\circ$) and ($4.9^\circ \pm 14.6^\circ$).

With the second objective, the SpinDoctor-IVIM stands out for accounting for volumetric microvasculature during blood flow simulations, incorporating diffusion phenomena in the intravascular space, and considering permeability between the intravascular and extravascular spaces, providing more accurate and comprehensive results.

Overall, this thesis contributes valuable insights into the microstructure and microvasculature of the myocardium, offering promising advancements in studying CVD using dMRI. The developed virtual imaging framework is a crucial step towards improving cardiac research based on dMRI.

Contents

List of Figures

List of Tables

Abbreviations

AD	Axial diffusivity
ADC	Apparent diffusion coefficient
CISTIB	Computational imaging and simulation technologies in biomedicine
CMs	Cardiomyocytes
CVDs	Cardiovascular diseases
D	Diffusivity
dMRI	Diffusion Magnetic Resonance Imaging
DTI	Diffusion Tensor Imaging
EC	Extracellular
ECM	Extracellular matrix
Endo	Endocardium
Epi	Epicardium
FA	Fractional anisotropy
FEM	Finite element method
HC	Hypertrophic Cardiomyopathy
HH	Hypertensive Hypertrophy
IC	Intracellular
ICDs	Intercalated discs
IVIM	Intravoxel Incoherent Motion
LICAMM	Leeds Institute of Cardiovascular and Metabolic Medicine
LL	Lower layer
MC	Monte Carlo
MD	Mean diffusivity
MI	Myocardial Infarction
MRI	Magnetic Resonance Imaging
NMR	Nuclear Magnetic Resonance
PDE	Partial Differential Equation
PGSE	Pulsed Gradient Spin Echo
RF	Radio Frequency
SE	Spin Echo
SNR	Signal noise ratio
UL	Upper layer

Chapter 1 : Introduction

1.1 Chapter summary

In chapter 1, the motivation for this project is explained, including the clinical importance of cardiac microstructure imaging (1.2.1), the role of diffusion MRI (dMRI) in cardiac microstructure imaging, as well as how modern virtual frameworks can be used to facilitate developing and validating novel techniques for cardiac microstructure imaging using dMRI models (1.2.2). Additionally, this chapter describes the problem that this project seeks to address and the specific ways in which it will do so in 1.3.

1.2 Motivation

1.2.1 Confronting Cardiovascular Disease

Cardiovascular diseases (CVDs) are a significant global health concern that account for more than one-quarter of all global deaths each year ($\sim$ 17.5 million) Ezzati et al. [2015]. Many CVDs such as hypertrophic cardiomyopathy (HC), myocardial infarction (MI), and hypertensive hypertrophy (HH) are accompanied by physical changes to the microstructure of the myocardium. These changes are called myocardial remodelling and fall under different categories, as suggested by Bates [2016]:

1. Myocardial disarray is the first class of myocardial remodelling where a normal arrangement of cardiomyocytes (CMs) is disorganised. This is common in HC and HH;

2. Fibrosis is the second class of myocardial remodelling, characterised by collagen replacing CMs, and is found in HC, MI, and HH;

3. The last type of remodelling includes capillaries, where the ratio between the external and internal lumen diameters of capillaries increases.

Therefore, exploring changes in the myocardial microstructure is crucial for both finding a diagnostic marker of diseases and also measuring treatment response to various therapies. However, traditional invasive procedures used to assess tissue microstructure

through biopsy and histology, which currently are the standard diagnosis routine for most tissues, cannot be employed on the myocardial tissue. The use of non-invasive diffusion magnetic resonance imaging (dMRI) techniques to study microstructural changes in myocardium has become increasingly popular in order to understand how these changes occur during the onset and progression of different types of cardiac pathology Mekkaoui et al. [2017], Nielles-Vallespin et al. [2019].

1.2.2 Cardiac Microstructure Assessment via dMRI

dMRI techniques based-on Brownian motion of water molecules

dMRI is a physical measurement of the stochastic motion (Brownian motion) of water molecules. During a typical magnetic resonance diffusion measurement, i.e., with diffusion times of 10-100 ms, water molecules diffuse around 4-20 µm within the soft tissues with a diffusivity of $D = 1.5\,\mu m^2/ms$ Yu et al. [2017]. However, the motion of water molecules is hindered and restricted in the cellular environment (Figure 1.1, cell level). This creates the opportunity to investigate tissues at the microscale, enabling a more in-depth study of pathological processes.

Apparent diffusion coefficient (ADC) was the first dMRI metric which served as a gold standard for detecting brain strokes and ischemia Le Bihan and Breton [1985]. Later, in 1994, Basser et al. [1994] proposed diffusion tensor imaging (DTI) to quantify the anisotropy of water diffusion in *in-vivo* biological tissues. Thus far, dMRI has found widespread application in studies on neurodevelopmental disorders, neurodegeneration, and other neurological disorders Tae et al. [2018]. More recently, the application of dMRI models in cardiology has gained the attention of clinicians and biomedical researchers Mekkaoui et al. [2017], Nielles-Vallespin et al. [2019].

ADC, DTI, and diffusion kurtosis imaging are the most prominent dMRI phenomenological models that reveal non-invasively some cumulative information about the tissue microstructure. However, these models do not provide biophysical interpretations of the dMRI signal, which clinical experts or cardiologists would prefer, in order to leverage the extracted information for diagnosis and clinical decision-making. The lack of phenomenological models to characterize the biophysical parameters of the cells calls the attention of researchers to develop biophysical models that could be used to probe the underlying microstructure of the myocardium. This is enabled by the fact that biophysical models are formulated based on certain approximations and assumptions,

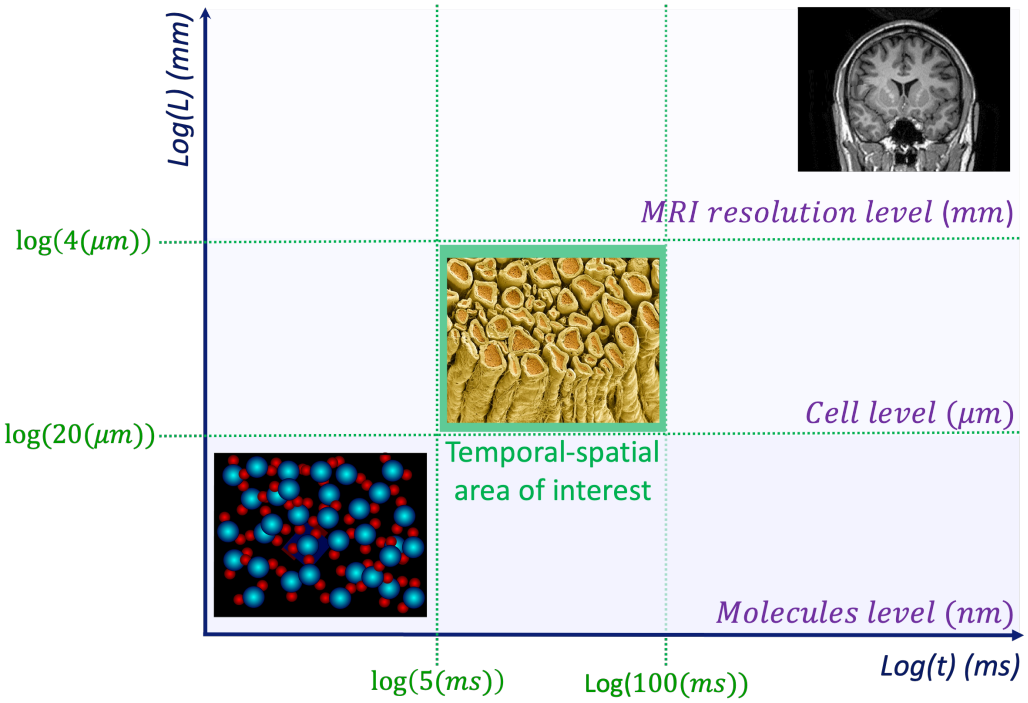

Figure 1.1: Accessing microstructure of tissue (cell level), an intermediate level between MRI resolution and molecules levels, at the typical resolution of MRI scanner, at the range of diffusion encoding time. Image with permission Novikov et al. [2016]

derived from biological information of the underlying tissue structure, in order to interpret dMRI signals. Therefore, there is currently a strong demand for the generation of both physical and numerical cardiac phantoms, in order to validate these assumptions and approximations. Nevertheless, few studies have explored the benefits and challenges associated with designing virtual framework for the cardiac dMRI. First part of this work aims to develop a workflow to generate a novel numerical phantom representing myocardial microstructure. Compared with previous efforts, the proposed framework introduces two main novel contributions:

1. it considers more realistic shapes for the CMs and consequently a realistic complexity for the medium (relative to previous phantoms), by incorporating the native probability density functions (PDFs) of CM shape parameters into the numerical phantom.

2. it takes into account the effects of water exchange through the intercalated discs

(ICDs) within the phantom on the dMRI signal.

dMRI techniques based-on both Brownian and transitional motions of water molecules

Recent years have seen a surge in use of MRI-based perfusion imaging to assess tissue microvasculature due to its non-irradiating process and superior signal-to-noise ratio (SNR) compared to computed tomography Demeestere et al. [2020]. The most common techniques for perfusion imaging using MRI are dynamic susceptibility contrast imaging, dynamic contrast-enhanced MR imaging, and arterial spin labelling. However, these imaging techniques have a number of limitations including ambiguity in the interpretation of their predictions, a high SNR requirement, limited accessibility to suitable agents, and limited spatial-temporal resolution that impede their use and implementation in clinical settings Karampinos et al. [2010], Mou et al. [2017], Spinner [2019]. In light of the limitations of conventional MRI-based perfusion imaging techniques, intravoxel incoherent motion (IVIM) MRI, due to its endogenous nature, is gaining more attention in the clinical setting. IVIM MRI is a dMRI-based technique that allows blood perfusion assessment of the tissue Zhu et al. [2020]. IVIM refers to the transitional displacement of the water molecules' spins through microvasculature within an MRI voxel during the measurement time Le Bihan [2019]. Consequently, IVIM MRI is based on the fact that blood magnetization is dephased in the presence of diffusion-encoding gradients due to non-coherent blood flow in the microvascular network Le Bihan et al. [1986].

Being an endogenous contrast technique, providing local information about perfusion (excitation and readout are carried out in the same plane), and providing information about tissue microstructure (through the diffusion of water molecules in the extra-vascular space) in addition to perfusion, are the main advantages of IVIM MRI that make it suitable for clinical use Federau [2017]. For instance, recent literature on IVIM MRI has revealed the feasibility of in vivo implementation of IVIM MRI using the current clinical setting Federau et al. [2014b], Iima and Le Bihan [2016]. Furthermore, previous studies have indicated that IVIM MRI is sufficiently sensitive to capture physiological and drug-induced changes in tissue perfusion Federau [2017].

Despite the *in-vivo* implementation of cardiac IVIM MRI Callot et al. [2003], Delattre et al. [2012], Moulin et al. [2016], because of the small volume fraction of the

capillaries and cardiac motion, the reliability of IVIM MRI information in the *in-vivo* heart is challenging. Consequently, uncertainties remain regarding the exact relationship between the parameters of IVIM MRI i.e., pseudo-diffusion and perfusion fractions, and tissue perfusion. Therefore, there is abundant interest in research to advance our understanding of the sensitivity of IVIM MRI parameters to biophysical features of microvasculature and imaging protocol. In addition, there is interest in investigating the feasibility of estimating microvascular biophysical parameters from IVIM MRI measurement. Finally, discovering the exact role of other sources of IVIM, such as arterioles/venules, and other fluid flows like brain cerebrospinal fluid on top of capillaries, which are not fully understood, is of particular interest.

Similar to cardiac dMRI techniques based-on Brownian motion, only a few studies have shed light on the potential of virtual frameworks to improve the interpretation of IVIM MRI signals, and analyse the sensitivity of IVIM MRI to changes in myocardial microvasculature and use of different pulse sequences Spinner et al. [2019]. Therefore, use of virtual frameworks is essential as they provide full control over the structure of microvasculature and extravascular compartments, alongside imaging protocols Fieremans and Lee [2018]. Hence, the second part of this work aims to develop an efficient virtual framework to aid in creating, evaluating, and optimizing cardiac IVIM MRI. However, in this part, no attempt is made to develop a numerical phantom for the cardiac microvasculature due to practical constraints for the development and assessment of the numerical phantom of the myocardial microvasculature.

1.3 Aim and objectives

We discussed in 1.2.2 that a virtual imaging framework is necessary for studying microstructures of the myocardium with dMRI. With this framework, the microstructure of the myocardium will be represented realistically using a numerical phantom along with a numerical solver that simulates dMRI by considering both Brownian and transitional motions. Such a framework comprises two core components, numerical phantom and dMRI simulator as shown in Figure 1.2.

The development of numerical phantoms is dependent upon the availability of a numerical simulator for evaluating the performance and accuracy of the phantom. It is important to compare the simulated signal derived from numerical phantoms with the signal coming from *in-vivo* and *ex-vivo* in order to assess the performance of the

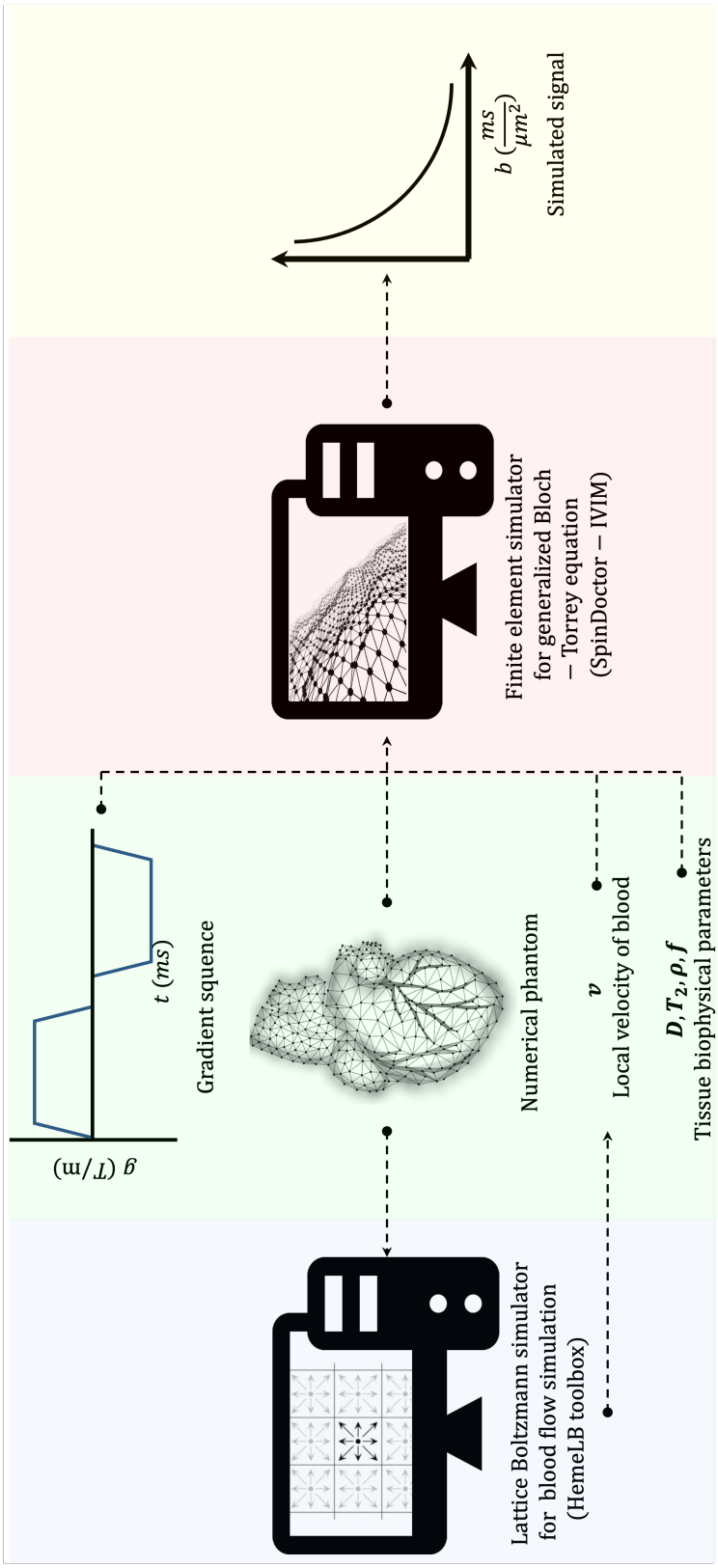

Figure 1.2: Schematic diagram of a virtual cardiac diffusion magnetic resonance imaging.

numerical phantom. Hence, in the absence of a simulator capable of incorporating the incoherent motion of water molecules through the microvasculature and detailed information about the structure of cardiac microvasculature, two objectives were considered for this thesis:

1. First, I develop an algorithm to generate a more realistic numerical phantom of myocardium tissue that considers the microstructural and biophysical features of the myocardial tissue.

2. The second objective of this thesis is the development of a FE solver for IVIM MRI. To accomplish this, a FE solver is extended that accounts for both Brownian and transitional motions. This FE solver is capable to solve the generalized Bloch-Torrey equation and can be used to solve any other type of microvasculature.

Chapter 2 : Background

2.1 Chapter summary

This chapter explains the primary concepts required to understand dMRI and dMRI simulation in following order: Section 2.2 introduces the nuclear magnetic resonance (NMR) principle; Section 2.2.2 and 2.3 explains the relevant terminology of MRI and dMRI, respectively. In addition, sections 2.4, 2.5, and 2.6 describe the generalised Bloch-Torrey equation, intra-voxel incoherent motion imaging, and Navier-Stokes equation, respectively. Section 2.7 ends this chapter with a short description about the available approaches for dMRI simulation.

2.2 Magnetic Resonance Imaging

2.2.1 Nuclear Magnetic Resonance Principle

MRI is a non-invasive medical imaging modality that enables us to acquire detailed information of internal structures in the body. It does this by employing the NMR characteristic of hydrogen atoms, the most predominant element in water and fatty tissues within the body. NMR characteristic of hydrogen atoms originate from single proton hydrogen nuclei that causes non-zero nuclear spin angular momentum of the hydrogen nuclei. The spin is a quantum mechanics quantity of nuclei without classical physical interpretation. But, in a simplistic view, it is assumed as a self-rotation element as illustrated in Figure 2.1 [1].

These spins can make a net magnetization vector, however, as illustrated in Figure 2.2 [2].a, due to arbitrary orientation of the spins, the net magnetization is zero. MRI using a strong and constant magnetic field, called main/external field $\mathbf{B}_0$, forces the spins to precess (i.e. rotate) relative to $\mathbf{B}_0$ with Larmor frequency, as shown in Figure 2.2.b.

[1] Image 2.1 was extracted http://www.pixelmeasure.io/pages/84/the-principles-of-magnetic-resonance-imaging

[2] Image 2.2 was extracted http://www.pixelmeasure.io/pages/84/the-principles-of-magnetic-resonance-imaging

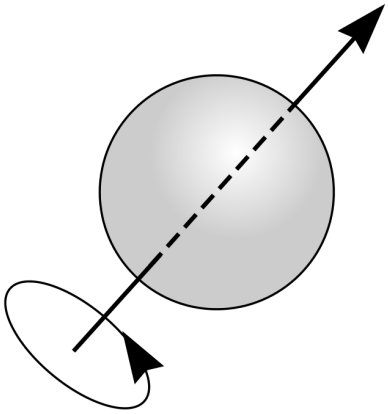

Figure 2.1: Simplified representation of a hydrogen nucleus as a spinning ball

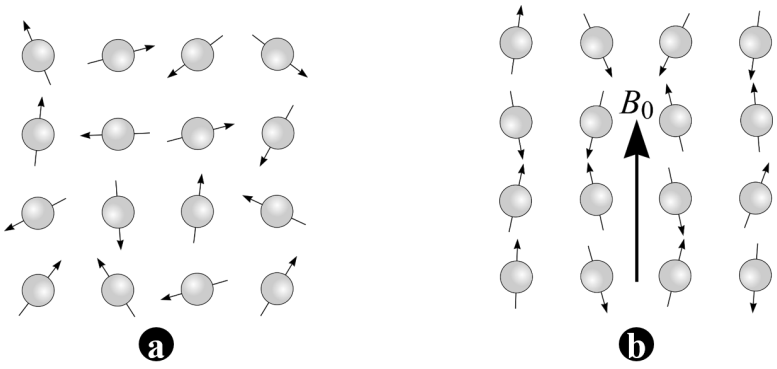

Figure 2.2: Schematic representation of spins orientation a) Arbitrary orientation of spins in absence of $\mathbf{B}_0$ b) Reorientation of spins around $\mathbf{B}_0$

Larmor frequency, w, is proportional to the external magnetic field:

$$w = \gamma B_0 \tag{2.1}$$

where γ is the gyromagnetic ratio of the nucleus, and B_0 is the intensity of the magnetic field.

After applying $\mathbf{B}_0$, spins precess with a direction parallel (upward) or anti-parallel (downward) to $\mathbf{B}_0$ direction (Figure 2.2.b). The energy level for upward spin is lower than that of downward, and a slightly larger proportion of spins precess with a direction parallel to $\mathbf{B}_0$. This state, when spins are aligned with the $\mathbf{B}_0$, is called equilibrium and net magnetization $\mathbf{M}_z$ is nonzero. By exposing energy, equal to the energy difference between energy level of upward and downward spins, the upward spins are excited and change their status to downward. This energy difference is proportional to w, which is in the range of radio frequencies (RF). Hence, in MRI, electromagnetic RF coils are used to excite proton spins. By applying an RF pulse with its magnetic field $\mathbf{B}_1$ perpendicular to $\mathbf{B}_0$ (Figure 2.3.a), the proportion of downward spins increases, resulting in a decrease of $\mathbf{M}_z$ (Figure 2.3.b). In addition, $\mathbf{B}_1$ makes spins to precess in phase (Figure 2.3.c) that generates a rotating transverse magnetization $\mathbf{M}_{xy}$ perpendicular to $\mathbf{B}_0$ (Figure 2.3.d).

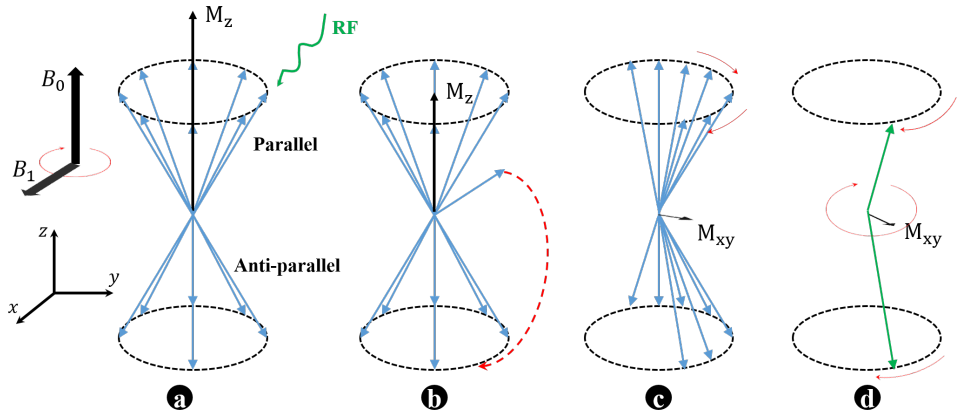

Figure 2.3: Spins excitation using RF pulse to generate transverse magnetization $\mathbf{M}_{xy}$. a) Applying RF pulse to the spins in the equilibrium status, b) immigration of spins from high level energy to low level and decrease in $\mathbf{M}_z$, c) rephasing of spins and increase in $\mathbf{M}_{xy}$ d) generating maximum $\mathbf{M}_{xy}$, rotating around $\mathbf{B}_0$.

After the RF is turned off, the immigrated spins to higher energy level, return to

the low energy level by emitting energy to the environment or to spins at lower energy level. The transferred energy to the environment increases $\mathbf{M}_z$, a process known as the spin-lattice relaxation. While, the transferred energy to other spins decreases $\mathbf{M}_{xy}$, as illustrated in Figure 2.4 [1], a process known as spin-spin relaxation.

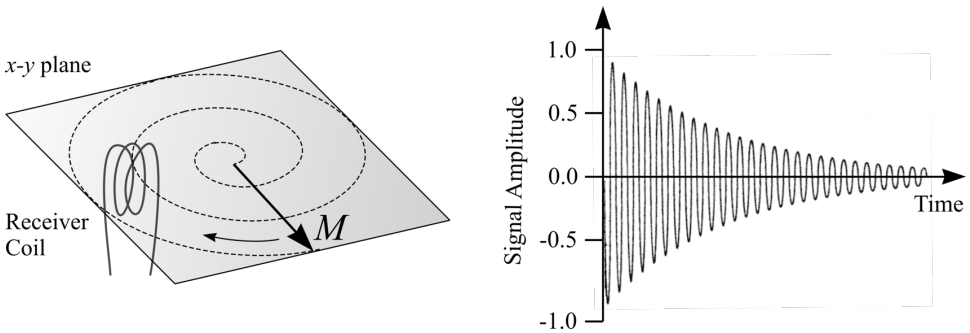

Figure 2.4: Effect of spin-spin relaxation in reducing intensity of $\mathbf{M}_{xy}$ and induced signal into a receiver coil.

Due to the difference in relaxation mechanisms, the RF emission from these mechanisms occur over different durations. Recovery of $\mathbf{M}_z$ to 63% of its primary value, is characterized by the relaxation time T_1. While the decrease of $\mathbf{M}_{xy}$ to 37% of its maximum value, is characterized by the relaxation time T_2.

2.2.2 Image Formation

To reconstruct an MRI image, the signal received by RF receiver coil must be encoded at different spatial locations. Hence, magnetic field gradients (pulse sequence) are employed to encode the spins spatially, as illustrated in Figure 2.5.a. When a part of body is put into an MRI scanner, all the spins in that part of body precess with the same w, and all of them are excited by the RF pulses at the same time. Therefore, to image a specific 2D slice from a desired transverse section of a body (e.g. Figure 2.5.b), a slice selecting gradient $\mathbf{G}_{ss}$, illustrated in Figure 2.5.a second line, is superimposed on the $\mathbf{B}_0$. Then, when an RF pulse is applied with the following frequency,

$$w_{RF} = \gamma(B_0 + G_{ss}z) \tag{2.2}$$

[1] Image 2.1 was extracted http://www.pixelmeasure.io/pages/84/the-principles-of-magnetic-resonance-imaging

where z is the slice position along $\mathbf{B}_0$, only the spins in the related slice are excited and precess with w_{RF}, as depicted in Figure 2.5.c. Then, to encode spins of the different rows of the selected slice, with different precessing frequencies (Figure 2.5.d), a frequency encoding gradient $\mathbf{G}_f$ along the x axis is superimposed on $\mathbf{B}_0$ (Figure 2.5.a third line). Finally, to encode each column of the selected slice with different precessing phases (Figure 2.5.e), phase encoding gradient $\mathbf{G}_p$, in Figure 2.5.a fourth line, is applied for a short time along the y axis. The intensity of $\mathbf{G}_p$ varies in the different signal acquisition (Figure 2.5.a fourth line), and the measured signals for all $\mathbf{G}_p$ repetitions are saved in a matrix known as the k-space (Fourier transform of the image), as shown in Figure 2.5.f. Finally, as depicted in Figure 2.5.g, an MRI image is reconstructed by applying the inverse Fourier transform to the k-space.

2.3 Diffusion Principle

The stochastic motion of water molecules within a medium is called Brownian motion (mostly known as diffusion in NMR field), described by Robert Brown in 1828. Einstein described the mean square displacement of water molecules, $\langle r^2 \rangle$, that diffuse freely during a diffusion encoding time, t, as

$$\langle r^2 \rangle = 2Dt \tag{2.3}$$

where D is the diffusion coefficient Einstein [1905].

2.3.1 Diffusion MRI

Microstructure and microvasculature of tissues restrict and hinder the movement of water molecules and change their behaviour in comparison with free diffusion status. By sensitizing MR signals to the movement of water molecules, microstructure and microvasculature information of a tissue are included within MR signals. This sensitization is done by applying diffusion encoding gradients. The diffusion encoding gradients relate the measured signal to water displacement, in the direction of encoding gradients.

Pulsed gradient spin echo (PGSE) is a common sequence that is used in dMRI for sensitizing MR signal to displacement of water molecules. Figure 2.6, illustrates the PGSE sequence which consists of a 90° RF pulse, two diffusion-sensitizing gradients—two rectangular with a duration time of δ and separated by time Δ —before and

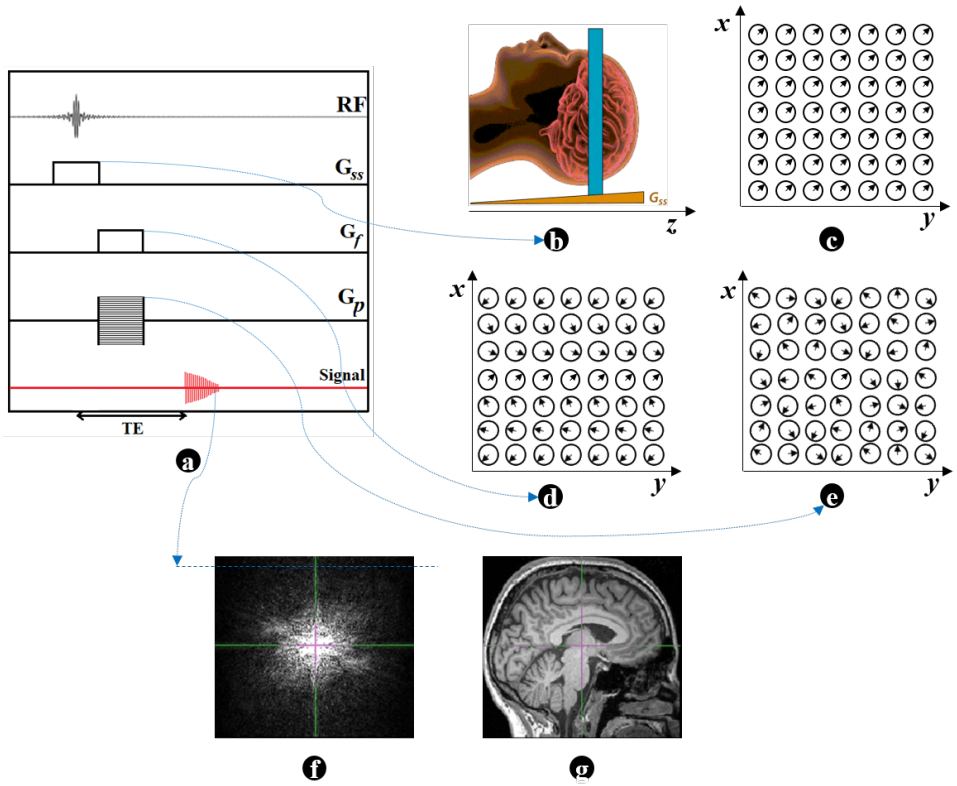

Figure 2.5: MRI space encoding and 2D image reconstruction. a) shows a schematic representation of the RF pulse and gradients for slice selection ($\mathbf{G}_{ss}$), frequency-encoding ($\mathbf{G}_f$) and phase-encoding ($\mathbf{G}_p$) used on gradient-echo sequences. b) selecting a slice of brain along z axis, c) precession of spins in the selected slice after applying $\mathbf{G}_{ss}$, d) precession of spins in the selected slice after applying $\mathbf{G}_f$, e) precession of spins in the selected slice after applying $\mathbf{G}_f$, f) k-space formation by increasing $\mathbf{G}_p$ repeatedly, g) MR image formation by applying inverse of Fourier transform to the k-space.

after a 180° RF pulse.

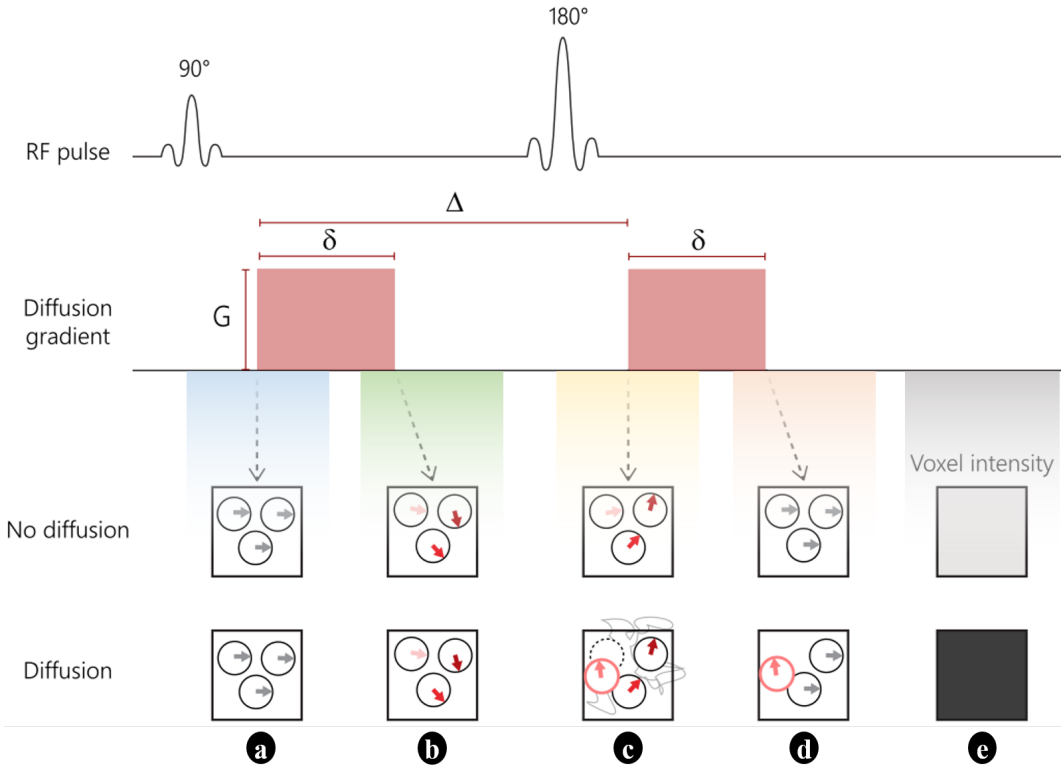

Figure 2.6: PGSE sequence. Each row, from top to bottom, shows 90° and 180° RF pulses, diffusion encoding gradients, a pack of static spins, and a pack of diffusing spins, respectively. a) $\mathbf{M}_{xy}$ in the transverse plane after 90° RF pulse, b) spins phase shift after first diffusion gradient, c) flipping polarity after 180° RF pulse, d) reversed phase shift after second diffusion gradient, e) signal loss for diffusing spins compare with static spins. Image with permission Grisot [2019]

First, 90° RF generates $\mathbf{M}_{xy}$ in the transverse plane (Figure 2.5.a). Then, when the first gradient is applied, the spins at different locations along the gradient direction, e.g. $\mathbf{x}$, experience a phase shift ϕ_1 (Figure 2.5.b), Eq. (2.4), and start to *dephase*.

$$\phi_1 = \gamma \delta G_x x_1 \tag{2.4}$$

After flipping the polarity using a 180° RF pulse (Figure 2.5.c), spins experience reversed phase shift ϕ_2 ((Figure 2.5.d)), Eq. (2.5), and start to *rephase*.

$$\phi_2 = -\gamma\delta G_x x_2 \tag{2.5}$$

net phase of the spins ϕ after the second gradient is equal to

$$\phi = \phi_1 + \phi_2 = \gamma\delta G_x(x_1 - x_2) = -qr \tag{2.6}$$

where $q = \gamma G\delta$. If the spins do not move, their positions are the same during application of the two gradients i.e. $x_1 = x_2$, therefore, their phase shift are cancelled ($\phi = 0$). However, if the spins move, their positions are not the same during application of the two gradients i.e. $x_1 \neq x_2$, resulting in a residual phase shift ($\phi \neq 0$) and signal loss (Figure 2.5.e, signal intensity for moving spins is lower than static spins), consequently. Stejskal and Tanner showed that the measured dMRI signal for free water diffusion can be described as follow Stejskal and Tanner [1965]:

$$\frac{S(b)}{S_0} = \exp(-bD) \tag{2.7}$$

where S_0 is the amplitude MR signal without the presence of diffusion gradient, and b is an effective parameter of a diffusion sequence, termed *b-value*:

$$b = (q)^2(\Delta - \frac{\delta}{3}) = (\gamma G\delta)^2(\Delta - \frac{\delta}{3}) \tag{2.8}$$

First application of dMRI proposed by Le Bihan et al., where they did curve fitting Eq. (2.9) on the diffusion signal acquired by a PGSE sequence. They used ADC instead of D to represent restricted diffusion Le Bihan et al. [1986], as diffusion of water in biological tissues may differ from the true diffusion coefficient due to tissue microstructure and/or existence of multi compartments with the different diffusivities:

$$\frac{S(b)}{S_0} = \exp(-bADC) \tag{2.9}$$

2.3.2 Diffusion Tensor Imaging

DTI is the first method that enabled us to measure anisotropy of water diffusion in tissues. The diffusion process in a homogeneous medium is characterized by the scalar D. However, in an inhomogeneous medium like biological tissues, the diffusion has a directional preference, termed *anisotropy*, that is specific to the microstructure of tissue. Consequently, a description of diffusion anisotropy is provided by a rank-2 tensor $\mathbf{D}$ as,

$$\mathbf{D} = \begin{bmatrix} D_{xx} & D_{xy} & D_{xz} \\ D_{yx} & D_{yy} & D_{yz} \\ D_{zx} & D_{zy} & D_{zz} \end{bmatrix} \tag{2.10}$$

where D_{xx}, D_{yy}, and D_{zz} characterize diffusion along x, y, and z axes, while the off-diagonal elements characterize the correlation of diffusion in different directions, and are symmetric (i.e. $D_{ij} = D_{ji}$). The six unknown elements of $\mathbf{D}$ and S_0 can be estimated using a diffusion measurement in at least 6 gradient directions and a measurement required with $b = 0$ ($\frac{s}{mm^2}$) Basser et al. [1994].

After estimation of $\mathbf{D}$, it can be decomposed to:

$$\mathbf{D} = \begin{bmatrix} e_1 & e_2 & e_3 \end{bmatrix} \begin{bmatrix} \lambda_1 & 0 & 0 \\ 0 & \lambda_2 & 0 \\ 0 & 0 & \lambda_3 \end{bmatrix} \begin{bmatrix} e_1 \\ e_2 \\ e_3 \end{bmatrix} \tag{2.11}$$

where (e_1, e_2, e_3), and $(\lambda_1, \lambda_2, \lambda_3)$ are three eigenvectors and eigenvalues, respectively.

After computing eigenvalues, some scalar quantitative metrics are derived from them to describe different aspects of the tensor.

Mean diffusivity (MD) in Eq. (2.12) describes the average of the eigenvalues; fractional anisotropy (FA) in Eq. (2.13) describes the degree of anisotropy in the tensor; axial diffusivity (AD) in Eq. (2.14) describes the mean diffusivity parallel to the axis of main diffusion; and radial diffusivity (RD) in Eq.(2.15) describes the mean diffusivity perpendicular to the axis of main diffusion Basser et al. [1994].

$$MD = \frac{\lambda_1 + \lambda_2 + \lambda_3}{3} \tag{2.12}$$

$$FA = \sqrt{\frac{(\lambda_1 - \lambda_2)^2 + (\lambda_2 - \lambda_3)^2 + (\lambda_3 - \lambda_1)^2}{2(\lambda_1^2 + \lambda_2^2 + \lambda_3^2)}} \tag{2.13}$$

$$AD = \lambda_1 \tag{2.14}$$

$$RD = \frac{\lambda_1 + \lambda_2}{2} \tag{2.15}$$

2.4 Generalized Bloch-Torrey equation

The transverse magnetization signal can be mathematically described with the Bloch-Torrey (BT) equation, Eq. (2.17), that relates the temporal and spatial evolution of the transverse magnetisation $M(\boldsymbol{r},t)$ to diffusion $D(\boldsymbol{r})$, spin-spin relaxation T_2, and the time-varying magnetic field gradient $f(t)\boldsymbol{g}\cdot\boldsymbol{r}$, where $f(t)$ is effective time profile (e.g. Eq. (2.16) is PGSE time profile) and $\boldsymbol{g}$ contains the amplitude and directional information of the magnetic field gradient.

$$f(t)=\begin{cases}1, & t_1\le t\le t_1+\delta,\\ -1, & t_1+\Delta\le t\le t_1+\Delta+\delta,\\ 0, & otherwise,\end{cases} \tag{2.16}$$

Let Ω be the observation domain, comprising L sub-domains, such that $\cup_{l=1}^{L}\Omega_l$. Also, let Γ_l^e be the external boundary of Ω_l, and Γ_{ln} the boundary between Ω_l and Ω_n. Then, the evolution of the complex transverse magnetisation is described by

$$\frac{\partial}{\partial t}M_l(\boldsymbol{r},t)=\nabla\cdot(D_l(\boldsymbol{r})\nabla M_l(\boldsymbol{r},t))-\frac{1}{T_{2l}}M_l(\boldsymbol{r},t)-i\gamma f(t)\boldsymbol{g}\cdot\boldsymbol{r}M_l(\boldsymbol{r},t)\quad(\boldsymbol{r}\in\Omega_l), \tag{2.17}$$

subject to the boundary conditions

$$D_l(\boldsymbol{r})\nabla M_l(\boldsymbol{r},t).\boldsymbol{n}_l(\boldsymbol{r})=k_{ln}(M_n(\boldsymbol{r},t)-M_l(\boldsymbol{r},t))\quad(\boldsymbol{r}\in\Gamma_{nl},\forall n), \tag{2.18}$$

$$D_l(\boldsymbol{r})\nabla M_l(\boldsymbol{r},t).\boldsymbol{n}_l(\boldsymbol{r})=-k_l^e M_l(\boldsymbol{r},t)\quad(\boldsymbol{r}\in\Gamma_l^e), \tag{2.19}$$

and the initial condition

$$M_l(\boldsymbol{r},0)=\rho_l(\boldsymbol{r}), \tag{2.20}$$

where $t\in[0,T_E]$ with T_E echo time, $\boldsymbol{n}_l(\boldsymbol{r})$ is the unitary outward pointing normal to Ω_l, k_{ln} (k_l^e) is the permeability constant in Γ_{ln} (Γ_l^e). Also, the same permeability is assumed in both directions of the membrane, i.e $k_{ln}=k_{nl}$. The generalized form of BT (gBT) equation is defined by factoring velocity of flow $\boldsymbol{v}(\boldsymbol{r},t)$ in the media into the Eq.

(2.17)

$$\begin{aligned}\frac{\partial}{\partial t}M_l(\boldsymbol{r},t) &= \nabla\cdot(D_l(\boldsymbol{r})\nabla M_l(\boldsymbol{r},t)) - \frac{1}{T_{2l}}M_l(\boldsymbol{r},t)\\ &\quad - i\gamma f(t)\boldsymbol{g}\cdot\boldsymbol{r}M_l(\boldsymbol{r},t) - \boldsymbol{v}(\boldsymbol{r},t)\cdot\nabla M_l(\boldsymbol{r},t)\\ &\quad (\boldsymbol{r}\in\Omega_l),\end{aligned} \tag{2.21}$$

2.5 Intravoxel incoherent imaging

IVIM refers to the transitional displacement of the water molecules' spins within an MRI voxel during the measurement time which leads to a distribution of spins' speeds in orientation and/or amplitude Le Bihan [2019]. This distribution originates from the blood flowing within a microvascular network, shown in Figure 2.7.a, and mimics a pseudo-diffusion process.

The IVIM theory, introduced by Le Bihan et al. [1986], states that the incoherent blood flow in microvasculature leads to a dephasing of the spins in blood when diffusion gradients are applied, according to the formula:

$$\frac{S}{S_0} = (1-f)e^{-bD} + fe^{(-b(D+D^*))} \tag{2.22}$$

where f is perfusion fraction, D is diffusion coefficient, and D^* is pseudo-diffusion coefficient. As depicted in Figure 2.7.b, the pseudo-diffusion process results in a fast dMRI signal decay in presence of the diffusion encoding gradients Jerome et al. [2021].

2.6 Navier-Stokes equation

Given the viscoelastic properties of the blood flow, it is considered as an incompressible non-Newtonian flow Baieth [2008]. The flow of incompressible and non-Newtonian fluid in an observation domain of Ω is governed by the Navier-Stokes equations, Eq(2.23), where $\boldsymbol{v}(\boldsymbol{r},t)$ is flow velocity, ϑ is a viscosity parameter, and $P(\boldsymbol{r},t)$ is the pressure.

$$\begin{aligned}&\rho\Big(\frac{\partial}{\partial t}\boldsymbol{v}(\boldsymbol{r},t) + \big(\boldsymbol{v}(\boldsymbol{r},t)\cdot\nabla\big)\boldsymbol{v}(\boldsymbol{r},t)\Big) = \vartheta\Delta\boldsymbol{v}(\boldsymbol{r},t) + \nabla P(\boldsymbol{r},t)\\ &(\boldsymbol{r}\in\Omega),\end{aligned} \tag{2.23}$$

$$\nabla\cdot\boldsymbol{v}(\boldsymbol{r},t) = 0 \qquad (\boldsymbol{r}\in\Omega), \tag{2.24}$$

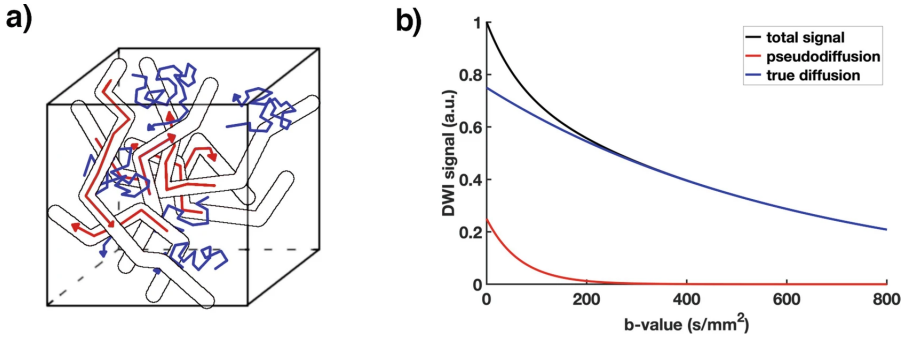

Figure 2.7: The IVIM model is represented schematically in (a), which shows the transitional movement of water molecules (coloured red) in the intravascular space and the Brownian movement of water molecules (coloured blue) in the extravascular space in a voxel of tissue. (b) illustrates the contributions of these movements to the observed dMRI signal decay, where the pseudo-diffusion caused by the transitional movement of water molecules contributes to a substantially faster decay compared to the diffusion caused by Brownian motion of water molecules. This leads to the observation of pseudo-diffusion only at low b-values. The image used with permission Jerome et al. [2021].

subject to the boundary conditions

$$\boldsymbol{v}(\boldsymbol{r},t) = 0 \qquad (\boldsymbol{r} \in \Gamma_w), \tag{2.25}$$

$$P(\boldsymbol{r},t)\cdot\boldsymbol{n}(\boldsymbol{r}) - \frac{\vartheta}{\rho}\nabla\boldsymbol{v}(\boldsymbol{r},t)\cdot\boldsymbol{n}(\boldsymbol{r}) = P(\boldsymbol{r},t)\cdot\boldsymbol{n}(\boldsymbol{r}) \quad (\boldsymbol{r} \in \Gamma_i \cup \Gamma_o), \tag{2.26}$$

and the initial condition

$$\boldsymbol{v}(\boldsymbol{r},0) = 0, \tag{2.27}$$

where $\boldsymbol{r} \in \Gamma_w$, $\boldsymbol{r} \in \Gamma_i$, and $\boldsymbol{r} \in \Gamma_i$, respectively, are the wall, inlet and outlet portions of the vascular boundary domains.

2.7 Computational Modelling of Diffusion MRI

Computational models, using analytical or numerical approaches, allow simulating dMRI signals for more realistic biological structures. Moreover, they enable one to investigate more subtle questions like the effect of the interaction of water molecules

with boundaries in the dMRI signals. The result of this simulation can be employed to investigate the sensitivity of dMRI signals to biophysical changes due to CVDs and use different pulse sequences.

To the best of my knowledge, these numerical methods of analyzing dMRI physics fall into either particle-tracking-based or continuum-based numerical schemes. Monte Carlo (MC) and finite element methods (FEM) are the common particle-tracking-based or continuum-based numerical schemes, respectively, for analysing dMRI numerically. These schemes are elaborated in the following for this section. However, two other numerical schemes used for this purpose, which fall into the category of continuum-based methods, include the lattice Boltzmann and matrix formalism methods. Lattice Boltzmann method, developed by Guyer and McCall [2000], numerically simulates the time evolution of magnetisation in a porous medium. However, lattice Boltzmann methods suffer from imposing a constraint on the time step (typical of explicit schemes) and requiring derivation of special boundary conditions for the probability distribution functions to preserve the consistency and accuracy of the numerical scheme Naughton et al. [2020]. Matrix formalism is a semi-numerical approximation that tries to find solutions for the eigenfunctions of the diffusion propagator. Due to matrix implementation, matrix formalism is computationally fast Callaghan [1997], Drobnjak et al. [2011], Grebenkov [2010]. However pragmatically, it is limited to simple geometries to find eigenfunctions analytically.

2.7.1 Monte Carlo simulation

MC simulation is based on replicating the Brownian motion of a large number of particles. For this purpose, MC method simulates the movement of every particle separately, and then calculates the total phase shift ϕ for each particle as a function of the gradient strength and its location over every timestep, j:

$$\sum_{j=0}^{N} \phi_j = \sum_{j=0}^{N} \gamma \langle G(t_j), r(t_j) \rangle t \tag{2.28}$$

where N is the total number of time steps, $G(t_j)$ is the diffusion encoding gradient at timestep j, and $r(t_j)$ is the molecule position at timestep j. Given the employed imaging sequence, the diffusion gradient strength at the location of the molecule at each timestep was summed for the duration of the two pulses (for the second pulse a

negative sign is considered). The dMRI signal $\frac{S}{S_0}$ for M water molecules (to calculate the dMRI signal, only molecules that finished inside the defined domain are considered, $M \leq N$) for each gradient direction is

$$\frac{S}{S_0} = \frac{1}{M} \sum_{j=0}^{M} cos(\phi_j) \tag{2.29}$$

The versatility of MC simulations makes them a suitable tool for modeling dMRI, since they can handle any arbitrary substrate and MR pulse sequence. In addition, MC simulations are capable to incorporate semi-permeable membranes, membrane-particle interactions, and changes in T1, T2, and diffusivity over time and space. However, for complex substrates, MC simulation requires to simulate enough number of spins at enough discrete time points to properly repleacate the dynamics of spins ensemble through the pulse squence.

Smoldyn Andrews [2017], Camino Cook et al. [2006], Hall and Alexander [2009], MRISIMUL Xanthis et al. [2013], and DIFSIM Balls and Frank [2009] are the common MC toolboxes that enable one to accurately model the 3D diffusion of large numbers of particles within complex geometries.

2.7.2 Finite element solution of generalized Bloch-Torrey partial differential equation

The solution of gBT equation Eq.(2.21) requires to be twice differentiable, which restricts the solution's space. This condition is relaxed by working out a solution in the weighted residual sense. This solution satisfies

$$\begin{aligned}\frac{\partial}{\partial t}\int_{\Omega_l} v(\boldsymbol{r})M_l(\boldsymbol{r},t)\,d\boldsymbol{r} = &\int_{\Omega_l} v(\boldsymbol{r})\nabla\cdot(D_l(\boldsymbol{r})\nabla M_l(\boldsymbol{r},t))\,d\boldsymbol{r} - \frac{1}{T_{2l}}\int_{\Omega_l} v(\boldsymbol{r})M_l(\boldsymbol{r},t)\,d\boldsymbol{r} \\ &- i\gamma f(t)\int_{\Omega_l} v(\boldsymbol{r})\boldsymbol{g}\cdot\boldsymbol{r}M_l(\boldsymbol{r},t)\,d\boldsymbol{r} \\ &- \int_{\Omega_l} v(\boldsymbol{r})\boldsymbol{v}(\boldsymbol{r},t)\cdot\nabla M_l(\boldsymbol{r},t)\,d\boldsymbol{r} \\ &(\boldsymbol{r}\in\Omega_l),\end{aligned} \tag{2.30}$$

valid for $\boldsymbol{r} \in \Omega_l (l = 1, ..., L)$, and for all functions $v(\boldsymbol{r})$ in a proper functional space. The Hilbert-Sobolev space $\mathscr{H}^l(\Omega_l)$ of square-integrable functions with square-integrable

derivatives is generally chosen. After using the divergence theorem in the diffusion term and the BCs, the one-time differentiable solution is:

$$\begin{aligned}\frac{\partial}{\partial t}\int_{\Omega_l} v(\boldsymbol{r})M_l(\boldsymbol{r},t)\,d\boldsymbol{r} = &-\int_{\Omega_l}\nabla v(\boldsymbol{r})\cdot(D_l(\boldsymbol{r})\nabla M_l(\boldsymbol{r},t))\,d\boldsymbol{r} - \frac{1}{T_{2l}}\int_{\Omega_l} v(\boldsymbol{r})M_l(\boldsymbol{r},t)\,d\boldsymbol{r}\\ &- i\gamma f(t)\int_{\Omega_l} v(\boldsymbol{r})\boldsymbol{g}\cdot\boldsymbol{r}M_l(\boldsymbol{r},t)\,d\boldsymbol{r} - \int_{\Omega_l} v(\boldsymbol{r})\boldsymbol{v}(\boldsymbol{r},t)\cdot\nabla M_l(\boldsymbol{r},t)\,d\boldsymbol{r}\\ &- k_l^e\int_{\Gamma_l^e} v(\boldsymbol{r})M_l(\boldsymbol{r},t)\,d\boldsymbol{r} + \sum_n k_{ln}\int_{\Gamma_{ln}} v(\boldsymbol{r})(M_n(\boldsymbol{r},t) - M_l(\boldsymbol{r},t))\,d\boldsymbol{r},\end{aligned} \tag{2.31}$$

In order to obtain a discretisation of Eq. (2.31), it is necessary to find a solution belonging to $\mathscr{V}_h$, a finite-dimensional subspace of $\mathscr{H}^l$. Let $\{\phi_1^l(\boldsymbol{r}),\phi_2^l(\boldsymbol{r}),...,\phi_N^l(\boldsymbol{r})\}$ be a basis of $\mathscr{V}_h$ such that for all $g(t)\in\mathscr{V}_h, g(t)=\sum_{i=1}^N\phi_i^l(\boldsymbol{r})\eta_i^l(t)$, with $\eta_i^l(t)\in\mathbb{C}$ Then, the approximation of the transverse magnetisation $m_l^*(\boldsymbol{r},t)\in\mathscr{V}_h$ satisfying Eq. (2.31) is defined as

$$m_l^*(\boldsymbol{r},t) = \sum_{i=1}^N \phi_i^l(\boldsymbol{r})\eta_i^l(t) \tag{2.32}$$

In the case of choosing the test functions as the basis functions, i.e. $v(\boldsymbol{r})=\phi_i^l(\boldsymbol{r})(j=1,...,N)$, it is possible to obtain (after some algebra)

$$\boldsymbol{M}_l\frac{\delta\eta_l}{\delta t} = -(\boldsymbol{S}_l + i\,\boldsymbol{Q}_l(t) + \frac{1}{T_l}\boldsymbol{M}_l + \boldsymbol{J}_l + \boldsymbol{F}_l(t))\eta_l \tag{2.33}$$

where

$$\{\boldsymbol{M}_l\}_{ij} \triangleq M_{ij} = \int_{\Omega_l}\phi_j^l(\boldsymbol{r})\phi_i^l(\boldsymbol{r})\,d\boldsymbol{r} \tag{2.34}$$

is the mass matrix,

$$\{\boldsymbol{S}_l\}_{ij} \triangleq S_{ij} = \int_{\Omega_l}\nabla\phi_j^l(\boldsymbol{r})\boldsymbol{D}_l\nabla\phi_i^l(\boldsymbol{r})\,d\boldsymbol{r} \tag{2.35}$$

is the stiffness matrix,

$$\{\boldsymbol{Q}_l\}_{ij}(t) \triangleq Q_{ij}(t) = \gamma\int_{\Omega_l}\phi_j^l(\boldsymbol{r})\phi_i^l(\boldsymbol{r})f(t)\boldsymbol{g}\cdot\boldsymbol{r}\,d\boldsymbol{r} \tag{2.36}$$

is the scaled-mass matrix,

$$\{\boldsymbol{J}_l\}_{ij} \triangleq J_{ij} = \kappa_l^e\int_{\Gamma_l^e}\phi_j^l(\boldsymbol{r})\phi_i^l(\boldsymbol{r})\,d\boldsymbol{r} \tag{2.37}$$

is the flux matrix, and

$$\{\boldsymbol{F}_l\}_{ij} \triangleq F_{ij} = \int_{\Omega_l}\phi_j^l(\boldsymbol{r})\boldsymbol{v}(\boldsymbol{r},t)\cdot\nabla\phi_i^l(\boldsymbol{r})\,d\boldsymbol{r} \tag{2.38}$$

is the damping matrix. η_l is approximation of magnetisation, and $(\phi_i(\boldsymbol{r}))_{i\in N}$ (where N denotes number of nodes) is the basis functions of $H^1_M(\Omega)$. To the best of my knowledge, there is a toolbox for simulating the dMRI signal based on solving the Bloch-Torrey equation using FEM, which is developed by Li et al. [2019].

2.8 Computational Modelling of Intravoxel Incoherent Motion Imaging

2.8.1 Vascular trajectory-based simulation

To date, all the numerical studies of IVIM have been done using a simple numerical method. This elementary numerical method simulates the movement of spins based on blood flow velocity over vascular trajectories $R(t')$. Then, the acquired phase ϕ_t due to these displacements of spins is computed as $\phi_t = \int_0^t \gamma G t(R(t'), t')dt'$, and finally, the approximate IVIM signal is computed using $S = S_0\mathbb{E}\{e^{(i\phi_t)}\}$, where $\mathbb{E}\{\}$ is expectation of random variable of ϕ_t Mozumder et al. [2018], Spinner et al. [2019], Van et al. [2021].

Chapter 3 : Relevant Myocardial Tissue Components and Their Properties Contributive to dMRI

3.1 Chapter summary

Myocardium is a composition of many different components. Hence, before devising the structure of the myocardial *in-silico* phantom, the necessary step is to discover which resident components in the myocardium should be modelled in the phantom. The purpose of this chapter is to review different myocardial components and their geometrical features along with introducing the most contributive components to cardiac dMRI that should be included in the proposed numerical phantom.

3.2 Selection criteria for myocardial cells or components

In dMRI, the measurement of water diffusion within tissues is sensitive to the microscopic structure of the tissue, specifically the barriers to water diffusion caused by the presence of cell membranes and other intracellular (IC) structures. When there is a high volume fraction (VF) of cells or compartments in tissue, they create more barriers to water diffusion. As a result, these cells or compartments impose more influence on the measured dMRI signal. According to Seidel et al. [2016], CMs, extracellular space (ECS), microvascular, and non-CMs cells comprise 66%, 24%, 8%, and 2% of myocardial volume, respectively. In the following sections, we review these components and describe their geometry.

3.3 Cardiomyocytes

CMs are the cells contributing the most toward the measured dMRI signal in the myocardium. They occupy 65-75% [Chen et al., 2007, Greiner et al., 2018, Schaper et al., 1985, Skepper and Navaratnam, 1995] of the myocardial volume and account for 25-35% of all cells [Pinto et al., 2016, Zhou and Pu, 2016]. CMs support the mechanical

contraction of the heart, which is necessary to pump blood to all organs within the body [Fraticelli et al., 1989].

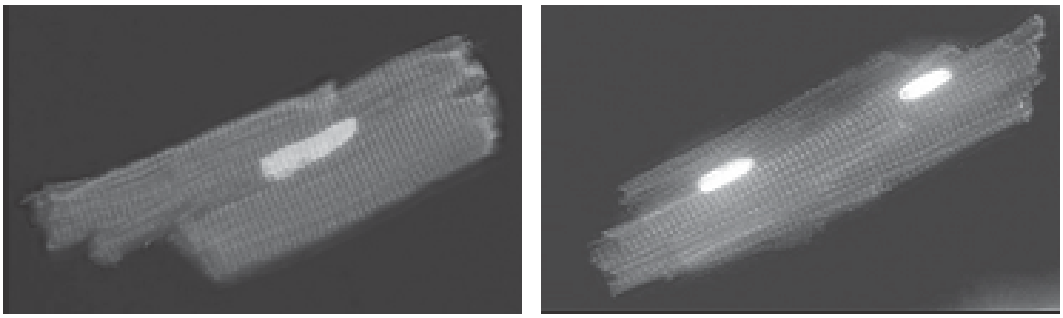

Figure 3.1: Two examples of the shape of an isolated CM with one and two nuclei (Brighter objects) in the left and right, respectively. Images with permission from [Gerdes and Pingitore, 2014].

3.3.1 Intracellular structures of cardiomyocyte

IC structures are essential for their function in generating and propagating electrical signals and contracting to pump blood. Some of the key intracellular structures in CMs include:

- **Sarcomeres:** These are the fundamental contractile units of muscle cells, including CMs. Sarcomeres are composed of thick and thin filaments made of proteins called myosin and actin, respectively. The interaction between these filaments leads to muscle contraction. They can be around 2 µm to 3 µm in length.
- **Mitochondria:** CMs have a high demand for energy due to their continuous contraction. Mitochondria are organelles responsible for producing adenosine triphosphate, the cell's primary energy source, through cellular respiration. they can range from 1 µm to 10 µm in length and 0.5 µm to 1 µm in diameter.
- **Nucleus:** Like other cells, CMs have a nucleus that contains the genetic material and controls cell activities, including protein synthesis necessary for maintaining cell structure and function. The nucleus can be around 5 µm to 10 µm in diameter.
- **T-tubules:** These are invaginations of the cell membrane (sarcolemma) that penetrate deep into the CM. T-tubules play a vital role in transmitting electrical

signals (action potentials) from the cell surface to the interior of the cell, ensuring synchronous contraction of the entire cell. Their diameter is approximately 200 nm to 300 nm.

- **Golgi apparatus:** This organelle is responsible for processing and packaging proteins for secretion or use within the cell. It plays a role in maintaining the structure and function of the cell membrane and organelles. The size of the Golgi apparatus can vary, with individual stacks having diameters of approximately 0.5 µm to 1 µm.
- **Cytoskeleton:** The cytoskeleton provides structural support to the cell and helps maintain its shape. It consists of protein filaments such as microtubules, microfilaments, and intermediate filaments. The thickness of microfilaments (actin filaments) and microtubules can be around 5 nm to 9 nm and 25 nm, respectively.

Given the typical diffusion time scale of dMRI and the consequent diffusion of water molecules, and the dimension of IC structure Rog-Zielinska et al. [2016], the effect of IC structure on IC diffusion is coarse-grained. More information about the coarse-grained effect can be found in [Novikov et al., 2016]. Therefore, the homogenising effect of the collagen fibre is seen as an effective medium with specific diffusivity.

3.3.2 Cardiomyocyte shape

The CM's membrane restricts the movement of water molecules and affects the dMRI signal. As illustrated in Figure 3.1, native CMs do not have a regular and consistent shape. However, in previous works, they are typically approximated as elliptical cylinders [Bolli et al., 2014]. Here, a realistic shape of the CMs in the proposed phantom is considered, as they constrain the mobility of water molecules.

A standard method to measure the dimensions of CMs is through the combined use of a Coulter channelyser and an optical microscope. The average length for the minor-axis (B), major-axis (A), longitudinal axis (L) of CMs along with their volume (V) have been reported as $12 \pm 1\,\mu m$. $30 \pm 1\,\mu m$, $141 \pm 9\,\mu m$, and $39933 \pm 4640\,\mu m^3$ respectively [Chen et al., 2007].

3.3.3 Cardiomyocyte membrane permeability

The permeability of CMs, defined as the CM-ECS water molecules exchange rate through sarcolemma, or CM-CM water molecules exchange rate through ICDs, is another biophysical feature of CMs that affects the dMRI signal.

Sarcolemma

The sarcolemma is a plasma membrane that acts as a boundary between the intracellular space (ICS) cytoplasm and ECS. It was shown that, during ischemic injury, the sarcolemma is ruptured, and CM permeability increases [Celes et al., 2010]. This feature is reflected in the phantom by assigning an interface permeability for the side surface of the CMs.

Intercalated discs

In adult hearts, ICDs are membranous regions where myofibrils of individual CMs are connected end-to-end with each other. Gap junctions are ICS channels through the ICDs that allow the passage of small molecules and ions between CMs through ICS diffusion. This arrangement facilitates the transmission of electrical impulses in the heart. Several studies have shown that gap junctions reduce in heart failure and can lead to fatal arrhythmia, leading to a decrease in the permeability of ICDs [Noorman et al., 2009, Perriard et al., 2003, Pinali et al., 2015]. ICDs' permeability are modelled by attributing an interface permeability to the top and bottom sides of the CMs.

3.3.4 Cardiomyocyte arrangement

The spatial organization of CMs within the myocardium determines biophysical characteristics that affect the dMRI signal. These include the following:

Sheetlet angles

Individual CMs are tightly packed into parallel laminar microstructures (as shown in Figure 3.2a), approximately 2-4 CMs thick, referred to as sheetlets [Hales et al., 2012]. These sheetlets orient locally in the tissue and are separated by cleavage with a width of 1-2 CMs from each other [LeGrice et al., 2005]. It has been shown and validated by histology that the primary (V_1), secondary (V_2), and tertiary (V_3) eigenvectors of

cardiac DTI (cDTI) correspond to the CM's long-axis, sheetlet, and sheetlet-normal directions, respectively, as shown in Figure 3.2a and 3.2b.

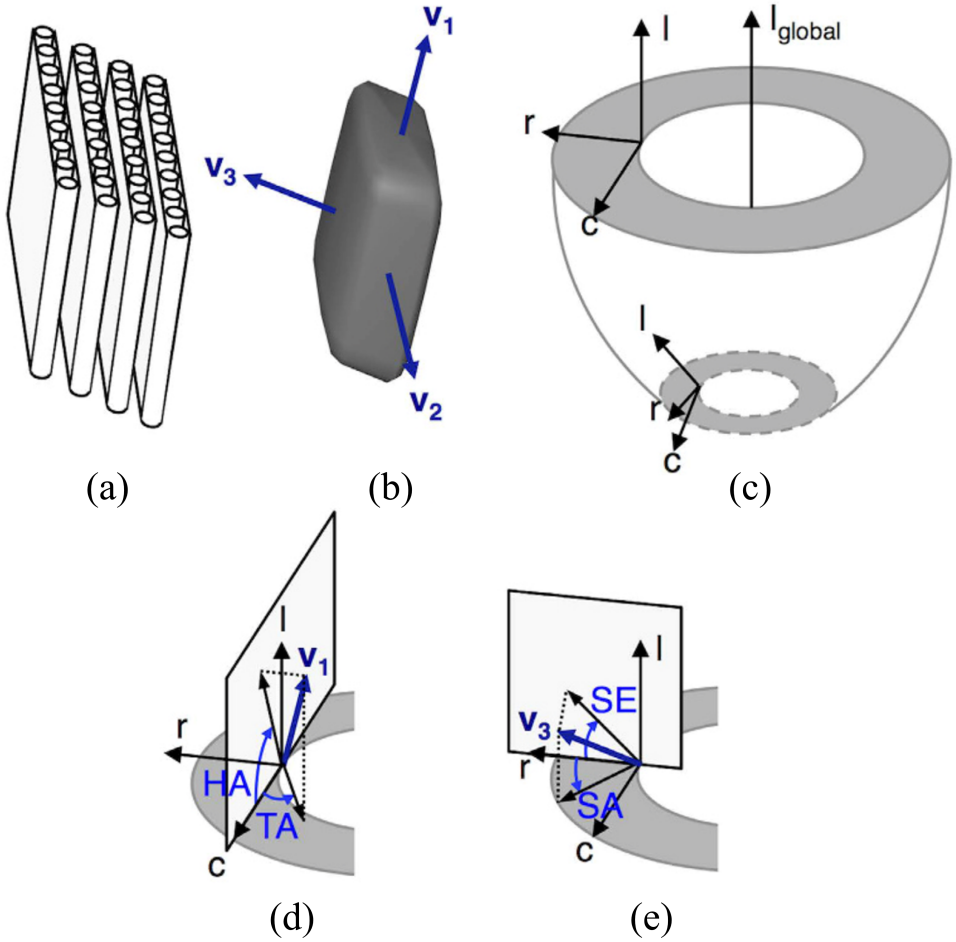

Figure 3.2: Definition of helix, transverse, sheet elevation, and sheet azimuth angles. a) Tightly packing CMs into a laminar structure; b) Superquadric glyph representation of the diffusion tensor and eigenvectors of (a); c) illustration of local cardiac coordinate; d) Helix and transverse angles, e) Sheet elevation and sheet azimuth angles. Image with permission from [Teh et al., 2016].

Using V_1 and V_3 [Teh et al., 2016], four angles are usually considered to describe these directions of the sheetlets. As shown in Figure 3.2c, a local coordinate system can be defined for each voxel in a cardiac image volume, based on the surface curvature of the cardiac wall, distinguished by longitudinal (**l**), radial (**r**) and circumferential (**c**) axes. **r** is computed using the Laplace method [Jones et al., 2000], whereas **c** is

defined as vectors perpendicular to **r** and global longitudinal ($\mathbf{l}_{global}$, a line fitted to the center of left ventricle cavity in 2D short-axis planes). Finally, **l** is defined as vectors perpendicular to $\mathbf{r} \times \mathbf{c}$. Therefore, as shown in Figure 3.2d, *helix angle* (HA) and *transverse angle* (TA) are defined as the angles subtended by **c** and projection of V_1 on **l-c** and **r-c** planes, respectively. The angles subtended by **r** and projection of V_3 on **l-r** and **r-c** planes are called *sheet elevation* (SE) and *sheet azimuth* (SA) angles.

Inter-CM and inter-sheetlet spaces

Inter-CM and inter-sheetlet spaces refer to the gaps or extracellular spaces between individual cardiomyocytes and sheetlets, respectively. These spaces might contain various components of the extracellular matrix like collagen and non-CM cells, which provide structural support to the heart tissue, as well as facilitate communication and signalling between cells. These spaces reduce or increase due to ageing or pathologies like hypertrophy Anversa et al. [2005], Engelmann et al. [1987], LeGrice et al. [2012], Yabluchanskiy et al. [2014].

Myocardial transmural twist

Figure 3.3 represents a simplified schematic of CM's long-axis direction, where it starts with a right-handed helical orientation in the endocardium and smoothly changes toward a left-handed helical orientation in the epicardium [Hales et al., 2012]. The measured V_1 corresponds to an average of the CMs' long axes directions within an MRI voxel [Streeter Jr et al., 1969]. Therefore, the magnitude of the primary eigenvalue of cDTI should be modulated by the standard deviation of this helical orientation distribution.

Ventricle curvature

Ventricle curvature is another important geometrical feature that affects sheetlets' shape, and consequently, CMs' shape (of myocardial tissue that undergoes remodelling in some CVDs). For instance, a normal left ventricle has an ellipsoidal geometry that alters to a more spherical one following myocardial infarction [Su et al., 2012]. The curvature values for different regions of the healthy and infarcted myocardium of rats are reported in [Espe et al., 2017, Weisman et al., 1985].

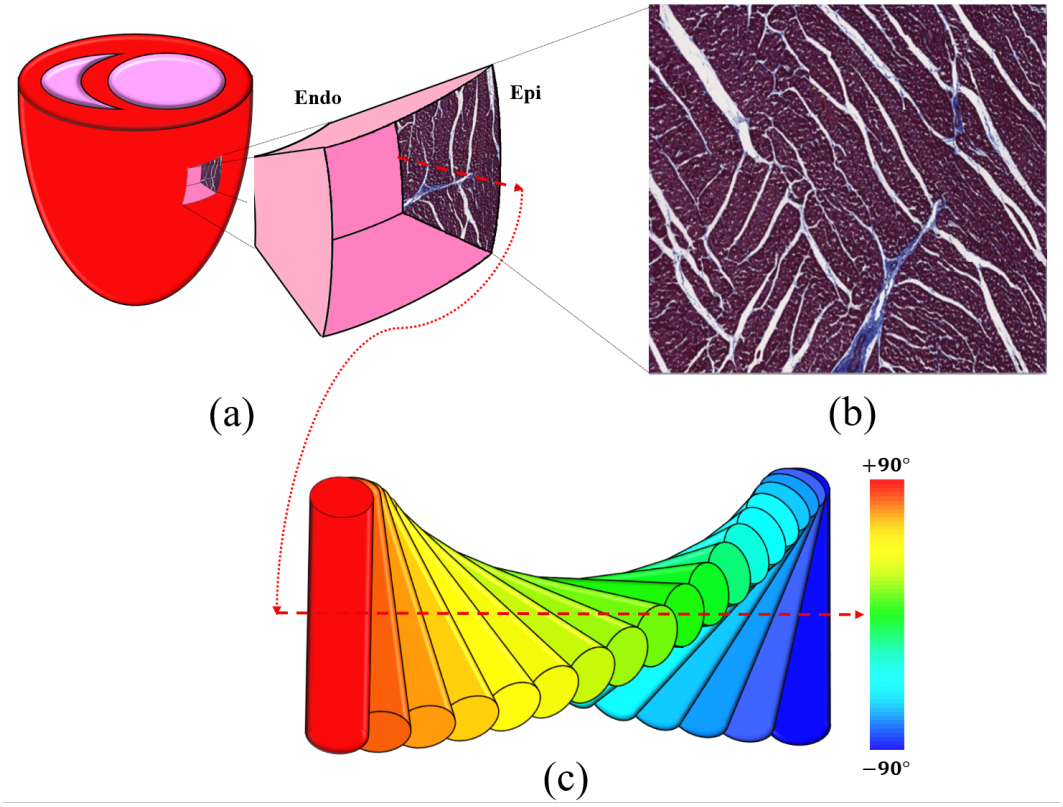

Figure 3.3: The arrangement of CMs in sheetlets in cardiac tissue. (a) a cubic slab of myocardium in local cardiac coordinate; (b) histological image from **l-r** plane view of myocardium, with permission from [Nielles-Vallespin et al., 2017]; (c) Simplified schematic of direction changes in CM's long axes transmurally from endocardium to epicardium where the heat-map shows HA variation.

3.4 Extracellular matrix

There is no doubt that the extracellular matrix (ECM) within the ECS of the cardiac muscle is highly responsive to mechanical loading and it is one of the key elements in the remodelling that occurs due to change of loading conditions LeGrice et al. [2005]. ECM of the heart, mainly made up of collagen fibres, provides a stress-tolerant network for the distribution of forces in the heart and alignment of the CMs Carver et al. [1991].

3.4.1 Collagen

Collagen fibre is the dominant component of ECM. Essentially it provides structural support to the myocardium by transmitting forces, preventing the myocardium from being overstretched and rupturing, and it maintains the shape and thickness of the myocardium while providing both active and passive stabilization to the myocardium [Benedicto et al., 2011]. As illustrated in Figure 3.4, the collagen fibres fall into three categories: endomysium, surrounding and interconnecting individual CMs and capillaries; perimysium, surrounding and interconnecting groups of CMs; and epimysium, surrounding the entire muscle [Pope et al., 2008]. Of the collagen fibres, only endomysium (Figure 3.5a) and perimysium (Figure 3.5b) are modelled in the proposed phantom as it is unlikely for many dMRI voxels to include effects of the epimysium in the dMRI signal, as epimysium locates at the surface of the muscle as shown in Figure 3.4.

Furthermore, since the thickness of the collagen fibre is at a nanoscale [Benedicto et al., 2011], given the typical diffusion time scale of dMRI and the consequent diffusion of water molecules, the effect of collagen fibre on ECS diffusion is coarse-grained. More information about the coarse-grained effect can be found in [Novikov et al., 2016]. Therefore, the homogenising effect of the collagen fibre is seen as an effective medium with specific diffusivity.

3.5 Microvasculature

Microvasculature comprises 8% of VF of myocardium tissue according to Seidel et al. [2016] which is actually an essential component of all tissues. During blood perfusion, this dynamic infrastructure distributes oxygen, nutrients, and drugs uniformly to the cells, while ensuring toxic metabolic waste is discharged. A microvascular network con-

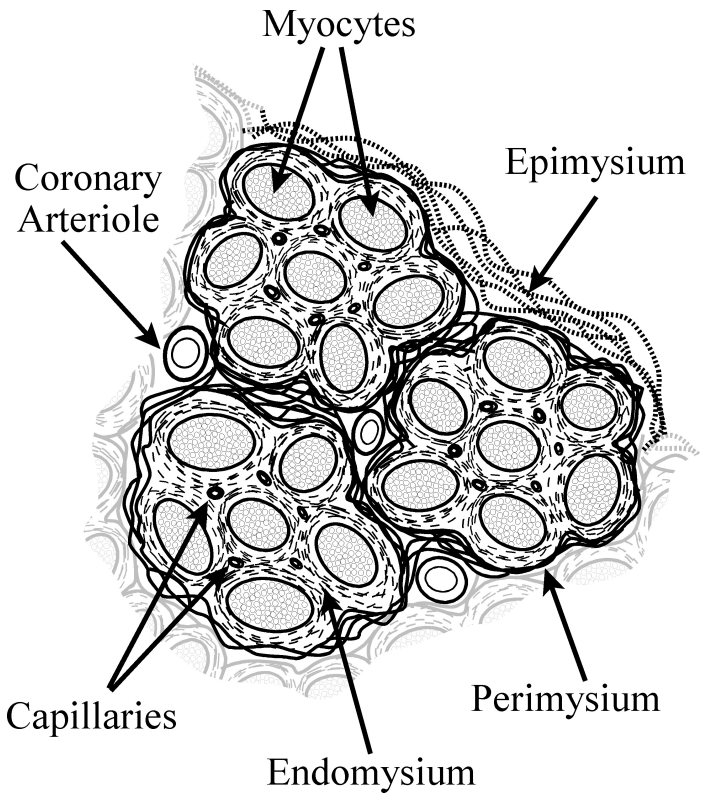

Figure 3.4: Structural organization of cardiac ECM. Here is a schematic illustration of fibrillar collagen arranged in relation to CMs as well as coronary vasculature in relation to fibrillar collagen. An endomysium is a structure consisting of collagen fibres that surround particular CMs and collagen struts that bind adjacent CMs together. Within the perimysium, there is a grouping of CMs that are called CMs bundles. There are groups of perimysial bundles enclosed in the epimysium. Image with permission Brown [2005]

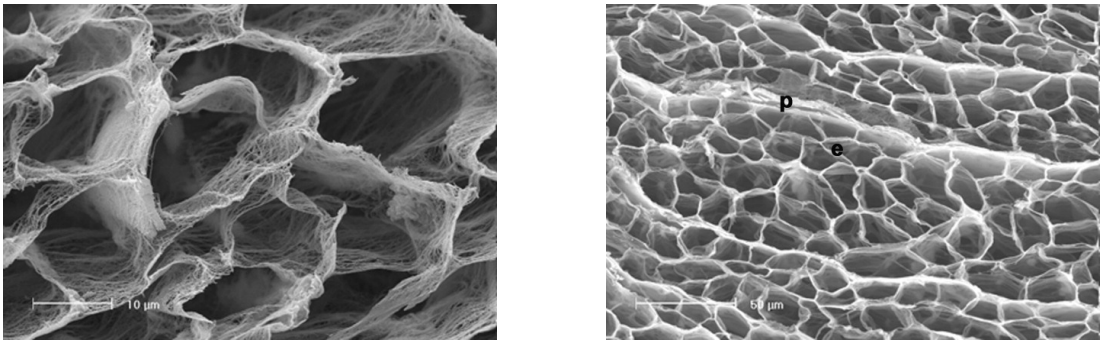

(a) (b)

Figure 3.5: SEM of the three-dimensional arrangement of the cardiac collagen fibres in healthy dogs. a) Endomysia b) Endomysia (e) and Perimysium (p). Image with permission [Benedicto et al., 2011].

sists of thousands of microvessels that are heterogeneous in size, length, and phenotype. This network—which is topologically unique for different tissues—provides short and homogeneous diffusion distances between individual capillaries, with low resistances and regulatable pathways for blood flow Beare et al. [2018].

3.5.1 Endothelial cells

Hearts contain many other components besides CMs, with endothelial cells (ECs) accounting for the largest proportion of these components with a share of ∼60% Pinto et al. [2016]. According to Seidel et al. [2016], the lumen only comprises 3.7% out of 8% VF of microvasculature and the ECs comprise the remaining volume of the microvasculature. The role of ECs in cardiac maturation and vascular homeostasis is critical, as well as their role in healing and regeneration following post-ischemic injuries Gray et al. [2018].

3.6 Non-cardiomyocytes cells

3.6.1 Mesenchymal Stem cells

The resident mesenchymal stem cells (MSCs) account for ∼27% of non-CMs cell count, divided into Fibroblasts (FBs), ∼15%, and non-Fibroblast MSCs (non-FB-MSCs),

∼12% Pinto et al. [2016]. FBs play a prominent role in supporting and maintaining normal cardiac function, namely preserving the stability of ECM by synthesis and degradation of collagen or replacing dying cardiomyocytes with ECM in the injuries Doppler et al. [2017]. Non-FB-MSCs are a class of heterogeneous stem cells that differentiate into different cell types, like CMs – only less than 30% of non-Fb-MSCs contribute to the regeneration of CMs Wei et al. [2011]. FBs and non-FB-MSCs have the same simplified morphology, long flat spindle-shaped, that can not be distinguished visually Soundararajan and Kannan [2018].

3.6.2 Myeloid cells

The last frequent non-CMs cells are Myeloid cells (MCs) which comprise 7% of myocardium resident cells Pinto et al. [2016]. MCs' key function is to preserve the healthy condition of the heart against viruses and bacterial infection Nahrendorf [2019]. MCs are a range of immune cells including neutrophils, monocytes, and macrophages – Neutrophils and monocytes are scarce in normal myocardium, collectively $< 1\%$, and similar to MSCs' shape, adopt a spindle-like shape.

3.7 Conclusion

Earlier in 3.2, it is explained that the primary criterion for including a myocardial component in a numerical phantom with the application in dMRI simulation is the VF occupied by that component. According to the first criterion, among the above-mentioned components, only CMs, ECS, and microvascular occupy considerable VF of myocardial tissue.

However, it is not possible to replicate the *in-silico* version of non-CMs since their dimensions and biophysical characteristics are not very well known. Furthermore, due to the lack of information about the myocardial microvasculature network, including the connection and distribution of capillaries between the CMs, it is not possible to include a *in-silico* replicant of the microvasculature network as a unique component into the numerical phantom. As a result, in this thesis, I attempt to generate the numerical phantom by replicating the *in-silico* CMs and ECS, as well as their relevant properties.

Chapter 4 : Three-dimensional micro-structurally informed in silico myocardium for virtual cardiac diffusion-weighted MRI

4.1 Chapter summary

This chapter introduces the proposed method to generate a more realistic myocardial numerical phantom which accounts for the variability of the CMs shape, water exchange between the CMs (ICDs), disorder class of myocardial microstructure, and four sheetlet orientations. In order to evaluate the performance of the generated phantom, some experiments are presented, including morphometric analysis, histology comparison, and simulated DTI compared to *ex-vivo* DTI.

This chapter was published in Lashgari et al. [2022]

4.2 Introduction

A numerical phantom offers a number of advantages over a physical counterpart, including reduced time and costs, reproducibility of results Sauer et al. [2022], the ability to control model detail and complexity of tissue microstructure, and a reduction in the pronounced artefacts caused by dismissing the properties of unknown materials in a physical phantom Fieremans and Lee [2018]. Numerical phantoms combined with MC or FE method-based simulators provide virtual frameworks to assist in the biophysical modelling and interpretation of cardiac dMRI signals. In addition, this virtual framework can assist in designing and conducting a feasibility study of the inverse problem to be solved, as well as analyzing how dMRI measurements are affected by changes in tissue microstructure and pulse sequences Bates et al. [2017], Rose et al. [2019].

In addition, integrating an accurate cardiac numerical phantom with a validated imaging simulator facilitates virtual imaging trials in cardiac dMRI. The virtual imaging trial is a unique alternative to assess and optimise medical imaging technologies by imitating the conventional imaging trials and studying the states that are not physically realisable nor ethically responsible in vivo Abadi et al. [2020, 2021], Sauer et al. [2022].

In addition, virtual imaging trials promise to lead to faster, safer and cost-effective regulatory studies compared to conventional clinical trials, due to replacing actual patients and imaging devices with virtual surrogates Abadi et al. [2020].

This chapter proposes a novel method to generate a realistic numerical phantom of myocardial microstructure. The proposed method extends previous studies by accounting for the variability of the cardiomyocyte shape, water exchange between the cardiomyocytes (intercalated discs), disorder class of myocardial microstructure, and four sheetlet orientations. In the first stage of the method, cardiomyocytes and sheetlets are generated by considering the shape variability and intercalated discs in cardiomyocyte-cardiomyocyte connections. Sheetlets are then aggregated and oriented in the directions of interest.

4.3 Literature review

Until now few studies have explored the benefits and challenges associated with designing numerical phantoms of the myocardium for cardiac dMRI. The first cardiac numerical phantom was proposed by [Wang et al., 2011]. They generated a multi-scale numerical phantom across numerous spatial resolutions and used these phantoms to produce dMRI signal via MC simulations. Their numerical phantom included a packed arrangement of CMs, simplified as cylindrical geometries with hexagonal cross sections. In a subsequent study, the same authors presented a different phantom design, modelling CMs as cylinders with different sizes, arrangements, and length/diameter ratios with varying numbers of CMs ($1, 8, 64$, and 8000). Next, they modelled sheetlet structures by arranging CMs based on their orientation [Wang et al., 2012]. [Bates et al., 2017] previously introduced a numerical phantom in which the length, cross-sectional area, and aspect ratio (thickness/width) of CMs were based on data from the literature. In proposed approach, the CMs were modelled as rectangular cuboids and arranged in two stages. The CMs were first arranged parallelly to form a sheetlet (sub-voxel stage). Next, adjacent sheetlets within a voxel were progressively rotated to simulate the transmural variation in the helix angle (HA) (sheetlet or voxel stage) [Bates et al., 2017]. In a recent study, [Rose et al., 2019] generated a numerical phantom based on histological images of the heart. CMs were first manually segmented from a sub-voxel area of the image, and the segmentation boundaries were then approximated with polygons with an average of 99 vertices. Next, by extruding individual CMs along the normal

perpendicular to their boundary in the 2D plane, a 3D block of CMs was created with random uniformly distributed lengths. Finally, they modelled HA by placing several blocks next to each other using different angles for the longitudinal axis of the cardiac local coordinate system [Rose et al., 2019]. Table 4.1 compares previous numerical phantoms in terms of the biophysical characteristics of the myocardial compartments, introduced in Chapter 3, they incorporated.

4.4 Innovation

The goal of this chapter is to address the limitations of the previous numerical phantoms of the heart muscle tissue, namely the lack of a detailed numerical phantom and the failure to incorporate cellular shape variability. Concerning the first limitation, the numerical phantom mimics the most relevant biophysical characteristics of ECS and ICS within the myocardium. There is evidence to suggest that regional curvature of ventricles [Espe et al., 2017, Su et al., 2012, Weisman et al., 1985], collagen in ECS matrix [Haddad and Samani, 2017], ICDs in ICS [Noorman et al., 2009, Perriard et al., 2003, Pinali et al., 2015], and changes in their respective biophysical characteristics are closely linked to some CVDs. Although these changes may affect dMRI signals, no study to date has modelled these characteristics and focused solely on modelling the CMs and ECS. Concerning the second limitation, most studies typically consider identical sets of simple geometries for cellular shape, limiting the complexity of the myocardium captured by numerical phantoms. These phantoms perform poorly compared with phantoms generated from histological images of tissues [Naughton and Georgiadis, 2019]. Moreover, it has been demonstrated that the disorder class of microstructure (determined based on the cellular shape variability and packing disorderliness) affects the coefficients of the time dependence diffusion at the macroscale [Novikov et al., 2014]. Consequently, it is imperative to consider the native probability distribution functions (PDFs) of the biophysical parameters associated with CMs shape (introduced in Chapter 3) when devising a realistic numerical phantom. Finally, the use of FE analysis to simulate the dMRI signal of the myocardium is investigated, as it is more faster than the conventional MC approach [Grebenkov, 2016]. To the best of my knowledge, this has not been explored previously in the heart.

Table 4.1: Comparison between the proposed and previous numerical phantoms including biophysical properties of the myocardium

Features	Radial shape variability of CMs	Axial shape variability of CMs	Sarcolemma ICDs permeability	Sarcolemma ICDs permeability	HA°	SE°	SA°	TA°	Regional curvature	Collagen
[Wang et al., 2011]	✗	✗	✓	✗	✗	✗	✗	✗	✗	✗
[Wang et al., 2012]	✗	✗	✓	✗	✓	✗	✗	✗	✗	✗
[Bates et al., 2017]	✗	✗	✓	✗	✓	✗	✗	✗	✗	✗
[Rose et al., 2019]	✓	✗	✗	✗	✓	✓	✗	✗	✗	✗

4.5 Method

As discussed earlier, the arrangement of CMs in the myocardium can be considered at two scales, i.e., at the scale of a sheetlet and at the scale of the myocardial wall (comprising several sheetlets). At the sheetlet scale, CMs are densely packed with a near-parallel arrangement into a sheet-like structure [Hales et al., 2012]. Conversely, the sheetlets are placed next to each other at the wall scale while orientated based on desired sheetlet angles. Therefore, packing CMs with diverse shapes while preserving the input PDFs of the shape parameters is a challenging task. This section proposes a method to address this task in two stages, corresponding to the sheetlet and wall scales.

4.5.1 Sheetlet Scale

Generating a 2D Cross-Section of a Sheetlet

A fully parallel arrangement of the CMs in the sheetlets is assumed, based on empirical evidence [Hales et al., 2012]. Therefore, dense packing of the CMs in a sheetlet can be generated in 2D and subsequently in 3D:

i *2D Ellipse Packing:* Limitation of the CMs' simplified cross-sections to ellipses or circles render a dense ellipse packing algorithm well suited to a 2D problem. Here I uses the dense ellipse packing algorithm proposed in [Ilin and Bernacki, 2016] to generate a primary 2D cross-section of the CMs packed densely in a 2D plane (Figure 4.1). The packing domain of ellipses is rectangular with a width of

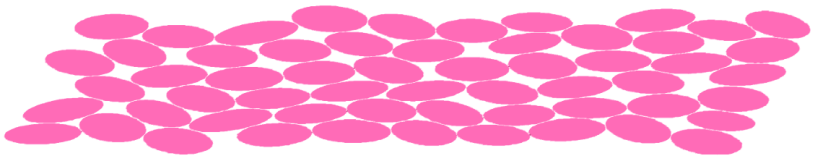

Figure 4.1: CMs' simplified cross-sections as packed ellipses.

sheetlet thickness (Table 4.1) and a length, larger than the final voxel's length. In this study, the length of the packing domain is set to 200 µm, two times larger than the final voxel's length (100 µm). The inputs to this algorithm are V, L, A, B, and dimensions of the packing domain (sheetlet thickness and length), shown in Table 4.1.

ii *Transformation of the 2D Pack of Ellipses to Polygons:* According to histological observations [Bensley et al., 2016], the native cross-section of CMs are polygons. Therefore, as proposed in [St-Pierre et al., 2008], the pack of ellipses is transformed into polygons using a watershed algorithm. Figure 4.2 depicts the cross-section of a myocardial sheetlet obtained from transforming packed ellipses to polygons.

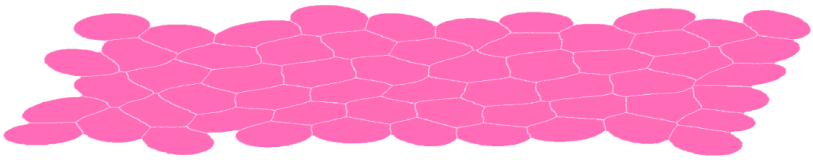

Figure 4.2: CMs'cross-sections as packed polygons.

Generating the 3D Shape of a Sheetlet Based on the 2D Cross-Section

The 3D shape of a sheetlet is formed by extruding the border of polygons/CMs along the normal axis to the cross-section of the sheetlet, according to the length PDF of CMs. Preserving the length PDF of CMs changes the volume PDF of CMs due to an increase in the area of the CMs' cross-section, following the transformation of ellipses to polygons. Hence, to preserve both input length and volume PDFs of CMs, a small segment is removed from the top of the extruded CMs as depicted in Figure 4.3 (left). This small segment is made up of the half cross-section of the CM, extruded long

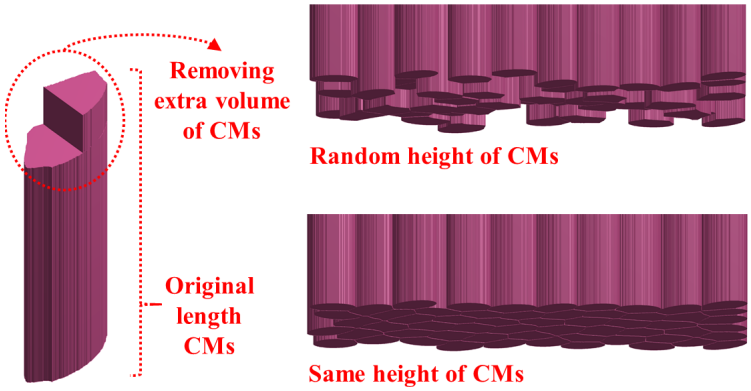

Figure 4.3: Generating the 3D Shape of a Sheetlet Based on the 2D Cross-Section.

enough to make its volume equal to the extra volume of the CM. Moreover, to better emulate real tissue and maintain some irregularity in the arrangement of CMs within

the phantom, CMs are placed at random heights (Figure 4.3, right). For each CM, the random height is a positive number, chosen from a uniform distribution in which the upper end of the CM does exceed the height of the highest CM in each group of CMs. The 3D shape of a short section of a sheetlet is illustrated in Figure 4.4.

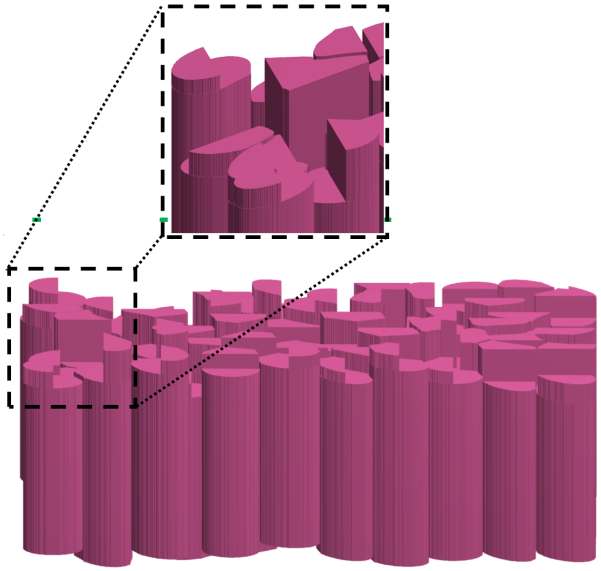

Figure 4.4: The 3D shape of a short section of a sheetlet.

Generating a Sheetlet

Given the average length of the CMs, 141 ± 9 μm, and the size of the *in-silico* voxel, several layers of the CMs must be stacked on top of one another to ensure a complete sheetlet is long enough. Figure 4.5 shows a short section of a sheetlet comprising two layers of CMs. The main challenges for extending a sheetlet, layer by layer, is that the ends of CMs at the lower layer (LL) are not aligned, as depicted in Figure 4.4 (magnified). To model ICDs and keep the ECS more realistic, each CM of the upper layer (UL) at its bottom should have a complementary shape concerning the top of the CMs in the LL, as shown in Figure 4.5 (magnified). This part of the algorithm includes the following steps:

i *Designing a Complementary Shape for CMs of UL:* First, to complete the sheetlet, along with preserving the randomness of the distribution of the CMs in the phantom, for each layer, a new cross-section of CMs are generated as described

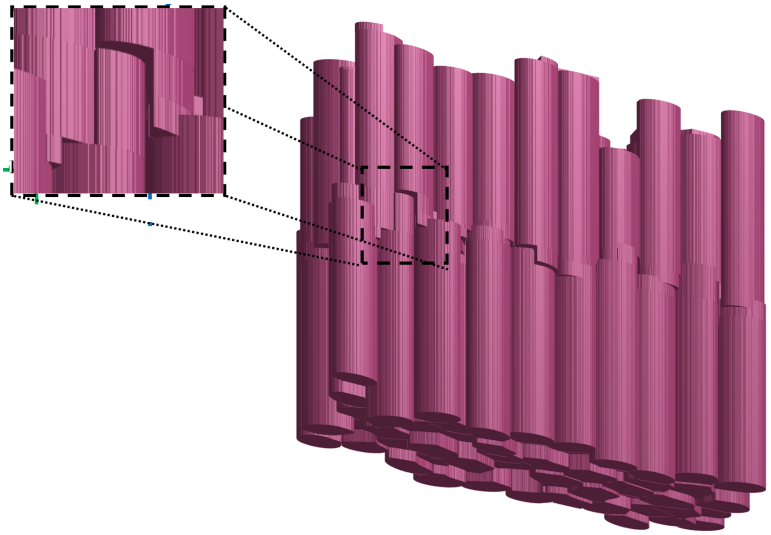

Figure 4.5: Short section of a sheetlet comprising two layers of CMs.

in Figure 4.6 and 4.7. Second, information about the intersections between the

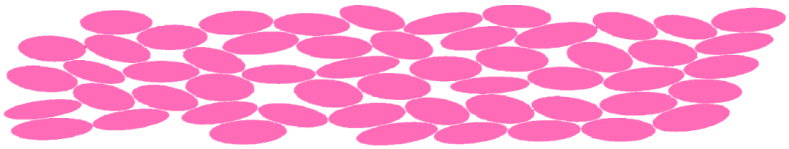

Figure 4.6: New CMs' simplified cross-sections as packed ellipses.

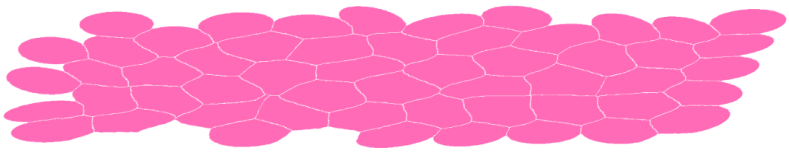

Figure 4.7: New CMs'cross-sections as packed polygons.

CMs in UL with CMs in LL and the height of their intersections, are acquired. Subsequently, using the acquired information, the complementary shape of CMs in UL is constructed. Next, the required steps are described in detail:

(a) *Finding the Intersection Between the CMs in the Successive Layers:* First, a topographic map of CMs in LL is generated as depicted in Figure 4.8. Next, since the cross-section of CMs in LL and UL are not the same (Figure

4.2 vs. 4.7), it is likely that some parts of marginal CMs in the UL, Figure 4.7, intersect the blue region (vacant region) in Figure 4.12h. Therefore, it

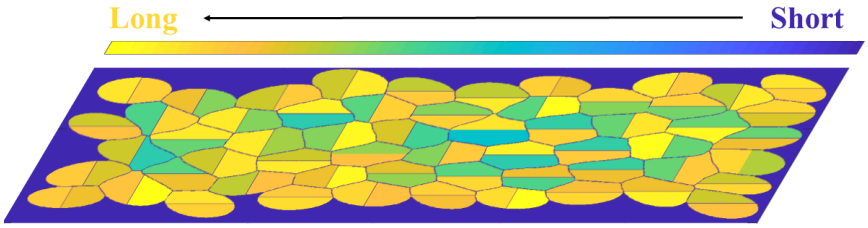

Figure 4.8: topographic map of CMs in LL.

is impossible to find the starting height for those parts of marginal CMs in UL, which intersect the blue region in Figure 4.8. Hence, the topographic map is modified so that the blue region is filled by the extension of marginal CMs in LL, as shown in Figure 4.9. Then, each CM in UL is intersected

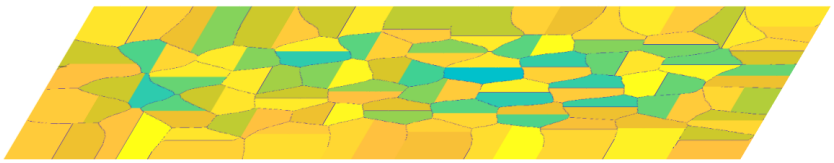

Figure 4.9: Modified topographic map where the blue region is filled by the extension of marginal CMs in LL.

with the modified topographic map. The result of the intersection of CMs in UL with the topographic map of CMs in LL is as shown in Figure 4.10, where blue polygons indicate the border of CMs of UL, shown in Figure 4.7.

(b) *Forming 3D Shape of CMs in UL:* For the intersection of each CM in UL with CMs in LL (e.g., Figure 4.10, a blue polygon with topographic map), the lowest segment (Figure 4.11a, the intersection of green region with blue polygon) is extruded to the height of second-lowest segment (Figure 4.11b). Then, at the height of the second-lowest segment, the first- and second-lowest segments (green and dark yellow inside the blue border, in Figure 4.10) are merged, as illustrated in Figure 4.11b, and extruded to the height of the third-lowest segment (Figure 4.11c). This procedure is repeated until

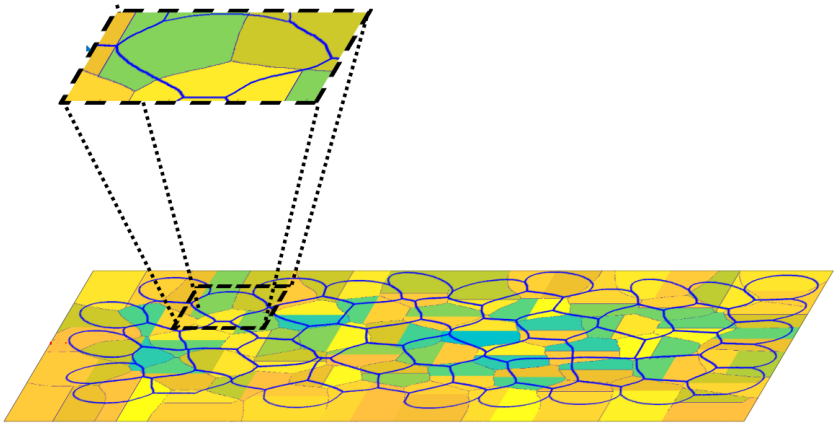

Figure 4.10: Intersection of CMs in UL with the topographic map of CMs in LL.

all segments of a CM are merged, and the original cross-section of the CM is retrieved (Figure 4.11c). Next, the original cross-section of CM is extruded long enough to preserve the input length of the CM. Finally, for CMs with increased volumes, a small segment is removed, illustrated in Figure 4.11d, as explained in 4.5.1.

Figure 4.5 shows adding the second layer of the CMs to the first layer (Figure 4.4). A complete sheetlet is formed by repeating this algorithm, blue box in Figure 4.12, for a desired number of layers.

4.5.2 Wall Scale

This Section describes the process of generating a voxel of the myocardium at a microscale, using the generated sheetlets in the previous Section. First, several sheetlets, depicted in pink in Figure 4.13a, are placed next to each other in the ECS, revealed by the blue color in Figure 4.13a. Endomysial and perimysium collagen fibres domains are indicated by grey colour in Figure 4.13a. The boundary of the collagen fibres domain is defined as an enlarged outline of the sheetlet. The ECS inside this domain, except the ICS regions, is labelled as the collagen region, and its effect is taken into account by assigning diffusivity ($D_{collagen}$) and relaxation ($T_{2_{collagen}}$) of collagen to it.

Next, the sheetlet angles are modelled by aligning the phantom in the directions of the desired eigenvectors. Because the eigenvectors are orthogonal, one only needs to align two of them in the desired directions. Since the SE, SA, HA, and TA angles are

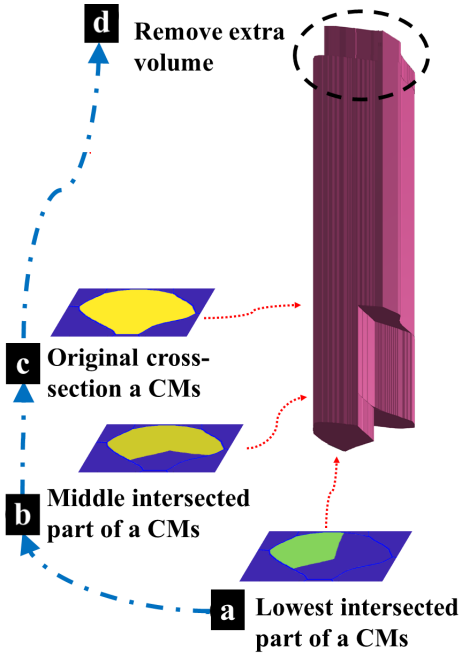

Figure 4.11: Intersection of CMs in UL with the topographic map of CMs in LL.

defined for V_1 and V_3, these eigenvectors are used for the alignment. Again, based on the orthogonality of eigenvectors, by setting three sheetlet angles out of four, V_1 and V_3 and consequently, V_2 are aligned in the desired directions. Here, the I orient the phantom based on SE, SA, and HA angles.

Initially, according to the relationship between sheetlet orientations and eigenvectors of cDTI, as shown in Figure 3.2b, V_1, V_2 and V_3 are set as depicted in Figure 4.13a. Then, to align V_3 in the desired direction, first, the phantom in its initial status, Figure 4.13a, is rotated around V_1 so that the projection of V_3 on **l-r** makes SE° angle with **r**, shown in Figure 4.12b. Second, the phantom is rotated around V_2, Figure 4.13b, so that SA° is subtended by **r** and the projection of V_3 on **r-c** as shown in Figure 4.13c. Then, to align V_1 in the desired direction, one only needs to rotate the phantom around V_3, Figure 4.13c. As a result, the subtended angle by the projection of V_1 on **l-c** and **c**, illustrated in Figure 4.13d, is equal to the desired HA°.

Next, the tissue is twisted by rotating the phantom of Figure 4.13d around the axis parallel to **r**, crossing through the center of the phantom, shown in Figure 4.13e, in which the degree of rotation (α) is increased by increasing the distance from the center of the phantom, as depicted in Figure 4.13e.

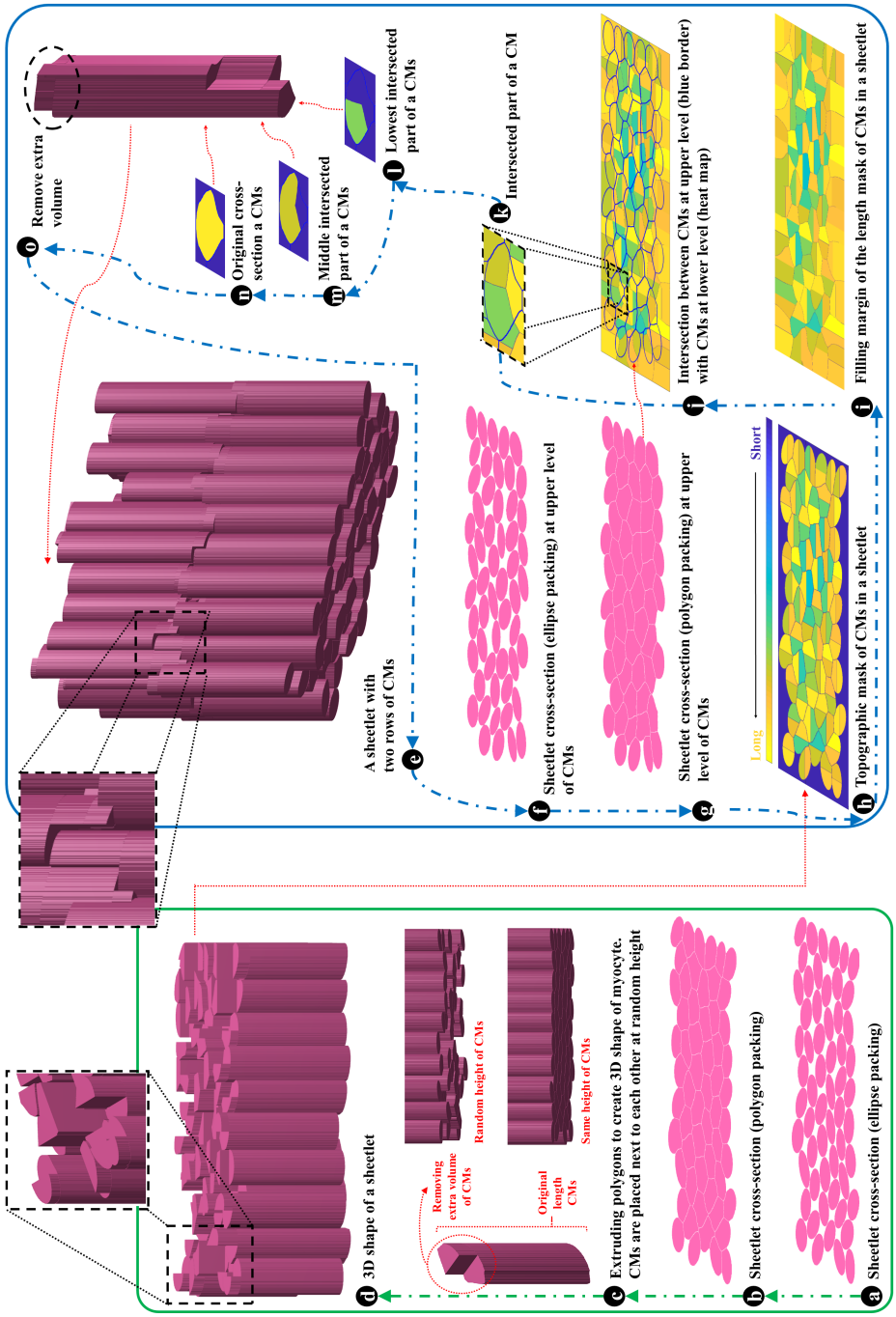

Figure 4.12: Schematic overview of the proposed approach for generating a numerical phantom of the myocardium, at the sheetlet scale.

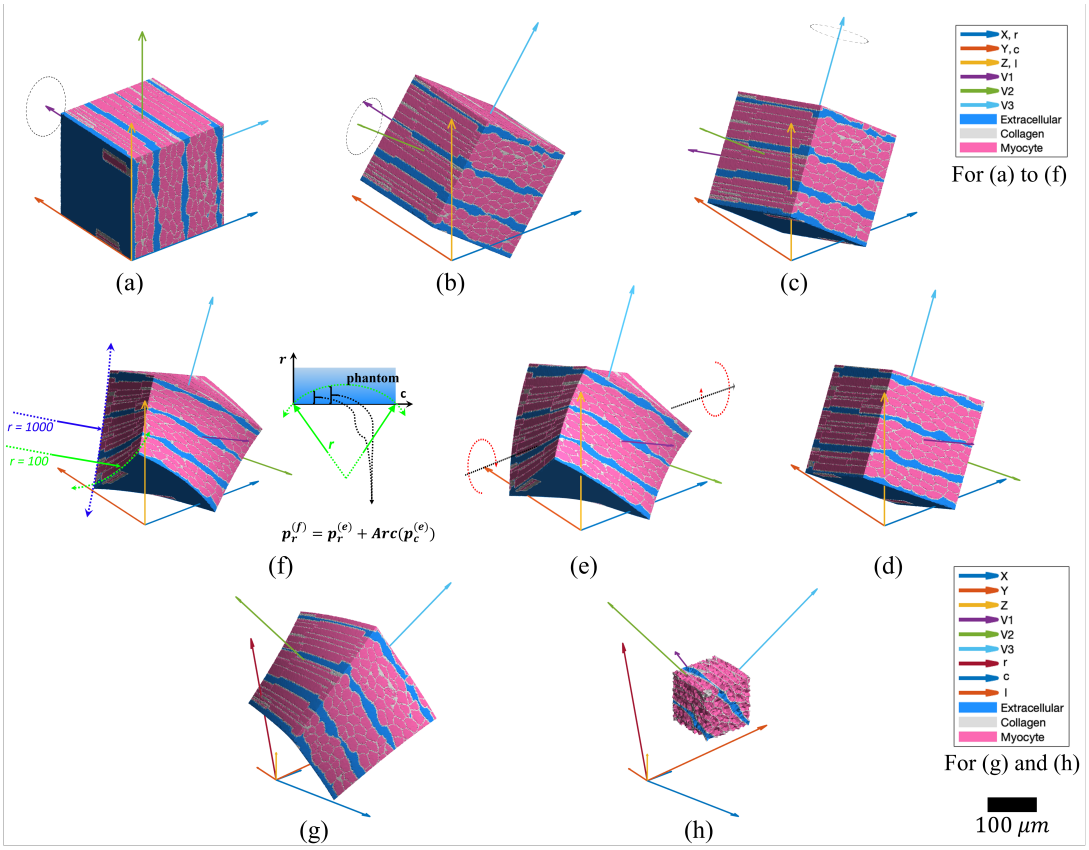

Figure 4.13: Algorithm for generating myocardium numerical phantom at wall scale: a) initial status of the sheetlets in-wall configuration, where V_1, V_2, V_3 are parallel to **c**, **l**, **r**, respectively; b) modelling SE° by rotating phantom in (a) around V_1; c) modelling SA° by rotating phantom in (b) around V_2; d) modelling HA° by rotating phantom in (c) around V_3; e) Twisting the phantom the axis crossing the centre of the phantom and parallel to **r**; f) modelling wall curvature by bending the phantom in (e) around the axes **l** and **c**; g) Transforming the phantom in (f) to cardiac local coordinate to mimic the sheetlet orientations in *ex-vivo* data; h) Extracting a cubic voxel to mimic an MRI voxel.

Then, the curvature of the myocardium wall is included in the phantom. For this purpose, the phantom should be bent around an axis parallel to **c** and crossing the point of $(\mathbf{c}, \frac{l}{2}, 0)$, and an axis parallel to **l** and crossing through $(\frac{l}{2}, \mathbf{l}, 0)$, where (l) is the length of the phantom across the axis **c**. For example, for the latter, all points in every **c-r** plane, depicted as blue in Figure 4.13f on the right-hand side, should be uniformly relocated to the green-dashed arrow. As depicted in Figure 4.13f (right-hand side), using the values of curvature $K = \frac{1}{r}$, where r (the green arrow) is the radius of the curvature, the displacement along axis **r**, $d_r = Arc(p_c)$, is computed where Arc computes the displacement of the location of phantom's nodes, i.e., (p_r, p_c, p_l), along the axis **r** using p_c or p_l. Then, the phantom is bent around an axis parallel to **l** and crossing through $(\frac{l}{2}, \mathbf{l}, 0)$ by updating the location of the phantom's nodes along with **r** concerning **c**, i.e., $p_r^{(f)} = p_r^{(e)} + Arc(p_c^{(e)})$ where superscripts (e) and (f) indicate nodes' location in the related phantoms in Figure 4.13e and 4.13f (left-hand side), respectively. Figure 4.13f (left-hand side) illustrates the bent phantom around an axis parallel to **l** and crossing from the point of $(\frac{l}{2}, \mathbf{l}, 0)$ indicated by a light green arc with $r = 100$. Similarly, by updating $p_r^{(f)} = p_r^{(e)} + Arc(p_l^{(e)})$, the phantom is bended around the axis parallel to **c** and crossing the point of $(\mathbf{c}, \frac{l}{2}, 0)$, shown in Figure 4.13f (left-hand side) as blue arc with $r = 1000$.

In the next step, only required for mimicking an MRI voxel, the phantom is transformed into a local coordinate system (Figure 4.13g). Finally, as shown in Figure 4.13h, a cubic slab which its sides are parallel to the axes of the global coordinate system is extracted from Figure 4.13g to represent an MRI voxel.

ECS can be increased by increasing inter-CMs and/or inter-sheetlet spaces. To increase inter-CMs space, the space between polygons generated in step Figure 4.12.b, needs to increase. The result of increasing inter-CMs space in the phantom is visible by comparing Figure 4.14(a) and 4.14(b). The result of increasing inter-sheetlet space by placing generated sheetlets further apart from each other is distinguishable by comparing Figure 4.14(a) vs. 4.14(c). Finally, the result of increasing inter-CMs space along with inter-sheetlet space is shown in Figure 4.14(d).

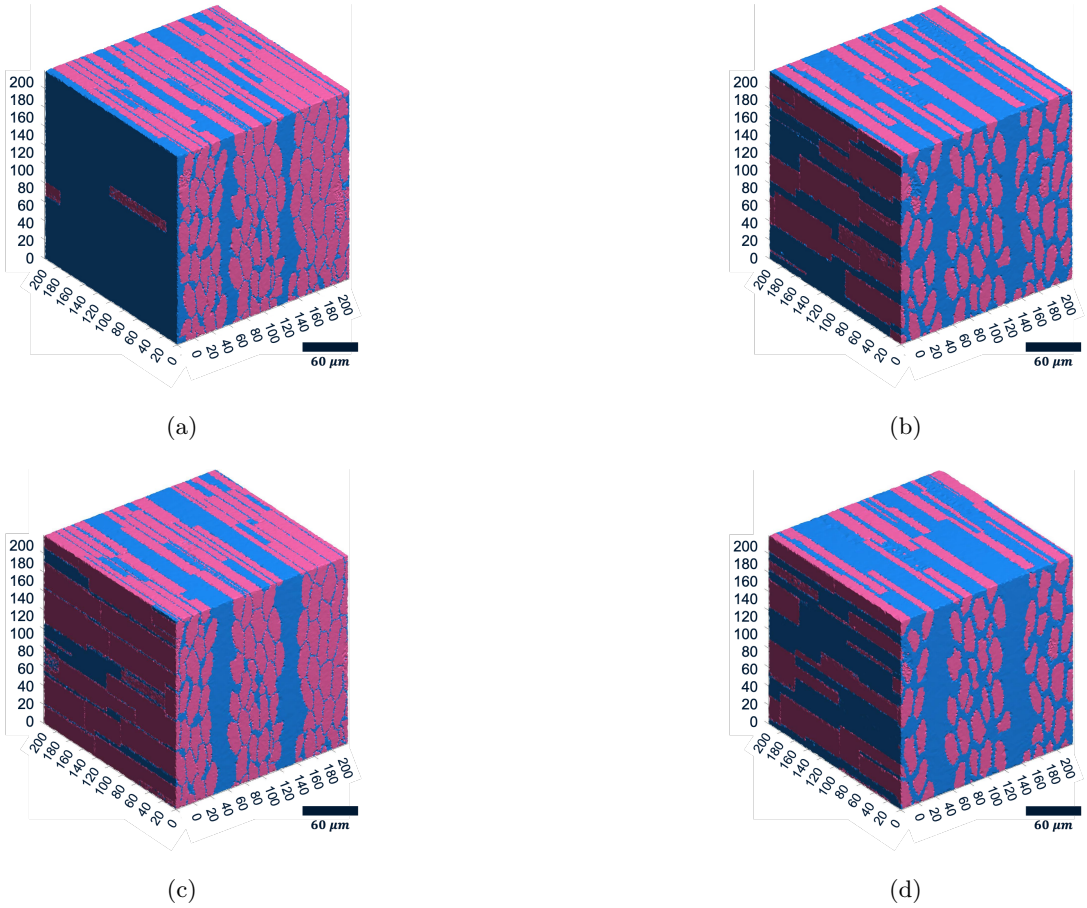

(a) (b) (c) (d)

Figure 4.14: Increase of ECS: a) Initial status, b) Increase of inter-CMs space, c) Increase of inter-sheetlet space, d) Increase of both inter-CMs and inter-sheetlet spaces.

4.6 Experimental Data and Software

4.6.1 Data

The phantom was verified using several voxels of the 3D data acquired in *ex-vivo* rat hearts reported previously [Teh et al., 2016]. Briefly, dMRI data was acquired on a 9.4 T preclinical MRI scanner (Agilent, CA, USA) using a 3D fast spin-echo DW sequence with the following parameters: TR/TE = 250/9.3 ms, echo train length = 8, echo spacing = 4.9 ms, field-of-view = $20 \times 16 \times 16$ mm, resolution = $100 \times 100 \times 100$ µm, diffusion duration (δ) = 2 ms, diffusion time (Δ) = 5.5 ms, number of non-DW images = 8, number of DW directions = 61, and b-value (effective) = 1000 s/mm^2. The

abovementioned values are the same for all the simulations in this work.

4.6.2 Software

All processes including the generation of the numerical phantom, meshing, simulation of dMRI signal, calculation of cDTI parameters, and statistical analysis were carried out in MATLAB (MathWorks, Massachusetts, USA).

iso2mesh

iso2mesh is an open-source MATLAB mesh generation and editing toolbox. It creates a 3D tetrahedral finite element mesh from 3D gray-scale volumetric image, resulting from Section 4.5 [Fang and Boas, 2009, Tran et al., 2020]. The different compartments of the numerical phantom i.e., CMs' groups, ECS, and collagens are labelled differently in the resultant mesh. These labels enable the FEM-based dMRI simulator to resolve diffusivity and relaxation assigned to each compartment, along with permeability between them for the simulation.

SpinDoctor

Here, to simulate the dMRI signal, the SpinDoctor simulator Li et al. [2019], which solves the Bloch-Torrey PDEs using the FEM, is used.

For all simulations, the ordinary differential equation (ODE) is solved using theta time stepping method (generalized midpoint) [Stuart and Peplow, 1991], with the following parameter setup of SpinDoctor toolbox:

- *implicitness* = 0.5: calls Crank Nicolson method [Stuart and Peplow, 1991];
- *timestep* = 5 µs: timestep for iterations.

4.7 Experiments and Results

The quality of the proposed numerical phantom was evaluated in the following experiments: (a) qualitative/visual comparison of *in-silico* CMs and myocardial tissue with their real counterparts; (b) comparison of the shape of *in-silico* CMs with real CMs, using a virtual morphometric study; (c) comparison of microstructure complexity of the *in-silico* tissue against histology; and d) verification of cDTI parameters of the

simulated cDTI with their experimental counterparts from *ex-vivo* measurements. The list of tunable parameters for the simulation of cDTI can be found in Table 4.3

4.7.1 Qualitative Comparison of *in-silico* CMs with Real Myocardium Experimental Data

This experiment aims to compare the *in-silico* version of: (i) single CMs, Figure 4.15(a); along with (ii) transverse cross-section, Figure 4.15(b); and (iii) longitudinal cross-section, Figure 4.15(c), of the myocardial tissue with their real counterparts using histological and confocal microscopy images. Visual assessment of individual CMs and cross-sectional images from tissue histology and the *in-silico* phantom indicate good agreement between the former and the latter.

4.7.2 Morphometric Study of Virtual CMs

This experiment evaluates how the PDFs from literature, used as inputs, are preserved following phantom generation. The virtual morphometric study is performed on 20 different numerical phantoms generated according to the PDFs shown in Table (4.3), each comprising 642 virtual CMs. For each numerical phantom, all processes of phantom generation are repeated from the beginning. The input PDFs are made on assumptions that the value reported (mean±standard deviation) in literature comes from a normal distribution. For each numerical phantom, all processes of phantom generation are repeated from the beginning. The volume V, length L, and profile $Area$ ($Area$ is defined as the maximum area of the 2D projection of virtual CMs on the plane parallel to the major-axis and perpendicular to the minor-axis of 2D polygons) are directly measured. Then, CM's major-axis A is calculated from $A = \frac{Area}{L}$, and consequently, CM's minor-axis B is measured using microstructural restriction density, the volume formula for an elliptical cylinder, $V = \pi ABL$, as explained in [Chen et al., 2007]. Figure 4.16 illustrates an example of the input and output PDFs of the CMs' shape parameters.

In this experiment, two null hypotheses are tested: first, the output PDFs follow a normal distribution; second, there is no significant difference between the input and output PDFs. The Shapiro-Wilk test tests the first null hypothesis, commonly used to test whether PDFs come from a normal distribution or not [Ahad et al., 2011, Nayak and Hazra, 2011]. The Mann-Whitney U-test tests the second null hypothesis if the first null hypothesis is rejected; otherwise, it is tested by the t-test. Moreover, to

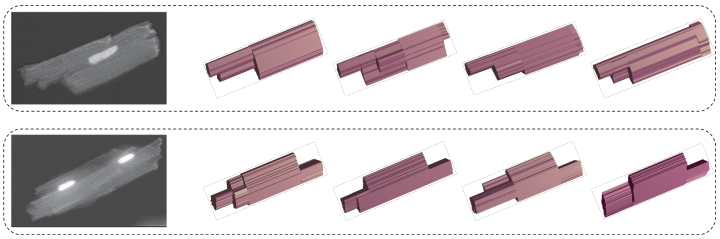

(a)

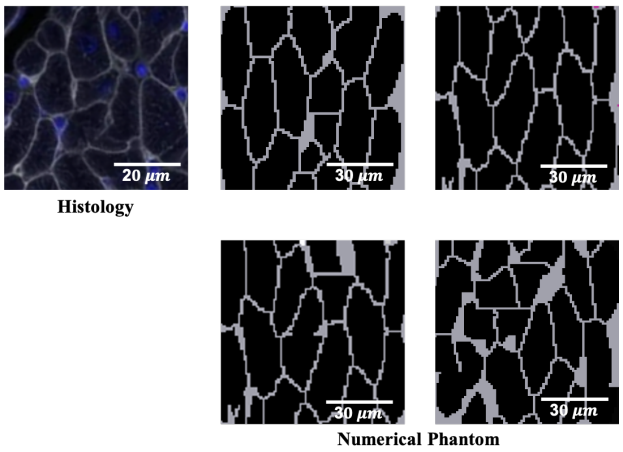

(b)

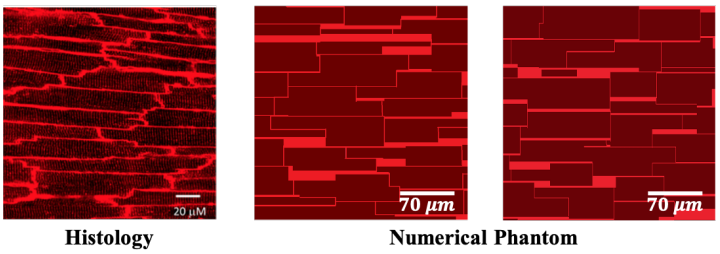

(c)

Figure 4.15: Comparison between *in-silico* and real myocardial tissue. a) Comparison between EM image of single CMs [Bensley et al., 2016] with *in-silico* CMs (the blues are microvasculature), b) Comparison between the transverse cross-section of myocardial tissue in a confocal microscopy image and an *in-silico* version of tissue, c) Comparison between the longitudinal cross-section [Chen et al., 2015] of myocardial tissue in a confocal microscopy image and an *in-silico* version of tissue.

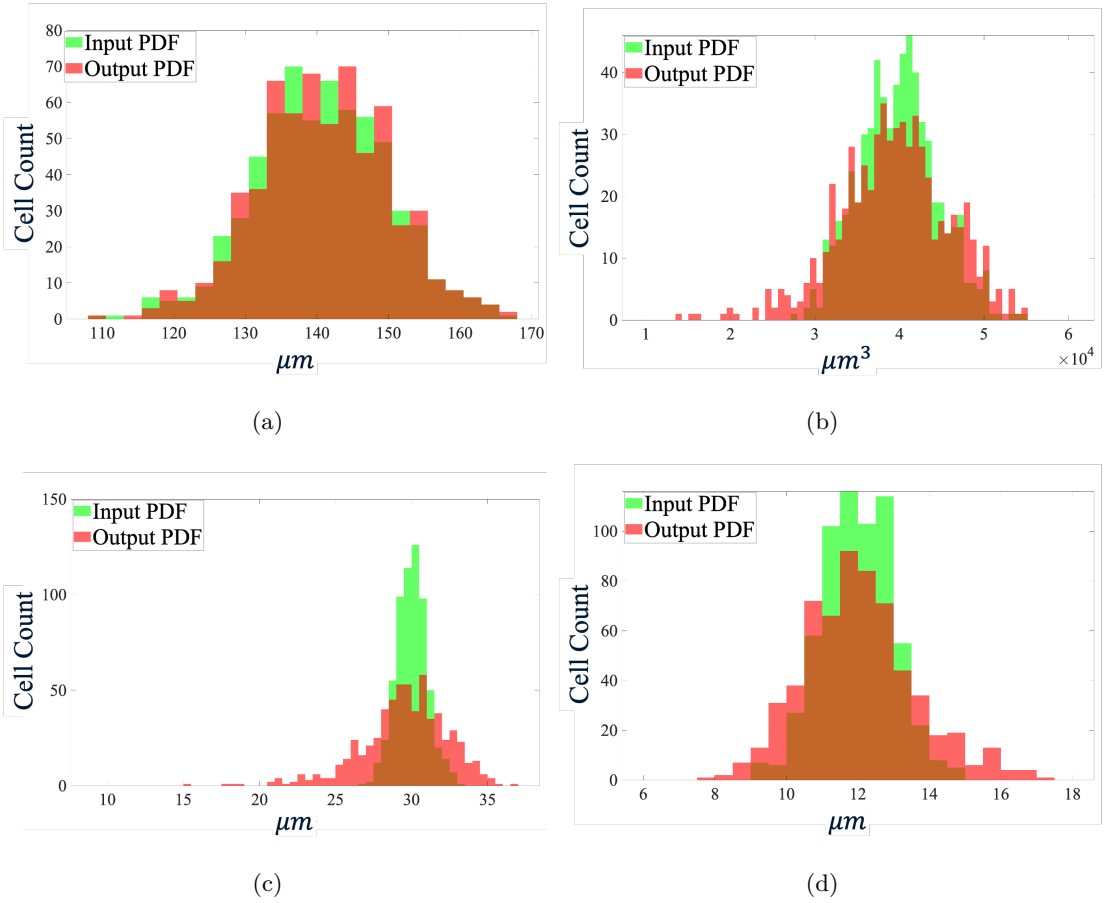

Figure 4.16: Comparison between the input and output PDFs of the CMs' shape parameters. a) Length L, bin size of 2.5 μm b) Volume V, bin size of 806 μm^3 c) Major-axis A, bin size of 0.5 μm d) Minor-axis B, bin size of 0.5 μm.

compare the variance of the PDFs, the null hypothesis that the input and output PDFs have equal variances is tested using a two-sample F-test if both PDFs have a normal distribution, and a Brown-Forsythe test if one of the PDFs does not follow a normal distribution. Table 4.2 presents these statistical tests and a comparison between the input and output data. Data are expressed as mean ± SD and are compared using the Shapiro-Wilk test, Mann-Whitney U-test, t-test, two-sample F-test, and Brown-Forsythe test.

The resultant p values for the Shapiro-Wilk test, p_1-values in Table 4.2, indicate that the proposed method preserves normality for the length and volume PDFs but does not for major- and minor-axis PDFs. These results are coupled with instance histograms are shown in Figure 4.16, where the length and volume of output PDFs (red bars in Figures 4.16(a) and 4.16(b)) are symmetric around their means, whereas it does not hold for PDFs of the major- and minor-axis (red bars in Figures 4.16(c) and 4.16(d)). Moreover, the null hypothesis of no statistically significant difference between input and output PDFs is confirmed based on the p_2- and p_3-values. Finally, according to p_4- and p_5-values, the null hypothesis of the equal variances for input and output PDFs only fails to reject for length PDF.

4.7.3 Microstructural complexity of the *in-silico* tissue

This experiment investigates the similarity between the structural universality classes of the *in-silico* myocardial tissue and the histological data from real tissue. Novikov et al. [2014] classified the microstructure into different *structural universality classes* based on the unique types of long-scale spatial correlations of a medium at the microscale. The criterion for this classification is the exponent p in $\Gamma(k)|_{k\to 0} \sim k^p$, which describes the long-range fluctuations of microstructural restriction density. $\Gamma(k)$ is radially averaged of the power spectrum density ($PSD(u,v)$) of the tissue microstructure around $k = 0$, where $k = \sqrt{u^2 + v^2}$ [Lee, 2019]. According to Wiener-Khinchin theorem, $PSD(u,v)$ can be found using the Fourier transform of the autocorrelation function [Lathi, 1998]:

$$PSD(u,v) = \sum_{x=0}^{M-1} \sum_{y=0}^{N-1} C(x,y) e^{-j2\pi(\frac{ux}{M} + \frac{vy}{N})} \tag{4.1}$$

where $C(x,y)$ is the autocorrelation of a 2D image, $I(x,y)$, $0 < x < M$, $0 < y < N$.

Here, the value of $\Gamma(k)$ for the *in-silico* and histological images of the myocardial transverse cross-section (in the plane perpendicular to the long axis of CMs) are com-

Table 4.2: Statistical tests and comparison between the input and output means ± SD of the CMs' shape parameters: Length L, Volume V, Major-axis A, and Minor-axis B.

	$L(\mu m)$	$V(\mu m^3)$	$A(\mu m)$	$B(\mu m)$
Input	141.1 ± 9.3	$39,933 \pm 4,640$	30.1 ± 1.1	11.1 ± 1
Output	141.1 ± 9.4	$39,732 \pm 6,693$	30.2 ± 2.9	11.9 ± 1.6
p_1	$0.28 > 0.01$	$0.17 > 0.01$	$0 < 0.01$	$0 < 0.01$
p_2	-	-	$0.09 > 0.01$	$0.19 > 0.01$
p_3	$0.99 > 0.01$	$0.76 > 0.01$	-	-
p_4	$0.98 > 0.01$	$10^{-18} < 0.01$	-	-
p_5	-	-	$10^{-53} < 0.01$	$10^{-18} < 0.01$

Values are mean ± SD for 642 CMs from 20 phantoms.

p_1, p_2, p_3, p_4, and p_5 are the results of the Shapiro-Wilk test, Mann-Whitney U-test, t-test, two-sample F-test, and Brown-Forsythe test, respectively. A value of $p < 0.01$ is considered statistically significant.

pared as shown in Figure 4.15(b). Figure 4.17 depicts the diagrams of $\Gamma(k)$ for these images, at the different k. As illustrated in Figure 4.17, at $k < \frac{1}{CM's\ minor-axis}$ i.e., $k < \frac{1}{12}$, the diagrams of the *in-silico* tissue follow the same power-law tail of the real tissue, i.e., k^0.

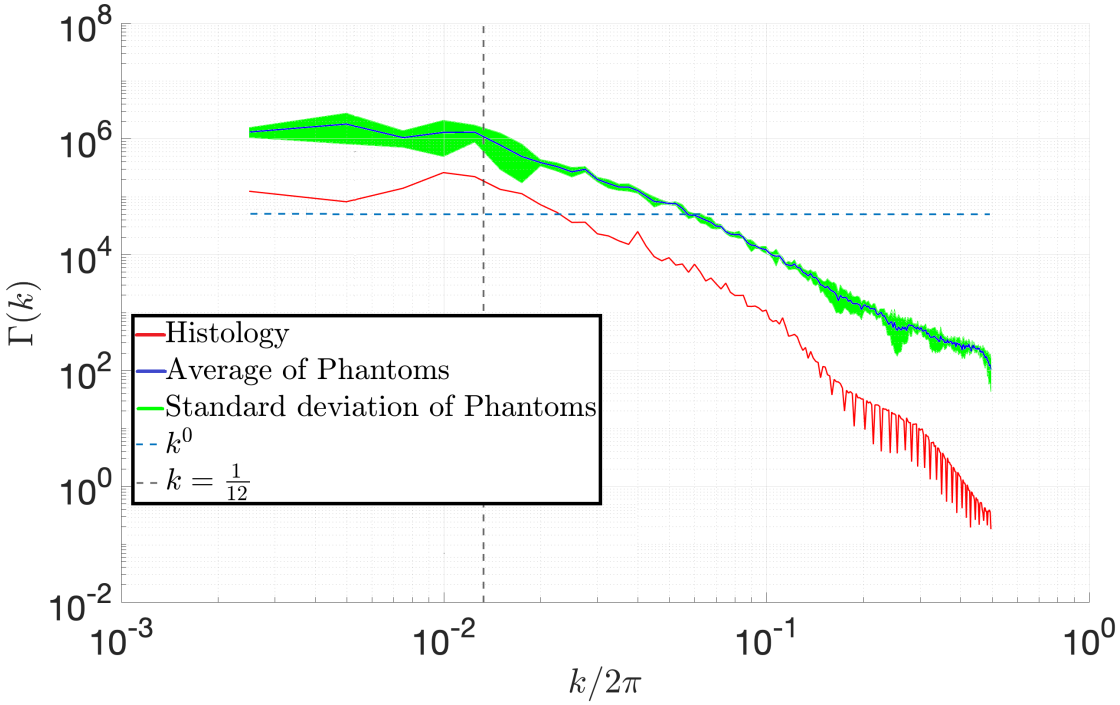

Figure 4.17: $\Gamma(k)$ for 2D images of the cross-sections of the *in-silico* and real myocardial tissues shown in Figure 4.15(b).

4.7.4 Mesh Analysis

This experiment aims to find the coarsest tetrahedral mesh used to generate the phantom, at which the simulated signal becomes independent of the mesh resolution. The mesh independence is evaluated by generating successively finer resolution of tetrahedral meshes for the domain of interest until the changes in the simulated signal become negligible. The number of tetrahedral elements at which this mesh independency is observed is employed for all subsequent simulations. Due to considerable memory requirements for higher b-values, the analysis is limited to the lower b-value of $b = 0$ (s/mm^2) and $b = 100$ (s/mm^2). All imaging parameters of the simulation are

set as described in Section 4.6.1, except diffusion encoding direction, which is set in the direction of the z-axis. Figure 4.18 shows mesh analysis for a $100 \times 100 \times 100$ (μm^3) phantom where changes in magnetisation and elapsed time for solving Bloch-Torrey equation are evaluated versus the phantoms generated by more refined tetrahedral elements (or more tetrahedral elements) at $b = 0$ (s/mm^2) and $b = 100$ (s/mm^2).

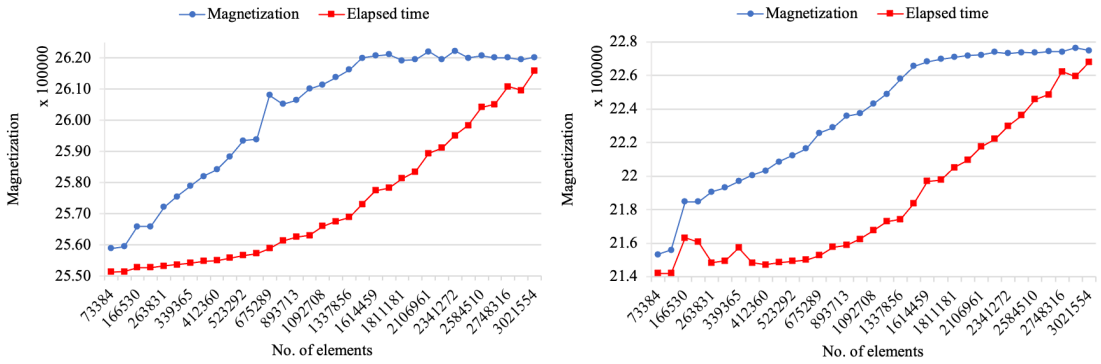

(a) (b)

Figure 4.18: Mesh Analysis: dependency of magnetisation to mesh resolution at: a) $b = 0$ (s/mm^2) b) $b = 100$ (s/mm^2)

According to Figure 4.18, the maximum number of tetrahedral elements at which the simulation result is approximately independent of mesh resolution is 1486993, which is achieved by setting the following parameters in iso2mesh:

- opt.radbound = 6: The maximum surface element size.
- opt.angbound = 30: The minimum angle of a surface triangle.
- opt.distbound = 0.45: The maximum distance between the center of the surface bounding circle and centre of the element bounding sphere.
- opt.reratio = 3: The maximum radius-edge ratio.
- maxvol = 5: The target maximum tetrahedral element volume.

4.7.5 cDTI MRI Measurements vs. Phantom-based Simulations

This experiment investigates the performance of numerical phantom in replicating cDTI eigenvectors and eigenvalues using a simplified version of the numerical phantom. The

reason for this simplification is the lack of information about the chamber curvature and myocardial tissue twisting of the *ex-vivo* data. Therefore, I discarded these features during the generation of the numerical phantom. Moreover, collagen fibres are not included in the numerical phantom, since the *ex-vivo* cDTI is measured from a healthy heart, where the collagen VF is $\sim$ 2% [Haddad and Samani, 2017]. Due to lack of information about inter-CMs space, this parameter was set 1 µm.

cDTI eigenvectors correspond to CMs and sheetlets directions [Magat et al., 2021, Tseng et al., 2003]. Therefore, how the simulated eigenvectors preserve the input directions are investigated. First, I generated 100 *in-silico* voxels at the resolution of *ex-vivo* data, described in Section 4.6.1, (the mesh resolution determined in Section 4.7.4) and VF_{ic} of the generated voxels fell into the range of 64-74%, with 69%±2% (mean±SD). Then, the directions of CMs and sheetlets of these voxels are oriented according to the eigenvectors of the voxels of an equivalent cDTI experiment, selected randomly from different myocardial regions (Figure 4.19(a)). Finally, the biophysical parameters of the *in-silico* voxels are set up according to the information provided in Table 4.3.

As shown in Table 4.3, the eigenvectors of *in-silico* voxels are exactly matched to the eigenvectors of the *ex-vivo* data. $T_{2_{ex}}$ is set 42.4 ms, water T_2 measured in the field strength of 9.4 T [Lei et al., 2003]. Then, $T_{2_{ic}}$ is computed by assuming $T_{2_{ic}} \times VF_{ic} + T_{2_{ex}} \times VF_{ex} = T_{2_{ex-vivo}}$ where $T_{2_{ex-vivo}} = 25.72$ ms is the average value of T_2 for 100 selected *ex-vivo* voxels. Similarly, D_{ex} is set 1.91 µm^2/ms, free water diffusivity reported in [Periquito et al., 2019], due to similar temperature during the acquisition in [Periquito et al., 2019] and the *ex-vivo* data under comparison [Teh et al., 2016]. Then, D_{ic} is computed by assuming $D_{ic} \times VF_{ic} + D_{ex} \times VF_{ex} = D_{ex-vivo}$ where $D_{ex-vivo} = 1.06$ µm^2/ms is the average diffusivity for 100 selected *ex-vivo* voxels. Since $D_{ex-vivo}$ is reduced by CMs' geometry, the computed D_{ic} needs to increase to offset the effect of CMs' geometry. Due to a lack of quantitative information about diffusivity reduction caused by CMs' geometry, different values of D_{ic} are assessed to achieve the best possible agreement between eigenvalues of the *in-silico* and *ex-vivo* measurements for 16 voxels, chosen randomly. According to this assessment, the best possible D_{ic} is achieved by 20% increase i.e., 0.83 µm^2/ms, and set in the simulation for the remaining voxels.

Other input parameters used for cDTI simulations were taken from published *ex-vivo* data in the literature. Afterward, dMRI signal is simulated for 100 *in-silico* voxels

Table 4.3: Phantom parameters for healthy myocardium

	$L(\mu m)$	$V(\mu m^3)$	$A(\mu m)$	$B(\mu m)$	$D_{ic}(\mu m^2/ms)$	$D_{ex}(\mu m^2/ms)$	$T_{2_{ic}}(ms)$	$T_{2_{ex}}(ms)$
Literature	$N(141.1 \pm 9.3)$ [Chen et al., 2007]	$N(39933 \pm 4640)$ [Chen et al., 2007]	$N(30.1 \pm 1.1)$ [Chen et al., 2007]	$N(11.1 \pm 1)$ [Chen et al., 2007]	0.83	1.91	18.4	42.4
ex-vivo	NA	NA	NA	NA	NA	NA	NA	NA
	$\kappa_{Sarco.}(\mu m\, s^-$	$\kappa_{ICDs}(\mu m\, s^-$	$p_r(m^{-1})$	$p_l(m^{-1})$	$\alpha(Â°)$	$V_1(Â°)$	$V_2(Â°)$	$V_3(Â°)$
Literature	15 [Bates et al., 2017]	0.5 [Bastide et al., 1996]	NA	NA	NA	-	-	-
ex-vivo	NA	NA	NA	NA	NA	AVL	AVL	AVL
Literature	~2-4 CMs thick [Hales et al., 2012].	NA	~1-2 CMs thick [LeGrice et al., 2005]	65-75% [Greiner et al., 2018, Skepper and Navaratnam, 1995]	~ 2% [Haddad and Samani, 2017]	NA	NA	
ex-vivo	NA	NA	NA	NA	NA	NA	NA	

	Sheetlet thickness (µm)	inter-CMs space (µm)	inter-sheetlet space (µm)	VF_{ic} (%)	$VF_{collagen}$ (%)	$D_{collagen}$ ($\mu m^2/ms$)	$T_{2_{collagen}}$ ($\mu m\, s^{-1}$)

AVL: available, NA: not available.

by setting the imaging parameters of simulation such as b-values, diffusion encoding directions, diffusion time, diffusion encoding gradient type and etc. as same as *ex-vivo* data, described in Section 4.6.1. Finally, for each *in-silico* voxel, the eigenvectors, eigenvalues, and FA of cDTI are computed and compared with their counterpart from *ex-vivo* data.

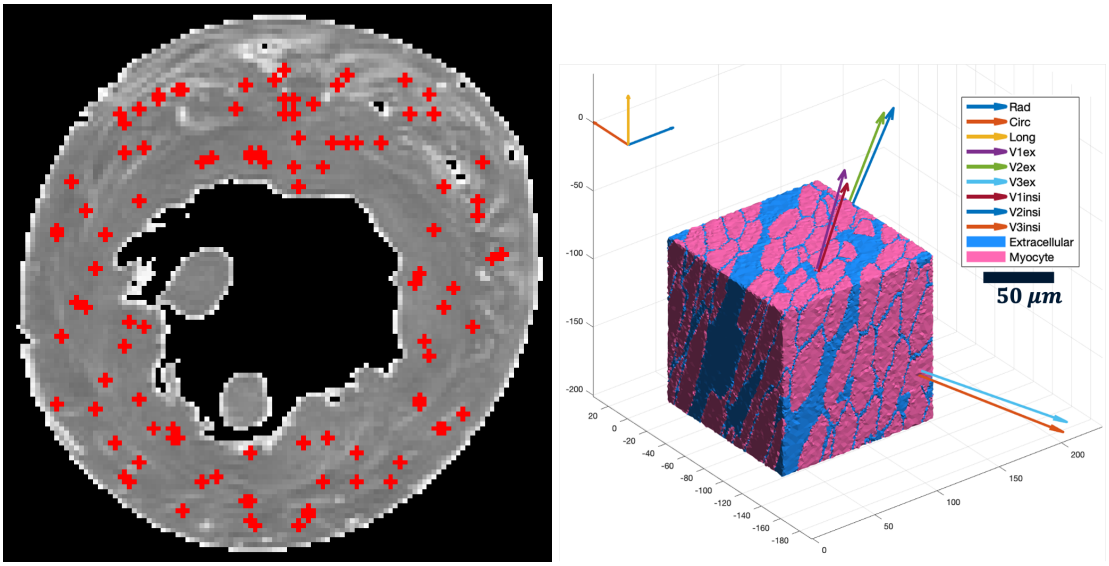

(a) (b)

Figure 4.19: a) Location of mimicking voxels in a slice of experimental cDTI, b) An example of *in-silico* voxel oriented according to voxel 8 in (a).

Figures 4.20 and 4.21 show the distribution of the angular distance between eigenvectors, along with the absolute angle difference between HA, TA, SA, and SE of the input and simulated ones in rose diagrams. The mean and standard deviation (SD), along with median and median absolute deviation (MAD) for these distributions are reported under each diagram. These angular distance and absolute angle differences are much smaller than those reported between cDTI and structural tensor imaging (STI) [Bernus et al., 2015] shown in Table 4.4, or reported in [Haliot et al., 2019]. In addition, as illustrated in the Bland-Altman plots in Figures 4.22(a), 4.22(b), 4.22(c), and 4.22(d), there is an adequate agreement between HA, TA, SE and SA of the *ex-vivo* data and the numerical phantoms.

Additionally, the simulated eigenvalues, mean diffusivity (MD), fractional aniso-

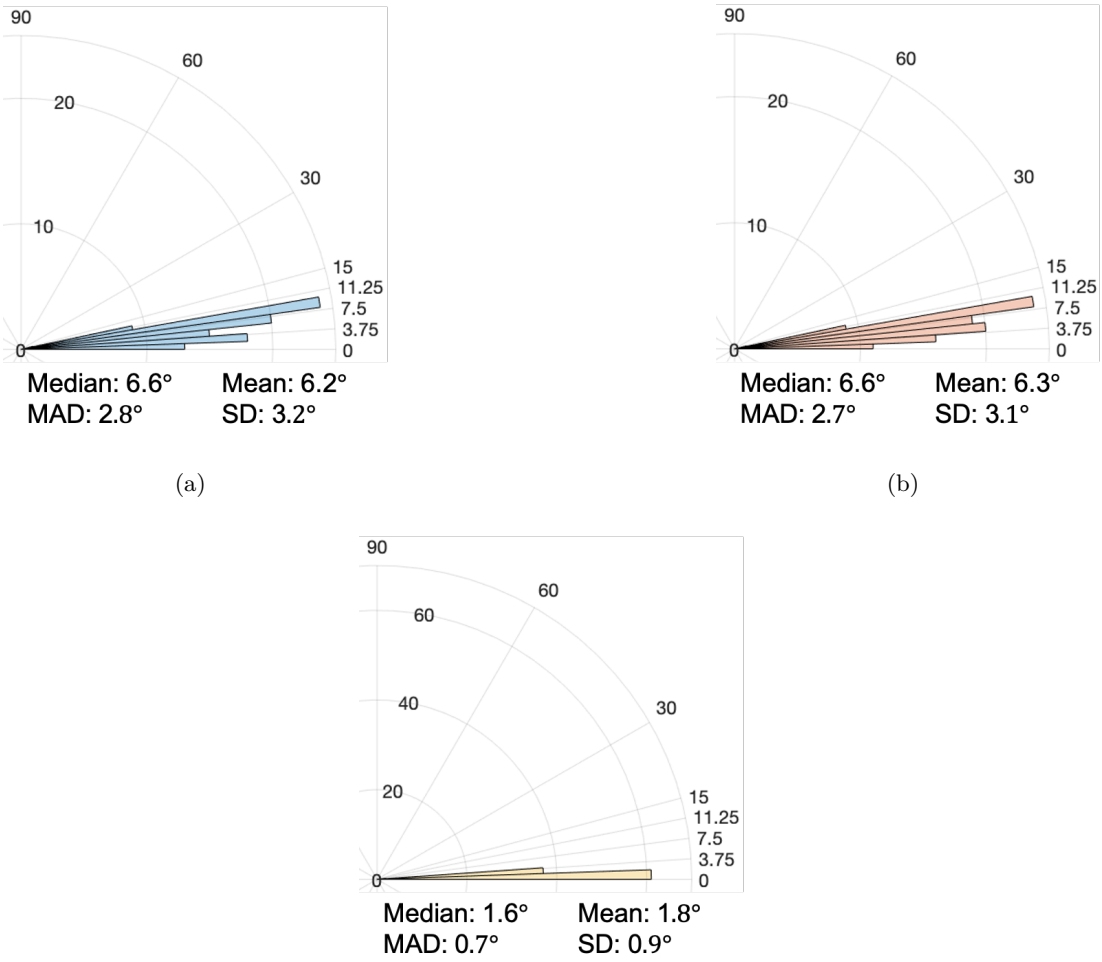

Figure 4.20: Angular distance between a) V_1, b) V_2, and c) V_3 of *ex-vivo* and *in-silico* voxels.

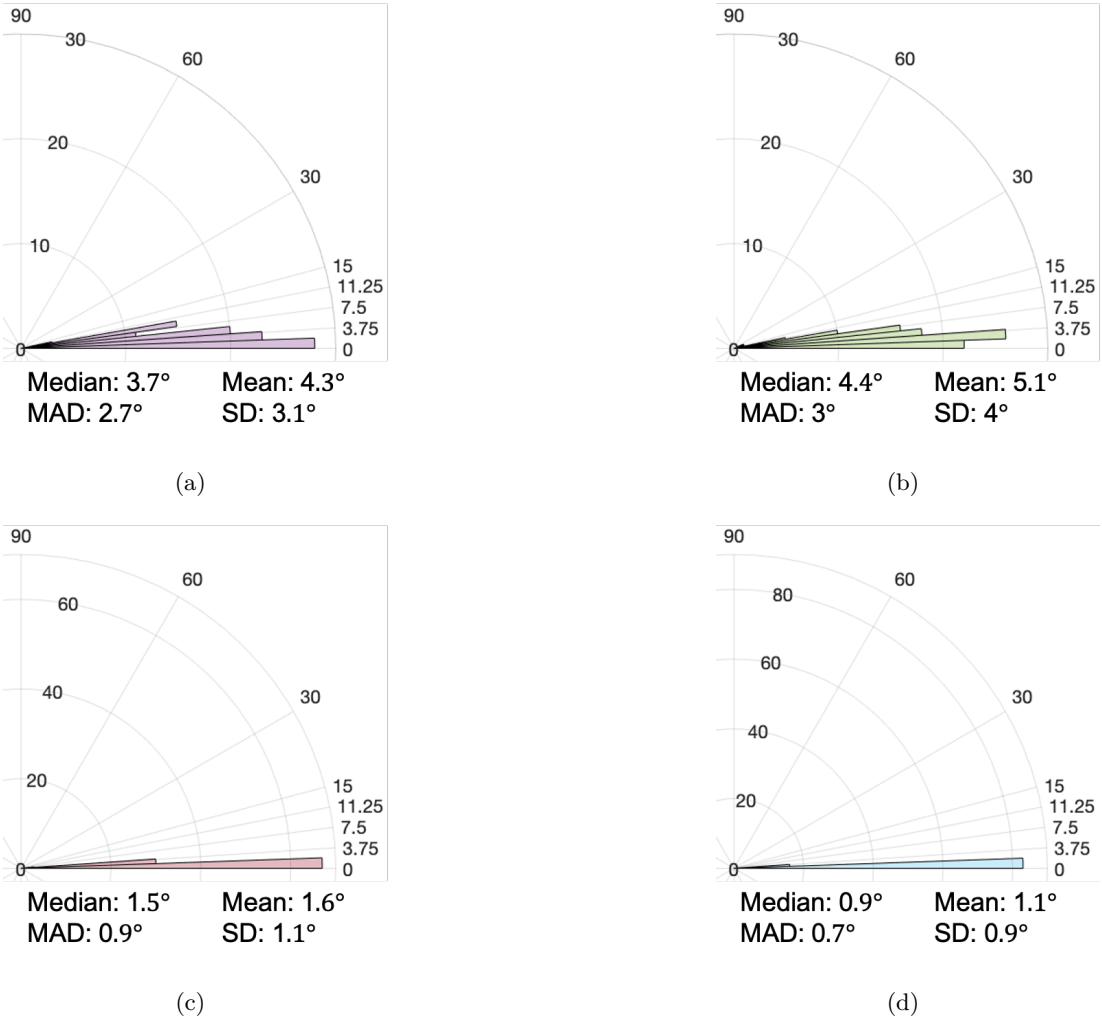

Figure 4.21: Absolute angle difference between a) HA, b) TA, c) SA, and d) SE of *ex-vivo* and *in-silico* voxels.

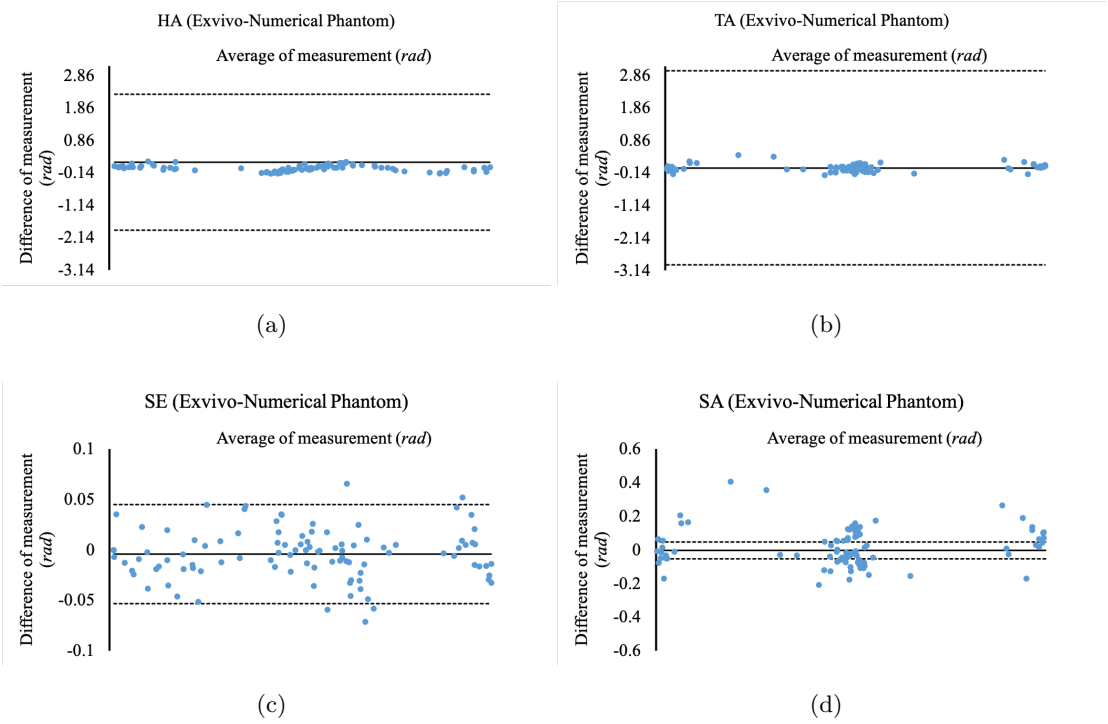

Figure 4.22: a) Comparison between sheetlet angles of the experimental data and numerical phantom. Agreement between a) HA; b) TA; c) SE and d) SA of the experimental data and numerical phantom.

Table 4.4: Angular distance and absolute angle difference (median±MAD) between eigenvectors and sheetlet angles of *ex-vivo* and *in-silico* voxels.

		V_1°	V_2°	V_3°	HA°	TA°	SE°	SA°
Septal	∠input vs. ∠*in-silico* DTI	7.1 ± 3.1	7.3 ± 2.9	1.3 ± 0.7	5.8 ± 3.1	3 ± 3.9	0.6 ± 0.6	1.1 ± 0.9
	∠STI vs. ∠DTI	13.3±6.7	32.9 ± 19.6	27.9 ± 17.4	8.5 ± 5.6	11.5±7.8	22 ± 16.2	22.9 ± 16.5
Lateral	∠input vs. ∠*in-silico* DTI	4.7 ± 3.1	4.9 ± 3	2.2 ± 0.8	2.4 ± 3.1	4.4 ± 1.7	1.2 ± 0.9	1.7 ± 0.9
	∠STI vs. ∠DTI	12.6±5.9	15 ± 8.5	23.8 ± 11.9	9.1 ± 5.8	15.6 ± 11.1	16.1 ± 10.5	14.6 ± 10.3

tropy (FA), and radial diffusivity (RD) are shown along with the eigenvalues of the *ex-vivo* data in Figure 4.23. For these parameters two null hypotheses are tested: first, the distribution of the cDTI parameters for the experimental and simulation follows a normal distribution; second, there is no significant difference between the distribution of cDTI parameters of the experimental and simulated data. These hypotheses are tested as in Section 4.7.2 and their results are presented in Figure 4.23 above each box and whisker plot.

Computational cost

The computations for Section 4.7.5 simulations were performed on ARC3, the high-performance computing facilities at the University of Leeds. ARC3 consists of 252 nodes with 24 cores (Broadwell E5-2650v4 CPUs, 2.2 GHz) and 128GB of memory each and an SSD within the node with 100GB of storage. The details of computational cost for undertaken simulations in Section 4.7.5 is reported in Table 4.5.

4.7.6 Effect of collagen density, twisting, and bending on MD and FA

As mentioned earlier, due to insufficient information about the twisting and curvature of the myocardial wall along with the lack of information about the diffusivity and relaxation of collagenous ECS, these structures are excluded in the simulation presented in Section 4.7.5. The goal of the following experiment is to identify the effect of these structures on cDTI derivatives individually. To this effect, cDTI for each structure's different range of values is simulated. Increasing collagen density decreases diffusivity and relaxation [Bun et al., 2012, Loganathan et al., 2006, Mewton et al., 2011]. Figures 4.24(a) and 4.25(a) show that a decrease in diffusivity and relaxation values leads to a reduction in MD and FA. Here, the effect of these changes on simulated signals for four pairs of values of diffusivities, $D_{collagen} \in [D_{ex}, D_{in}]$, and relaxations, $T_{2_{collagen}} \in [T_{2_{ex}}, T_{2_{in}}]$, are illustrated respectively.

The degree of wall twisting and curvature depends on the studied cardiac phase. In the transition from systole to diastole, the degree of the twisting increases [Streeter Jr et al., 1969], whereas the curvature decreases. To show the effect of these geometrical changes on MD and FA, cDTI is simulated using an *in-silico* voxel, mimicking transiting from systole to diastole at four points, where $\alpha^\circ \in [0, 60]$ and $p_l, p_r \in [0.31\,\mathrm{mm}^{-1}, 0.01\,\mathrm{mm}^{-1}]$ [Ferferieva et al., 2018], respectively. Figures 4.24(b) and

Table 4.5: Computational cost of the simulation

Average number of tetrahedrons per voxel	Number of cores per voxel	Memory per core (GB)	Computational time per core (hours)	Entire Number of cores	Computational time for entire voxels (core hours)
856570±48666	7	62	6±2.5	700	4152

4.25(b); and Figures 4.24(c) and 4.25(c) show the simulated values of MD and FA, respectively, increase by decreasing the curvature and increasing the twisting, which agrees with changes in the *in-vivo* measurement of MD and FA [Khalique et al., 2020, McGill et al., 2014]. The observation in Figure 4.25(b) is somewhat surprising as FA values increase by increase of twisting, as it is expected that FA values decrease with increase in the range of CMs orientation resulting from increased twisting. One possible explanation for this observation is that the increase in the tissue twisting leads to a decrease in CMs' diameters [Axel et al., 2014, Nielles-Vallespin et al., 2017] which increases FA values. The same reason may explain why increase in tissue bending results in increasing FA values (Figure 4.25(c)).

4.7.7 Effect of adding obstacles into ECS on reduction in secondary eigenvalue

To support the argument about the role of non-CM compartments and tortuous structure of inter-sheetlet space in reduction of λ_2, several simulations were run over multiple 3D simplified versions of myocardial *in-silico* phantoms with different density of the obstacles in ECS. Figure 4.26 shows simplified phantoms where light blue is ECS, and pink and dark blue represent the CMs and obstacles, respectively. In these phantoms, both CMs and obstacles have cuboid shapes. The phantom oriented in space, where the CMs and obstacles were parallel to the **z**-axis, and sheetlets were perpendicular to the **y**-axis. In Figure 4.26(b) and 4.26(d) obstacles are only placed in inter-sheetlet space, whereas in Figure 4.26(c) and 4.26(e) obstacles are also added into inter-CM space.

In these experiments, parameters of the phantoms and simulations were similar to the experiment in Section 4, but spins were encoded in 12 directions. Moreover, CMs and obstacles share the same values for diffusivity, T_2 relaxation, and permeability. As illustrated in Figure 4.26, the resulting eigenvectors for each phantom are oriented correctly, and adding the obstacles does not change their orientation, at least in the case of these simplified phantoms. Table 4.6 shows eigenvalues for the phantoms in Figure 4.26 along with their percentage change with respect to the initial phantom in Figure 4.26(a), where there are no obstacles in ECS. In all phantoms, the eigenvalues reduce, and the reduction in λ_2 is two times larger than the reduction in λ_1 and λ_3. Interestingly, in Table 4.6 it can be observed that the reduction in both λ_1 and λ_3 is the same for all phantoms, e.g., $\Delta\lambda_1 = \Delta\lambda_3$. Therefore, it is possible to hypothesise

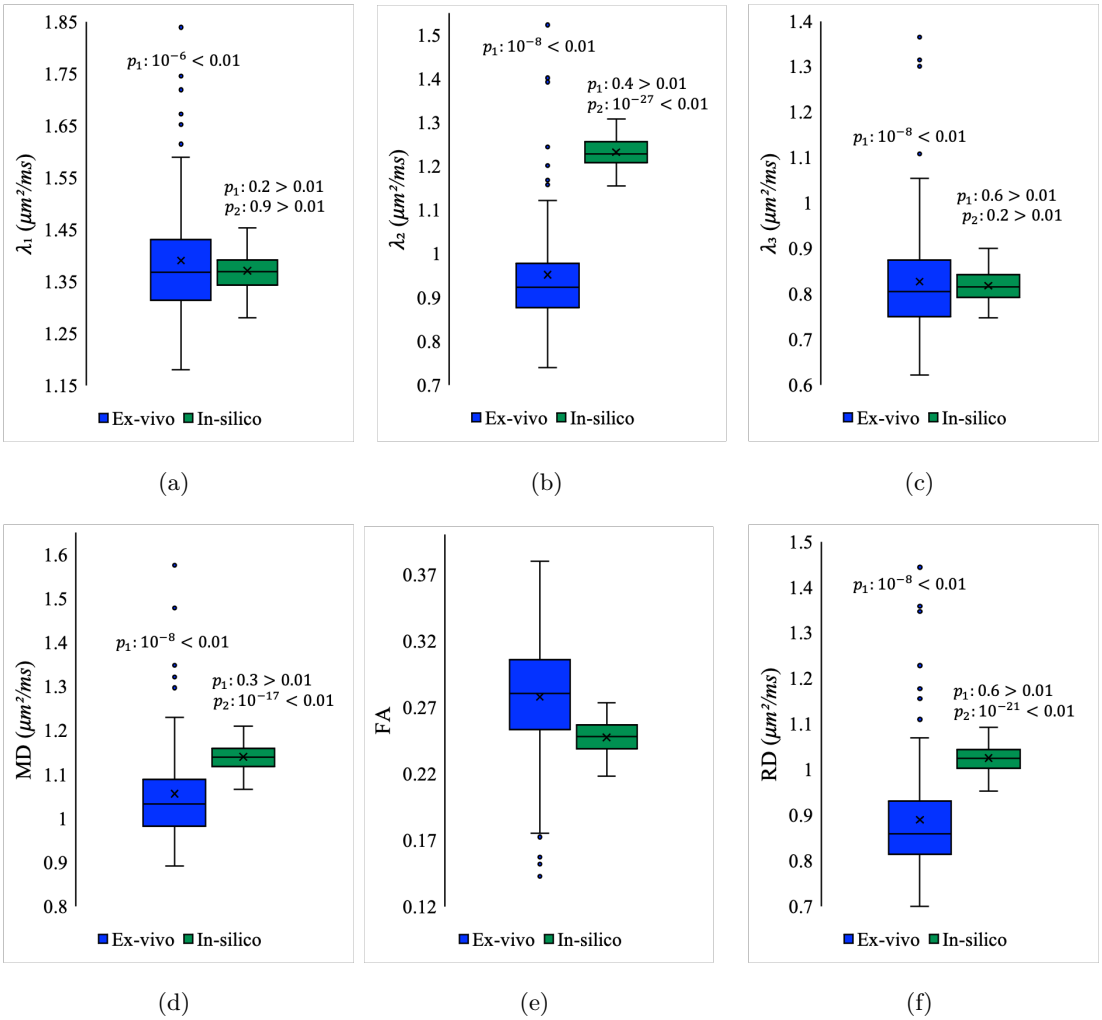

Figure 4.23: Comparison between cDTI parameters of the experimental (blue whisker plots) and *in-silico* data (green whisker plots). Agreement between a) λ_1; b) λ_2; c) λ_3; d) MD; e) FA; f) RD of the experimental data and numerical phantom.

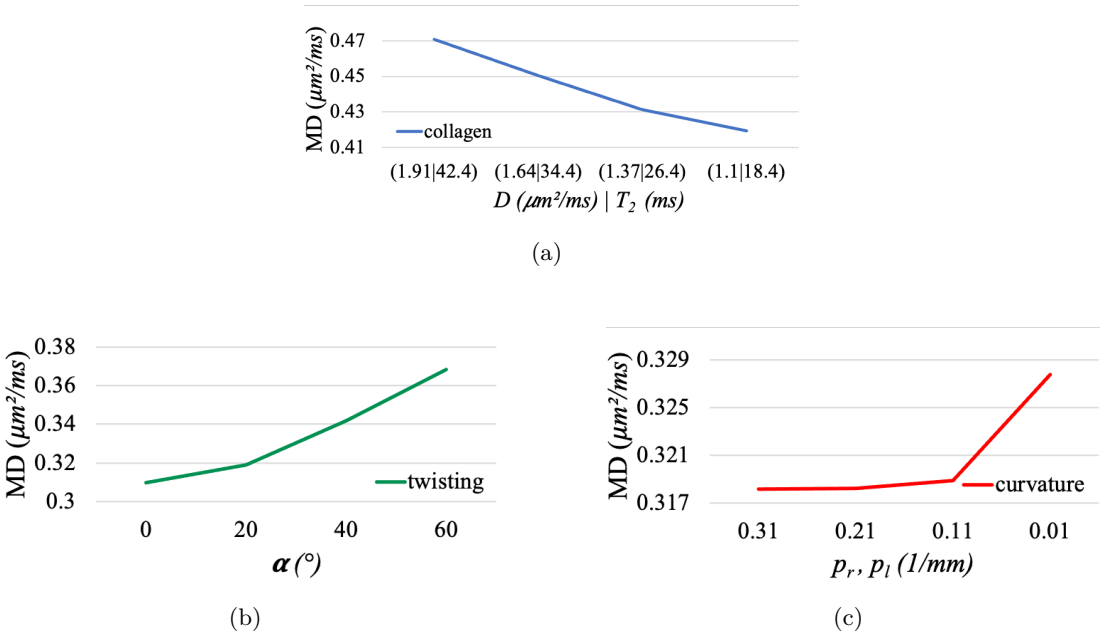

Figure 4.24: Effect of a) increase in collagen density, b) increase in twisting, and c) decrease in curvature on MD.

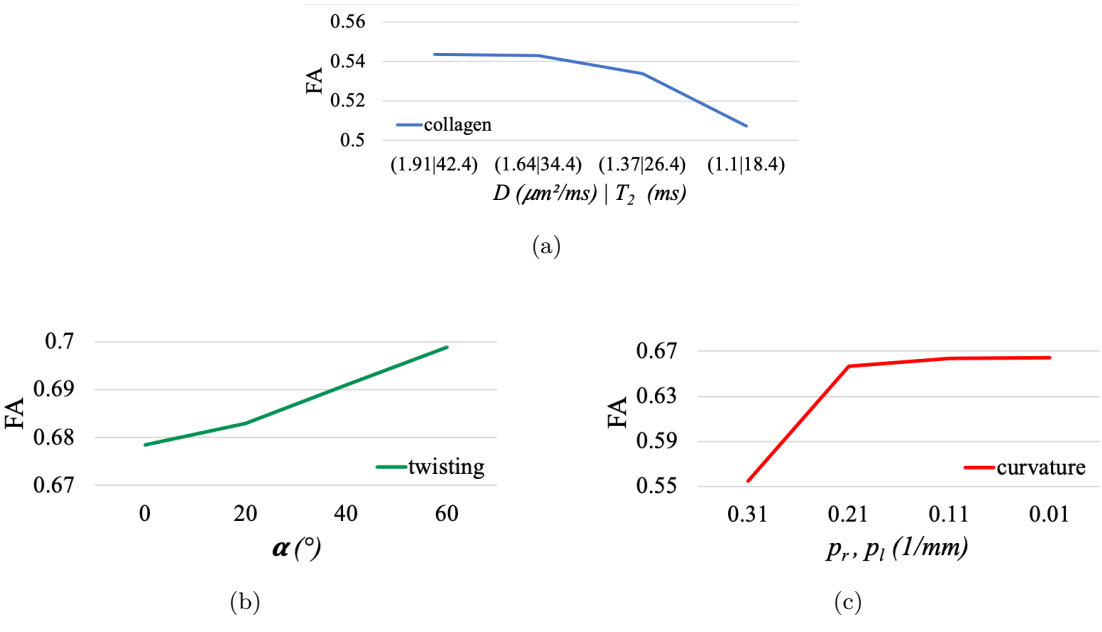

Figure 4.25: Effect of a) increase in collagen density, b) increase in twisting, and c) decrease in curvature on FA.

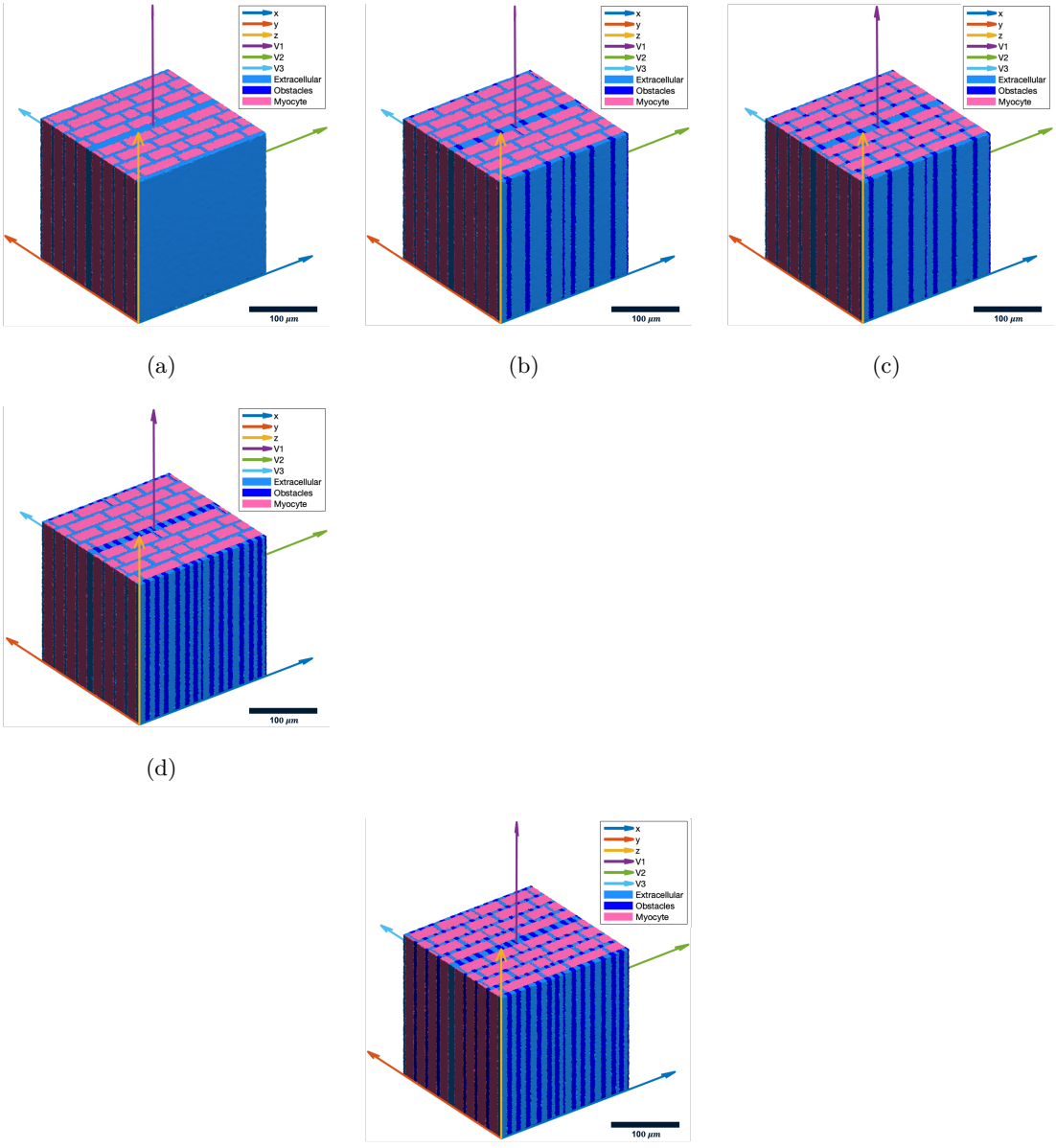

(a) (b) (c)

(d)

(e)

Figure 4.26: Simple phantom mimicking myocardial microstructure (light blue: ECS, pink: CMs) to investigate the effect of adding obstacles (dark blue) into the ECS on eigenvalues.

that these conditions are more likely to occur for the proposed *in-silico* phantom by adding the obstacles.

However, as mentioned earlier, including the above-mentioned obstacles reduces all eigenvalues, whereas only a reduction in λ_2 is of interest. Therefore, to preserve matching between λ_1 and λ_3, ICS diffusivity should increase to offset the reduction in λ_1 and λ_3, while more reduction in λ_2 is likely to lead to matching between λ_2 of *in-silico* and *ex-vivo* data. This can be demonstrated by comparing λ_1 and λ_3 of phantoms (c) and (d) computed by ICS diffusivity of $1\,\mu m^2/ms$, shown in Table 4.7, with their counterpart for phantom (a) computed using ICS diffusivity of $0.83\,\mu m^2/ms$, shown in Table 4.6.

4.8 Discussion and Conclusion

This chapter aims to develop a workflow to generate a novel numerical phantom representing myocardial microstructure. Compared with previous efforts, this study introduces two main novel contributions: (a) it considers more realistic shapes for the CMs and consequently a realistic complexity for the medium (relative to previous phantoms), by incorporating the native PDFs of CM shape parameters into the phantom; (b) it models the ICDs within the phantom and takes into account their effects on the dMRI signal.

Interestingly, the comparison of the *in-silico* images with the histological images in Figure 4.15 shows that the proposed method closely mimics myocardial tissue. The most striking observation emerges from the shape comparison of several single *in-silico* CMs with real CMs, shown in Figure 4.15(a), where the proposed algorithm is demonstrated to generate a realistic *in-silico* version of CMs. Figure 4.15(b) and Figure 4.15(c) show an apparent similarity between the shape of the transverse and longitudinal cross-section of *in-silico* tissue and real ones, where combining both confirms an elliptical shape for CMs. However, closer inspection in Figure 4.15(b) reveals different dispersion for crosswise orientation of the CMs (the directions of the principal axes of polygons) in *in-silico* images and histology. In the *in-silico* images, these directions are more correlated than those of the histological images.

The virtual morphometric study (Table 4.2) confirms that the shape of individual CMs is consistent with real CMs, where p-values for the length and volume of the CMs, i.e., p_3, and p-values for major and minor axes of the CMs, i.e., p_2, are > 0.01. The

Table 4.6: Effect of adding obstacles into ECS (Figure 16) on reduction of λ_2 with ICS diffusivity of $0.83\,\mu m^2/ms$.

Eigenvalues ($\mu m^2/ms$)	Figure 4.26(a)	Figure 4.26(b)	Figure 4.26(c)	Figure 4.26(d)	Figure 4.26(e)
λ_1	1.63	1.56 (↓4%)	1.47 (↓10%)	1.51 (↓7%)	1.35 (↓17%)
λ_2	1.34	1.20 (↓11%)	1.06 (↓21%)	1.10 (↓18%)	0.86 (↓35%)
λ_3	1.01	0.97 (↓4%)	0.90 (↓10%)	0.94 (↓7%)	0.83 (↓18%)

Table 4.7: Effect of adding obstacles into ECS (Figure 4.26) on eigenvalues with ICS diffusivity of 1 $\mu m^2/ms$.

Eigenvalues ($\mu m^2/ms$)	Figure 4.26(a)	Figure 4.26(b)	Figure 4.26(c)	Figure 4.26(d)	Figure 4.26(e)
λ_1	1.81	1.73	1.63	1.69	1.52
λ_2	1.48	1.30	1.16	1.20	0.94
λ_3	1.08	1.04	0.97	1.01	0.91

reason for high p-values for the length and volume lies in the step shown in Figures 4.12c and 4.12l-4.12o, where the shape of each virtual CMs is modified to preserve the input PDF of the length and volume, respectively. In contrast, the statistical tests related to PDFs of the major-axis and minor-axis result in lower values of p_2. As shown in Figure 4.16, major-axis and minor-axis PDFs of the output are broadened than the input. Broadening is a consequence of creating inter-CM space, during the transformation of the ellipse packing to the polygons. To create inter-CM space, the area of some polygons, shown in Figure 4.12.b, is shrunk, which leads to the reduction of the values of the major- and minor- axes and correspondingly, a broadening of their PDFs.

Considering microstructure complexity, the results of the structural correlator $\Gamma(k)$ corroborate the consistency between the *in-silico* generated tissue and real tissue (Figure 4.17). [Novikov et al., 2014] showed that the transverse cross-sections of skeletal muscle are classified as an extended disorder due to $\Gamma(k) \sim k^{-1}$. This k^{-1} behaviour comes from (relatively) straight lines of the myocyte's boundaries in the transverse cross-section of skeletal muscle, which spatially correlates over length scales of the cell's diameter. As shown in Figure 4.15(b), CMs' boundaries in the transverse cross-section of the myocardial tissue are curved, and their directions are uncorrelated. Therefore, the k^{-1} gets cut-off at $k \sim \frac{1}{\text{Cell's diameter}}$, and the disorder at larger cell diameter scales tends to plateau, i.e., k^0, the green dashed line in Figure 4.17, termed a short-ranged disorder.

This study shows that the median $\pm$ MAD of the angular distance between the input and simulated eigenvectors, along with the absolute angle difference between the input and simulated sheetlet angles, displayed in Figure 4.20 and 4.21, are lower than those between DTI and STI, reported in Figure 10 and Figure DS3 of [Bernus et al., 2015]. Moreover, the angular distance between the input and simulated V_3 (Figure 4.20(c)) is much smaller than the angular distance between the directly measured FLASH laminar normal and V_3 of STI and DTI, as reported in [Bernus et al., 2015]. Additionally, the resulting absolute angle difference for HA (Figure 4.21) demonstrates that the deviation of the simulated HA from the input directions ($4.3° \pm 3.1°$) is consistent with the absolute angle difference for HA between the experimental cDTI and histology reported by [Holmes et al., 2000] ($3.7° \pm 6.4°$) and [Scollan et al., 1998] ($4.9° \pm 14.6°$). According to Figure 4.23, λ_1 and λ_3 are in reasonable agreement with those from the *ex-vivo* data.

However, λ_2 of *in-silico* is considerably higher than its *ex-vivo* counterpart. Since the ICS and ECS diffusivities contribute fairly well to the values of λ_1 and λ_3, the best way to reduce λ_2 with less effect on λ_1 and λ_3 is to add more obstacles to the passage of water molecules in the direction of V_2. The most important compartments that hinder the movement of water molecules in this direction are microvasculature, fibroblast, and collagens (non-CM compartment) (with the VF of 7.7%, 2.5% [Greiner et al., 2018], and 2% [Haddad and Samani, 2017], respectively), as they are perpendicular to V_2, aligned along CMs [Greiner et al., 2018]. Moreover, inter-sheetlet space in real myocardial tissue is more tortuous than its *in-silico* counterpart, which results in λ_2 reduction. Section 4.7.7 illustrates the effect of adding the above-mentioned obstacles in ECS on eigenvalues over simple phantoms. For these phantoms, adding the obstacles in ECS reduces all eigenvalues λ_1 and λ_3 reduce by the same amount, whereas the reduction in λ_2 is two times more than both λ_1 and λ_3. Thus, the results in Section 4.7.7 appear to support the argument that dismissing obstacles in ECS increases λ_2. In addition, although there is no statistical difference between the *in-silico* and *ex-vivo* values of λ_1 and λ_3, there are differences between the range of their quartiles and extremes as shown in the box plots of Figure 4.23. The possible explanation for these differences is that the reported values for CM shape parameters are an average from a large part of a heart, whereas these values are used for every small *in-silico* voxel.

Therefore, the focus of future works should be on integrating realistic microvasculature, non-CM compartments, along with tortuous inter-sheetlet space into the numerical phantom to improve the agreement between *in-silico* and *ex-vivo* λ_2. Moreover, local information about the CM shape parameters for every voxel should be used in the experiment to make the findings more generalisable. Therefore, there is a definite need for an imaging method for intact hearts that enables us to reveal this information.

Chapter 5 : An in-silico imaging framework for intravoxel incoherent motion MRI

5.1 Chapter summary

This chapter introduces an in silico IVIM MRI framework developed through an extended finite element solver.

Contrary to previous approaches, this framework accounts for volumetric microvasculature during blood flow simulations, incorporates diffusion phenomena in the intravascular space, and accounts for the permeability between the intravascular and extravascular spaces. Some experiments are presented to explore how these features of the proposed framework affect a simulated dMRI signal.

5.2 Introduction

Perfusion plays a crucial role in preserving the normal function of the tissues by delivering O_2 and nutrients into tissue as well as discharging CO_2 and wastes. Hence, perfusion imaging is instrumental in the diagnosis and monitoring of microvasculature diseases such as ischemia, hypercapnia- and hyperoxygenation-induced vasoconstriction Federau et al. [2012], distinguishing between high- and low-grade brain gliomas Federau et al. [2014a], and etc.

As discussed in Section 1.2.2, IVIM MRI is a promising technique that allows perfusion assessment of the tissue. However, the interpretation of IVIM imaging data can be challenging due to the complexity of the underlying physiological processes. The use of virtual imaging frameworks can help to overcome these challenges by providing a framework for the interpretation of IVIM MRI data and the estimation of quantitative parameters Spinner et al. [2019], Zhang et al. [2018].

For instance, virtual IVIM MRI frameworks can provide a detailed understanding of the underlying physiological processes that contribute to IVIM MRI. They can simulate the different complex microcirculation dynamics within tissues and help to identify the contributions of different parameters to the signal. This can help to disentangle the

effects of diffusion and perfusion and provide a more accurate estimation of tissue microstructure and perfusion. Furthermore, virtual IVIM MRI frameworks can help to optimize the acquisition parameters for IVIM MRI. By simulating the effects of different diffusion weighting gradients and echo times, virtual IVIM MRI frameworks can identify the optimal acquisition parameters for a given tissue type and imaging protocol. This can help to improve the accuracy and reproducibility of IVIM MRI data.

5.3 Literature review

To date, all the numerical studies of IVIM MRI have been done using a simple numerical method, namely, an elementary method that simulates the movement of spins based on only the blood flow velocity over vascular trajectories $R(t')$. Then, the acquired phase ϕ_t due to these displacements of spins is computed as $\phi_t = \int_0^t \gamma G(R(t'), t')dt'$, and finally, the approximate IVIM MRI signal is computed using $S = S_0\mathbb{E}\{e^{(i\phi_t)}\}$, where $\mathbb{E}\{\}$ is an expectation of random variable of ϕ_t. For a basic example, see Fournet et al. [2017]. Additionally, Mozumder et al. [2018] used the discussed method to analyse the sensitivity of different IVIM MRI parameter estimation algorithms to the parameter initialisation values, and Spinner et al. [2019] used the same method to compare the IVIM MRI encoding efficiency of spin-echo- and stimulated-echo-based diffusion MRI for assessing myocardial perfusion. More recently, using this method, simulated IVIM MRI in three realistic vascular networks of a mouse brain was conducted inVan et al. [2021]. A likely explanation for the limited body of research on the numerical study of IVIM MRI, compared with diffusion MRI techniques Fieremans and Lee [2018], is the lack of a sophisticated virtual imaging technique for IVIM MRI simulation. The major drawback of the above elementary approach is the use of vessel trajectory instead of the 3D geometry of microvasculature, which imposes three limitations:

i The blood flow simulation is unrealistic, regardless of the flow computation method, as the elementary method assigns a unique blood velocity to each vessel segment. However, blood velocity along both parallel and vertical axes of the vessel axis is variable.

ii The diffusion within the intravascular space due to the Brownian motion of water molecules inside the red blood cells and plasma is ignored.

iii The effect of the permeability between the intra- and extra-vascular spaces is not accounted for.

iv The hindering effect of vascular geometry on the spins within the extravascular space is discarded.

5.4 Motivation and Contribution

The objective of this chapter is to present a virtual IVIM MRI technique which addresses the abovementioned limitations. This technique integrates a sophisticated and established blood flow simulator with a newly developed MR transverse magnetisation simulator. The schematic diagram of this virtual IVIM MRI technique is shown in Figure 5.1. This technique includes two cores:

i *Blood flow simulator based on the Lattice Boltzmann Method (LBM)*: the pseudo-diffusion describes blood flow through the capillaries as a diffusion-like process, and relates it to blood flow velocity. Hence, having a more realistic and accurate IVIM MRI simulation requires a more realistic and accurate blood flow simulation. For this purpose, a computational fluid dynamics package, HemeLB Mazzeo and Coveney [2008], is used which can resolve the full three-dimensional flow field in any microvascular bed of interest Bernabeu et al. [2018] by approximating the Navier-Stokes equations with an efficient and highly parallel LBM implementation. A more detailed description of HemeLB is available in Bernabeu et al. [2014].

ii *MR magnetisation simulator based on the finite element method*: To simulate MR transverse magnetisation, a new extension of SpinDoctor, a Matlab Toolbox providing numerical solutions to the Bloch-Torrey partial differential equation (BTPDE) Li et al. [2019], is presented for IVIM MRI simulation, called SpinDoctor-IVIM. The SpinDoctor-IVIM solves a "generalised" form of BTPDE, termed gBTPDE, which takes into account the velocity of the water molecules' spins in the blood flow alongside their diffusion and relaxation.

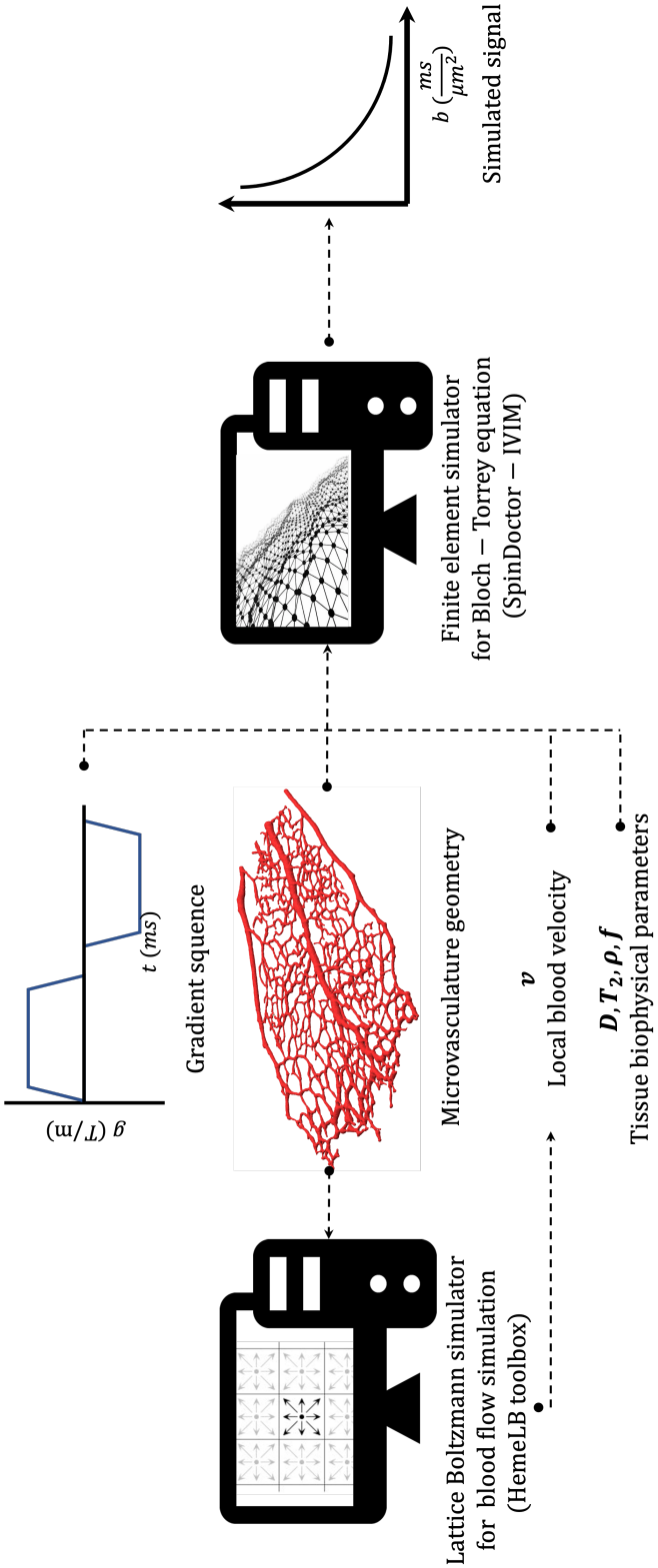

Figure 5.1: Schematic diagram of the proposed integrated framework for virtual IVIM MRI.

5.5 Data

A developmental retinal vascular plexus network, at the centre of Figure 5.1 in red, was acquired in an earlier study Bernabeu et al. [2014], using transmission electron microscopy. Details regarding tissue preparation, transmission electron microscopy imaging, image segmentation, and 3D surface generation are available in Franco et al. [2008] and Bernabeu et al. [2014], respectively. In this network, the largest diameter is 40 µm, which occurs along the retinal vein, whereas, the larger diameter of artery segments is about 16 µm approaching the optic disc. The capillary's diameters vary approximately in the range 2 to 10 µm, with a reduced amount of vessels with a smaller diameter.

5.6 Method

5.6.1 Finite Element Solution of Generalised Bloch-Torrey Partial Differential Equation

This Section presents the extensions made to the original version of SpinDoctor to form SpinDoctor-IVIM. The gBT equation Eq.(2.21) is spatially discretised using the finite element method (FEM), resulting in the following linear system:

$$\boldsymbol{M}_l \frac{\delta \eta_l}{\delta t} = -(\boldsymbol{S}_l + \sqrt{-1}\boldsymbol{Q}_l(t) + \frac{1}{T_l}\boldsymbol{M}_l + \boldsymbol{J}_l + \boldsymbol{F}_l(t))\eta_l, \tag{5.1}$$

where $\boldsymbol{M}_l$ is the mass matrix Eq.(2.34), $\boldsymbol{S}_l$ is the stiffness matrix Eq.(2.35), $\boldsymbol{Q}_l(t)$ is the scaled-mass matrix Eq.(2.36), $\boldsymbol{J}_l$ is the flux matrix Eq.(2.37), and $\boldsymbol{F}_l(t)$

$$\{\boldsymbol{F}_l\}_{ij} \triangleq F_{ij} = \int_{\Omega_l} \phi_j^l(\boldsymbol{r})\boldsymbol{v}(\boldsymbol{r},t)\cdot\nabla\phi_i^l(\boldsymbol{r})\,d\boldsymbol{r} \tag{5.2}$$

is the damping matrix. The finite elements used by SpinDoctor-IVIM are P1 elements, η_l is the approximation of the magnetisation at the nodes of the finite element in Ω_l, and $(\phi_i^l(\boldsymbol{r}))$ are the set of finite element basis functions in Ω_l.

SpinDoctor incorporates Eq. (2.34)-(2.37) to solve the Bloch-Torrey equation. The extension SpinDoctor-IVIM, incorporates the damping matrix, i.e., Eq. (2.38), into the linear system of Eq. (2.33), enabling one to consider the effect of blood flow on magnetisation. The linear system of Eq. (2.33) is solved using the*theta time stepping* method (generalised midpoint) Stuart and Peplow [1991], with the following parameter set-up of the toolbox:

- *implicitness* = 0.5: calls Crank Nicolson method Stuart and Peplow [1991];
- *timestep* = 5 µs: timestep for iterations.

5.6.2 Interpolating Local Velocities for Tetrahedron Mesh

HemeLB is used to compute the local velocities within the microvasculature, which is the input to SpinDoctor-IVIM. HemeLB computes these values for the vertices of a lattice, shown in Figure 5.2 as small circles, but these local values should be computed for each tetrahedron, as tetrahedral meshes are the inputs to SpinDoctor-IVIM. Figure 5.2 shows how tetrahedrons are generated in different sizes and occupy the computational space. Therefore, it is necessary to interpolate the local velocities for each tetrahedron centre before simulating the IVIM MRI signal using SpinDoctor-IVIM.

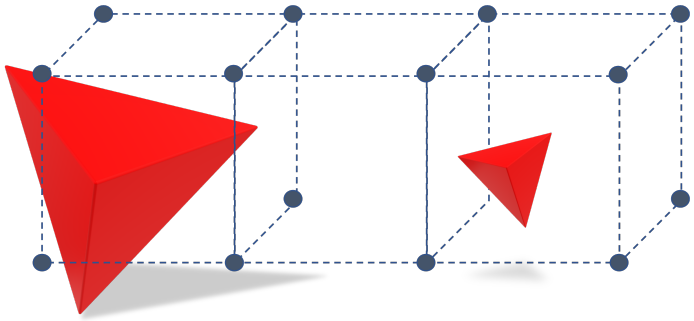

Figure 5.2: A schematic of the relative position of a lattice versus tetrahedron.

Before the interpolation, it is necessary to register the discretised domains of the lattice and the tetrahedral finite element mesh to achieve the most accurate interpolation of the velocities at the tetrahedral centres. This can be accomplished most efficiently by generating a tetrahedral volume mesh directly from the input surface mesh, as in Figure 5.3a. There are occasions, however, when the tetrahedral volume mesh does not register completely with the lattice domain due to some technical issues. Therefore, before interpolation, mesh registration must be investigated and corrected between the two domains, as in Figure 5.3.

For this purpose, first, a rigid transformation that registers the surface of the tetrahedral domain to the input mesh surface of HemeLB is computed Besl and McKay [1992], Chen and Medioni [1992]. Then, using this rigid transformation, all the vertices within the tetrahedral domain are moved into a new location. With the tetrahedral

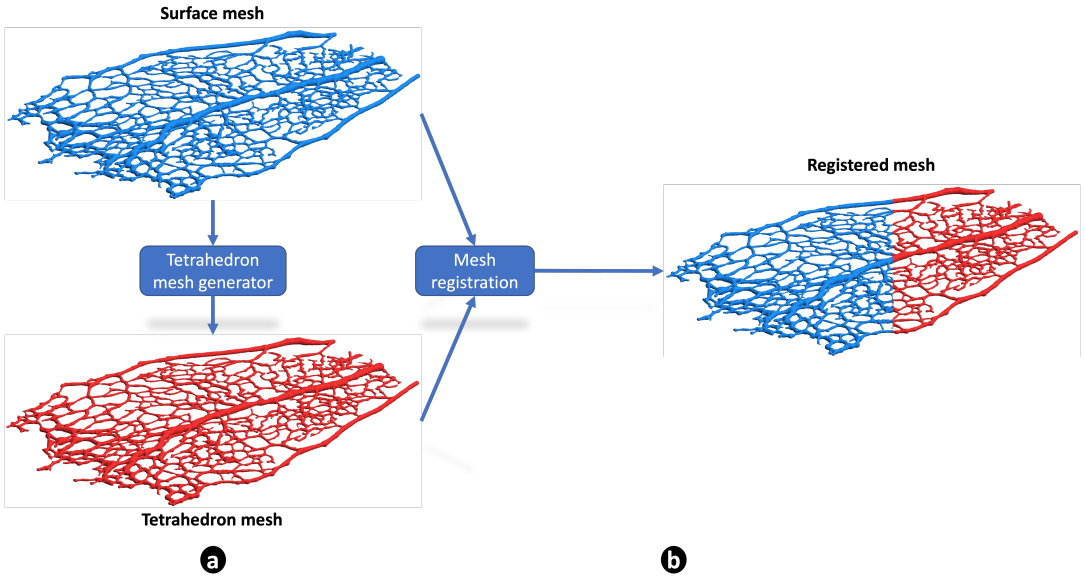

Figure 5.3: Mesh generation and registration. a) Generating tetrahedron mesh, to be used as SpinDoctor-IVIM input, from the input surface mesh of HemeLB; b) Registration between tetrahedron mesh and the output lattice of HemeLB.

domain registered to the lattice domain, velocities at the centre of the tetrahedrons are interpolated using scattered data interpolation methods Amidror [2002].

5.6.3 Adding extravascular domain

The effect of microvasculature permeability on IVIM MRI signal can be accounted for by enclosing microvasculature with extravascular spaces, as shown in Figure 5.4. The outline boundary of this extravascular space can, however, affect the simulated signal unrealistically. Unlike real tissue, which does not have these boundaries, molecules that reach this extravascular space in the simulation domains reflect elastically off. To discard the impact of the collisions between molecules and extravascular outline boundaries, IVIM MRI simulations are run over a mesh with a larger extravascular domain to eliminate the impact of collisions between molecules and extravascular outline boundaries. Finally, extravascular magnetizations in the vicinity of outline boundaries are excluded from the IVIM MRI signal calculation.

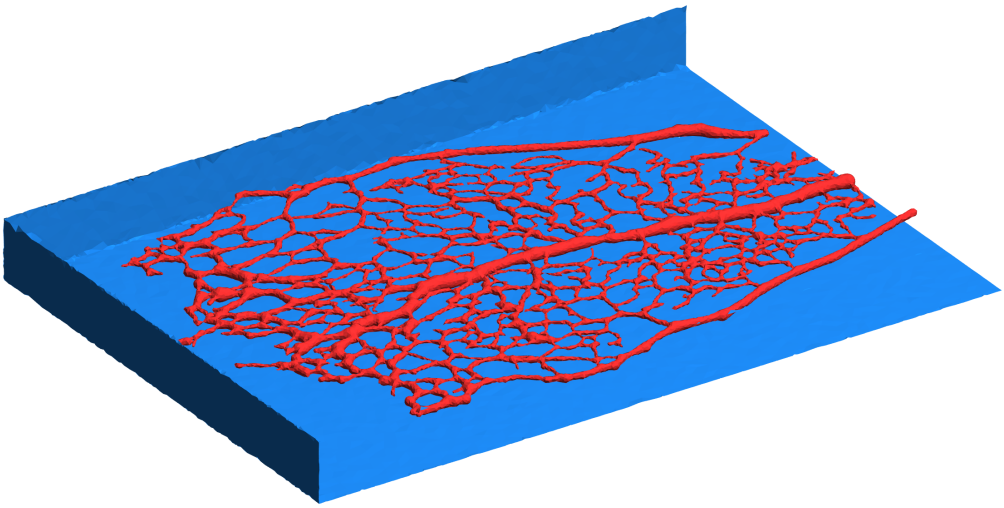

Figure 5.4: Sub-set of murine retinal vascular plexus (red) surrounded by extra-vascular space (blue).

5.6.4 Removing Effect of Outlet Boundaries on A Simulated IVIM MRI

During virtual IVIM MRI, when simulated spins reach outlet boundaries, they reflect elastically off those boundaries. These collisions, which affect the simulated signal, never happen in a real IVIM MRI experiment due to the continuity of the vascular system. Therefore, the simulation parameters must be set to prevent the spins from reaching the outlet boundaries before the echo time to avoid adverse effects from the outlet boundaries on the simulated IVIM MRI. For this purpose, the IVIM MRI simulation begins in a part of the vascular domain, termed region of interest (ROI), which is far enough from the outlet boundaries, while the region of non-interest (RONI), the region near the outlet boundaries, is initialised by zero magnetisation, as in Figure 5.5. Lastly, after the simulation is complete, the simulated IVIM MRI signal is computed without considering the magnetisation values in RONI. As in Figure 5.5, one reliable and easy way to define RONI for the domain is to consider the part at $\max\{\boldsymbol{v}(\boldsymbol{r},t)\}\times T_e$ around outlet boundaries as RONI, where T_e is the echo time. Examples of the simulated IVIM MRI signal for the different ROI have been shown in Figure 5.6 for the velocities ranging from 0 to the maximum possible velocity at each ROI.

For all experiments in this work, to compute the local blood flow velocities through the microvasculature, the result of the blood flow simulation reported in Bernabeu

et al. [2014], for ocular perfusion pressure of 25 mmHg is used. Bernabeu et al. [2014] showed the changes in ocular perfusion pressure affect only the magnitude of blood velocity within the microvasculature, not the pattern of flow. Therefore, to repeat the IVIM MRI simulation at the different blood velocities, the magnitude of the velocities simulated for ocular perfusion pressure of 25 mmHg is scaled.

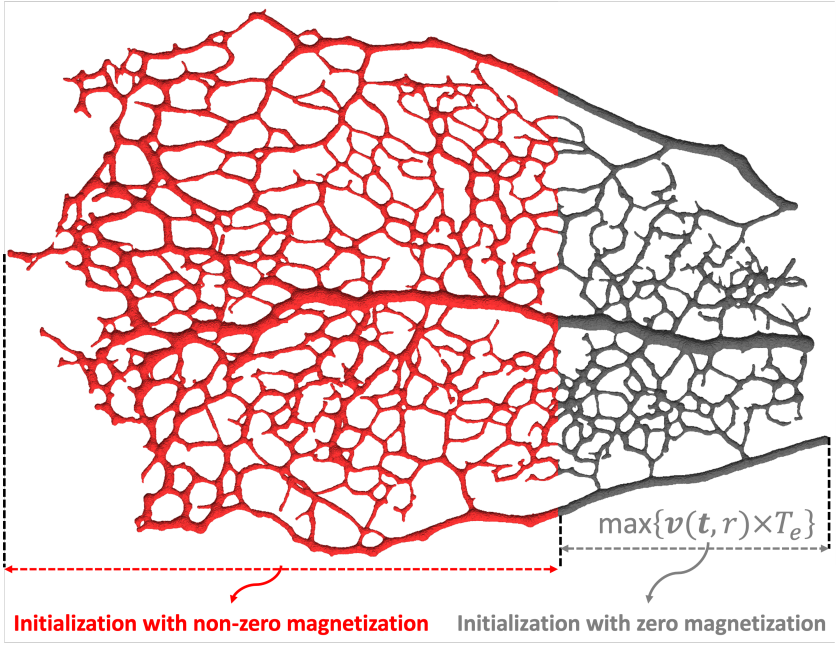

Figure 5.5: Excluding the effect of the outlet boundaries on the simulated IVIM MRI signal by setting zero initial magnetisation at $\max\{\boldsymbol{v}(\boldsymbol{r},t)\}\times T_e$ vicinity of outlet boundaries. At the end of the simulation, the magnetisation in this region is dismissed in the computation of the final signal.

5.7 Experiments and Results

This Section illustrates how the proposed framework can be applied to IVIM MRI studies through some prototypical experiments. As described earlier in Section 5.2, when blood flows incoherently in the microvasculature, diffusion gradients dephase spins in blood, according to the IVIM theory Le Bihan et al. [1986]. Le Bihan et al. Le Bihan et al. [1986] described the IVIM MRI signal through a bi-exponential model, which included a true diffusion component related to the Brownian motion of

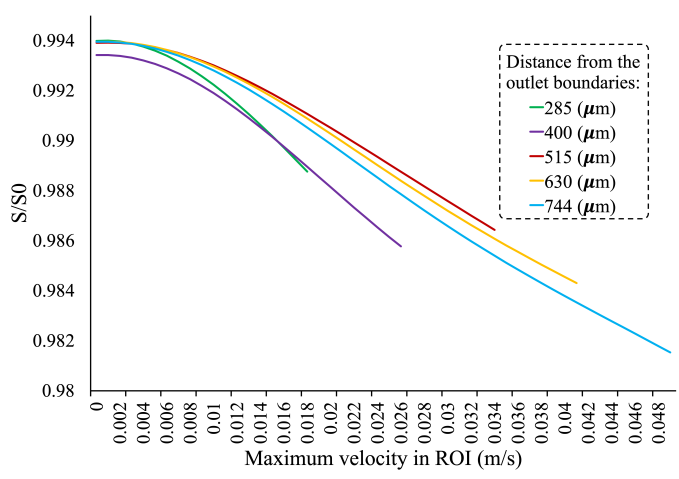

Figure 5.6: Effect of different ROIs, $\max\{\boldsymbol{v}(\boldsymbol{r},t)\} \times T_e$, and maximum velocities $\max\{\boldsymbol{v}(\boldsymbol{r},t)\}$ for each ROI on normalised IVIM MRI signal.

water molecules, D, and a perfusion-related diffusion component concerned with blood microcirculation in the capillary network, pseudo-diffusion coefficient D^*, according to the following formula:

$$\frac{S}{S_0} = (1-f) \times e^{-b \times D} + f \times e^{-b \times (D^*)} \tag{5.3}$$

where f is perfusion fraction.

These experiments include evaluating the effects of changes in biophysical parameters of the domain, such as blood pressure, vascular permeability, and intravascular diffusivities, on simulated IVIM MRI signals, as well as their effects on estimated biophysical parameters of microvascular using a bi-exponential signal model. The bi-exponential model is fitted to IVIM MRI signal using the segmented fitting method Jalnefjord et al. [2018].

5.7.1 Effect of Different Blood Pressure on IVIM MRI Signal

The link between high blood pressure and damage to the heart, brain, retina, kidneys, and arterial blood vessels has been well established in research Mensah [2016]. When blood pressure exceeds the normal level, structural changes occur in the targeted organs, resulting in organ dysfunction Suvila and Niiranen [2022]. The goal of this experiment is to investigate how changes in blood pressure affect IVIM MRI signals and

the parameters of the bi-exponential model. Since blood pressure and blood velocity are directly related, changing the velocity in gBT will account for changes in blood pressure. To provide the spins with enough opportunity to disperse, relatively large diffusion times and geometry should be considered. Therefore, since the experiments were restricted to a small retinal microvasculature, experiments limited the maximum velocity of $0.01\,\mathrm{ms}^{-1}$ and $0.02\,\mathrm{ms}^{-1}$.

5.7.2 Effect of Different Intravascular Diffusivities on IVIM MRI Signal

Previous simulation frameworks do not account for the effect of blood diffusion on simulated signals Spinner et al. [2019], Van et al. [2021] as discussed earlier. According to typical IVIM MRI experiments, the effect of blood self-diffusion on signal attenuation is trivial compared to blood velocity (modelled by pseudo-diffusion), but the results of the flow-compensated diffusion gradient experiment do not support this assertion Funck et al. [2018]. The objective of this experiment is to determine whether changes in intravascular diffusivity affect the simulated IVIM MRI signal and three estimated parameters of the IVIM bi-exponential model. For this purpose, three intravascular diffusivity values of $10^{-7}\mu\mathrm{m}^2/\mathrm{ms}$, $1.26\,\mu\mathrm{m}^2/\mathrm{ms}$ and $3\,\mu\mathrm{m}^2/\mathrm{ms}$ are used—The value of $1.26\,\mu\mathrm{m}^2/\mathrm{ms}$ is the experimental coefficient for blood diffusivity reported in Funck et al. [2018].

5.7.3 Effect of Different Vascular Permeabilities on IVIM MRI Signal

The permeability of the vascular system refers to the rate at which molecules and solutes exchange between the inside and outside of the vessel. Maintaining tissue functionality physiologically requires a normal exchange between blood components and tissues. Several vasculopathies modulate and alter this exchange rate, which adversely affects tissue function Wautier and Wautier [2022]. The following are examples: an increase in tumour microvascular permeability helps with cancer metastatic spread; acute increases in myocardial permeability cause tissue oedema, which affects the heart's pumping efficiency Claesson-Welsh [2015]; an increase in permeability increases interstitial pressure and impairs the delivery of therapeutic agents; an increase in retina microvasculature permeability is one of the first observable alterations in diabetic retinopathy, which can cause vision loss Antonetti et al. [1999]. This experiment aims to determine whether

changes in vascular permeability affect the IVIM MRI signal and if the IVIM biexponential signal model can detect these changes. This is done by simulating the IVIM MRI signal in the retina microvasculature using different orders of magnitude for the permeability: $10^{-7}\,\mathrm{m\,s^{-1}}$, $10^{-6}\,\mathrm{m\,s^{-1}}$ Allen et al. [2020], $10^{-5}\,\mathrm{m\,s^{-1}}$ Allen et al. [2021], and $10^{-4}\,\mathrm{m\,s^{-1}}$.

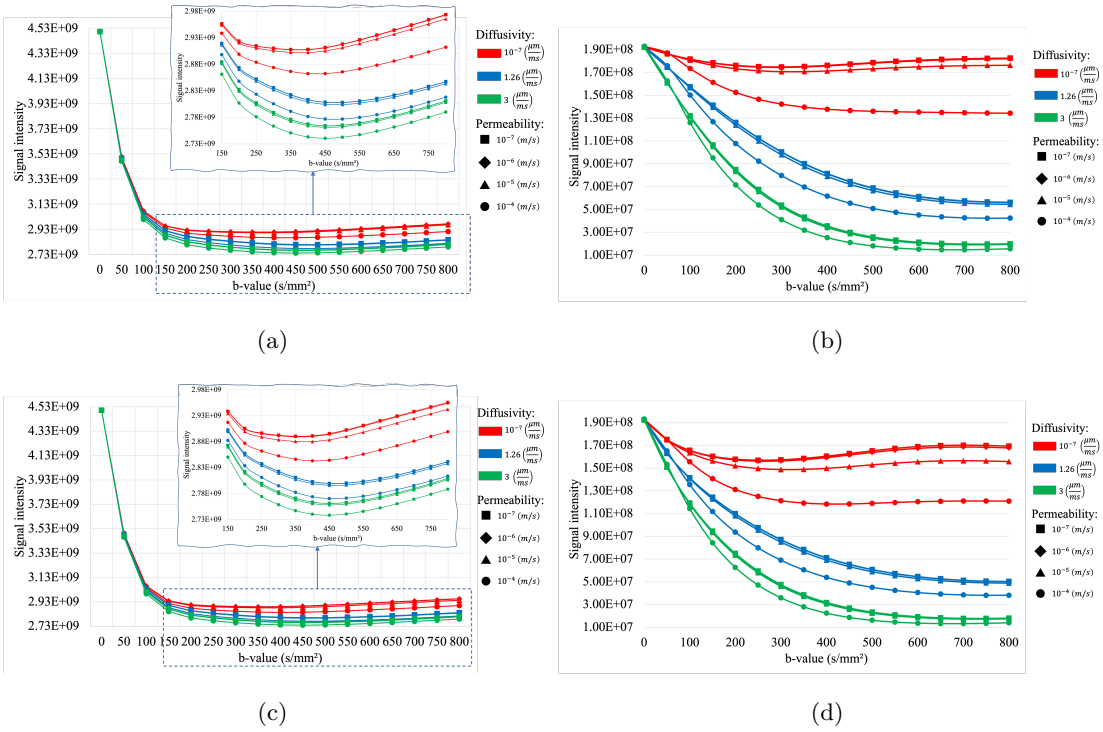

Figure 5.7: Effect of changing the blood diffusivity and vascular permeability on a) IVIM MRI signal originated from both intravascular and extravascular spaces at the velocity of $0.01\,\mathrm{m\,s^{-1}}$, b) IVIM MRI signal originated from intravascular spaces at the velocity of $0.01\,\mathrm{m\,s^{-1}}$, c) IVIM MRI signal originated from both intravascular and extravascular spaces at the velocity of $0.02\,\mathrm{m\,s^{-1}}$, and d) IVIM MRI signal originated from intravascular spaces at the velocity of $0.02\,\mathrm{m\,s^{-1}}$.

Following are the other imaging and biophysical parameters that will be fixed in the experiment:

- A classic Stejskal-Tanner pulse sequence is used for the IVIM MRI simulation, with b-values ranging from $0\,\mathrm{s/\mu m^2}$ to $800\,\mathrm{s/\mu m^2}$ with the incremental step of

$50\,\mathrm{s}/\mu\mathrm{m}^2$.

- The fixed diffusion time and gradient duration of 40 ms and 2.5 ms are used, while the gradient ramps are neglected.
- Intravascular and extravascular T_2 relaxations are fixed 220 ms (the average value of T_2 for arterial and venous blood) and 280 ms, respectively. These T_2 values were reported in Lin et al. [2012] and measured for samples under normal physiological conditions (haematocrit = 0.43), using a 1.5 T system, and at body temperature.
- The fixed value of $3\,\mu\mathrm{m}^2/\mathrm{ms}$ is used for diffusivity in extravascular space.

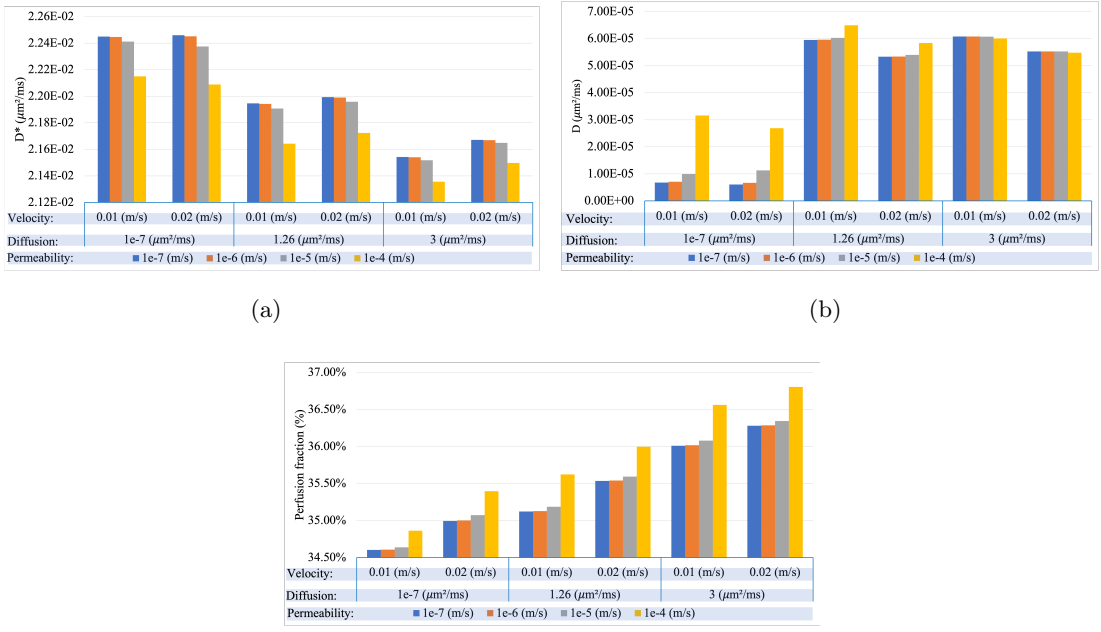

(a) (b)

(c)

Figure 5.8: Effect of changes in a) D^* b) D, and c) f at the different blood flow velocities, intravascular diffusivity and vascular permeability. The volume fraction of the microvasculature at experimental ROI is 9%.

Figures 5.7(a) and 5.7(c) show the IVIM MRI signal decay at the different b-values, originating from intravascular and extravascular spaces, for the different intravascular diffusivities and vascular permeabilities. At the same time, the maximum blood velocity

within the microvasculature is $0.01\,\mathrm{m\,s^{-1}}$ and $0.02\,\mathrm{m\,s^{-1}}$, respectively. Similarly, Figures 5.7(b) and 5.7(d) display the same information about the IVIM MRI signal decay originating only from intravascular space. A significant error is clear in Figures 5.7(b) and 5.7(d) when intravascular diffusivity is excluded from the simulated IVIM MRI signal. Further, an increase in both intravascular diffusivity and vascular permeability increase signal decay in Figure 5.7. Comparing Figure 5.7(a) with 5.7(c) and Figure 5.7(b) with 5.7(d), respectively, shows an increase in signal decay rate in IVIM MRI as blood flow velocity increases. Figures 5.8(a), 5.8(b), and 5.8(c) compare changes in the values of D^*, D, and f for the different values of vascular permeability, intravascular diffusivity, and blood flow velocity. 5.8(a) shows an increase in blood flow velocity leads to a rise in D^*, but an increase in diffusion and permeability values results in a decrease in D^* . As illustrated in 5.8(b), an increase in blood flow velocity leads to a reduction in D, but as expected, an increase in intravascular diffusivity leads to an increase in D. However, the effect of increasing vascular permeabilities depends on both intravascular and extravascular diffusivities. It can be seen in Figure 5.8(b) that there is a direct relationship between the estimated values of D and vascular permeability when intravascular diffusivities are less than $3\,\mu\mathrm{m}^2/\mathrm{ms}$. In contrast, this relationship reverses when intravascular and extravascular diffusivities are the same at $3\,\mu\mathrm{m}^2/\mathrm{ms}$. Finally, a higher velocity of blood flow, a higher intravascular diffusivity, and a higher vascular permeability result in higher values of f in Figure 5.8(c). The volume fraction of the microvasculature at experimental ROI is 9%.

Initial observations of the results in Figure 5.8 suggest that the changes in blood flow velocity and vascular permeability have a trivial impact on both IVIM MRI signal and the estimated parameters of bi-exponential IVIM. However, as the microvasculature used here for the simulation has a simple geometry and is small, caution must be applied; these findings might not be generalisable to more complex geometries. The T_2 values of blood are dependent on haematocrit content and oxygenation level Lin et al. [2012], which will affect the results for this study. It is also possible that the bi-exponential model cannot capture the effects of these biophysical changes in D^*, D, and f.

5.7.4 Computational Cost

The computations for Section 5.7 simulations were performed on ARC3, the High-Performance Computing facilities at the University of Leeds. ARC3 consists of 252 nodes with 24 cores (Broadwell E5-2650v4 CPUs, 2.2 GHz) and 128GB of memory each, and an SSD within the node with 100GB of storage. The details of computational cost for undertaken simulations in Section 5.7 is reported in Table 5.1.

5.8 Conclusion and Discussion

This study presents a virtual imaging framework, called SpinDoctor-IVIM, that simulates IVIM MRI signals by integrating a new finite element solver for gBT PDEs with a well-established LBM solver for the Navier-Stokes equations. SpinDoctor-IVIM provides a more realistic and comprehensive virtual imaging framework that can be used for prototyping IVIM MRI. One of the more significant findings to emerge from this study is that the intravascular diffusivity affects the simulated IVIM MRI signal in a non-trivial way, which is in accordance with previous research Funck et al. [2018].

Second, this study illustrates how vascular permeability affects the simulated IVIM MRI signal. In the previous method, IVIM MRI signals are simulated by simulating spin movement based solely on vascular trajectories, which makes it difficult to consider intravascular blood diffusivity and permeability between intravascular and extravascular spaces.

As well as these advantages of the proposed framework, the simulated signal is computed based on a more realistic blood flow simulation. This increases the result reliability and allows a local investigation of the relationship between blood flow parameters, such as the blood velocity and vessel's wall shear stress, with IVIM MRI parameters. Hence, the framework proposed here lays the groundwork for future research into the numerical study of IVIM MRI.

Table 5.1: Computational cost of the simulation

The number of nodes in the mesh	Memory per core (GB)	Number of cores for the pair of the experiment set-up (unique value of diffusivity, permeability, and velocity) over 17 b-values	Entire number of cores	Total computational time (core hours)
53844	4	3	3×24	20±1.83

Chapter 6 : Conclusions

6.1 Contributions

Throughout this chapter, the author summarises the contributions made by the work presented throughout this thesis for studying myocardial microstructure using virtual dMRI based on Brownian and intravoxel incoherent motions of water molecules in tissue. As part of this project, we have developed a new numerical phantom generator for the myocardium, as well as expanded the SpinDoctor toolbox for IVIM MRI. Furthermore, the author discusses the limitations and future directions of this field of research.

6.1.1 Three-dimensional micro-structurally informed in silico myocardium for virtual cardiac diffusion-weighted MRI

In silico tissue models (viz. numerical phantoms) provide a mechanism for evaluating quantitative models of magnetic resonance imaging. This includes the validation and sensitivity analysis of imaging and tissue microstructure parameters. Chapter 4 proposes a novel method to generate a realistic numerical phantom of myocardial microstructure. The proposed method extends previous studies by accounting for the variability of the cardiomyocyte shape, water exchange between the cardiomyocytes (ICDs), disorder class of myocardial microstructure, and four sheetlet orientations. In the first stage of the method, CMs and sheetlets are generated by considering the shape variability and ICDs in CM-CM connections. Sheetlets are then aggregated and oriented in the directions of interest. The morphometric study demonstrates no significant difference ($p > 0.01$) between the distribution of volume, length, and primary and secondary axes of the numerical and real (literature) CM data. Moreover, structural correlation analysis validates that the *in-silico* tissue is in the same class of disorderliness as the real tissue. Additionally, the absolute angle differences between the simulated HA and input HA (reference value) of the CMs ($4.3° \pm 3.1°$) demonstrate a good agreement with the absolute angle difference between the measured HA using experimental cDTI and histology (reference value) reported by (Holmes et al., 2000) ($3.7° \pm 6.4°$) and (Scollan et al., 1998) ($4.9° \pm 14.6°$). Furthermore, the angular distance between

eigenvectors and sheetlet angles of the input and simulated cDTI is much smaller than those between measured angles using structural tensor imaging (as a gold standard) and experimental cDTI. Combined with the qualitative results, these results confirm that the proposed method can generate richer numerical phantoms for the myocardium than previous studies.

6.1.2 An *in-silico* imaging framework for intravoxel incoherent motion MRI

IVIM MRI is increasingly recognised as an important tool in clinical MRI, where tissue perfusion and diffusion information can aid disease diagnosis, prognosis, treatment outcome assessment, and monitoring of patient recovery. Currently, biomarker discovery based on IVIM MRI, similar to other medical imaging modalities, depends on lengthy preclinical and clinical validation pathways to link image-derived observable markers with the underlying pathophysiological mechanisms. To speed up this process, a virtual IVIM MR imaging is proposed in Chapter 5. This approach requires an efficient virtual imaging framework to design, evaluate, and optimise novel approaches for IVIM MRI. In Chapter 5, in silico IVIM MRI is developed through a new FE solver, SpinDoctor-IVIM, which extends SpinDoctor, a dMRI simulation toolbox. SpinDoctor-IVIM simulates IVIM MRI signals by solving the generalised Bloch-Torrey PDE. The input velocity to SpinDoctor-IVIM is computed using HemeLB, an established Lattice Boltzmann blood flow simulator. Contrary to previous approaches, the SpinDoctor-IVIM accounts for volumetric microvasculature during blood flow simulations, incorporates diffusion phenomena in the intravascular space, and accounts for the permeability between the intravascular and extravascular spaces.

6.2 Limitations and Future directions

6.2.1 Three-dimensional micro-structurally informed in silico myocardium for virtual cardiac diffusion-weighted MRI

The most important limitation related to the numerical phantom is that non-CM compartments, along with tortuous inter-sheetlet space, are not included in the *in-silico* phantom. Moreover, the lack of local information about the CM shape parameters for every voxel makes these findings of Chapter 4 less generalisable. Thirdly, as shown in

Table 4.3, among 23 adjustable parameters of the numerical phantom, only eigenvectors of *in-silico* voxels are exactly matched with their *ex-vivo* counterparts. For the remaining 20 parameters, we either discarded these parameters (such as collagen's diffusivity and relaxation ($D_{collagen}$ and $T_{2_{collagen}}$), tissue twisting (α), wall curvature (p_r and p_l), etc.) or used the values reported in the literature (such as CMs' dimension (L, V, A and B), CMs' permeability ($k_{Sarco.}$ and k_{ICDs}), etc.) which are likely to differ from the parameters of the *ex-vivo* data under comparison. Therefore, there is a definite need for an imaging method for intact hearts that enables us to reveal this information. Imaging to this aim could be based on synchrotron radiation X-ray phase-contrast imaging, which has facilitated the investigation of myocardial tissue in detail, as recently shown by [Kaneko et al., 2017, Pierpaoli, 2010, Shinohara et al., 2016].

Sensitivity analysis of cDTI parameters or simulated diffusion signal to microstructure parameters listed in Table 4.3, along with incorporating non-CM compartments into the present phantom, will be the subject of future works. Moreover, the proposed micro-scale numerical phantom can be integrated into the XCAT phantom [Segars et al., 2010] to generate a micro-structurally informed numerical phantom of a whole cardiac organ. This opens up an opportunity for virtual imaging trials in cardiac dMRI through simulating 3D cardiac dMRI images —, which are micro-structurally informed—, together with including the effect of cardiac contraction and respiratory motion on dMRI images.

6.2.2 An *in-silico* imaging framework for intravoxel incoherent motion MRI

Another source of weakness in the results presented in Chapter 5, which could have affected the measurements of Figure 5.8, was the limitation of access to a complex and large microvasculature for a comprehensive sensitivity analysis of the IVIM MRI signal to changes in imaging parameters and biophysical parameters of the microvasculature. Due to the small size of the microvasculature, the range of possible values for blood flow velocity and diffusion encoding time was limited during the simulation set-up to preserve much of the microvasculature by minimising the $\max\{\boldsymbol{v}(\boldsymbol{r},t)\} \times T_e$, introduced in 5.6.4. Therefore, there is a need to address the problem of outlet boundaries, discussed in 5.6.4, more efficiently.

Furthermore, T_2 values of blood depend on haematocrit content and oxygenation

level. Hence, the different types of vessels, i.e., arterial and venous, have their specific range of T_2 values Lin et al. [2012]. Having more information about the type of vessels would allow for a more accurate IVIM MRI simulation by assigning correct T_2 relaxation values. Then, additional work is needed to label the different types of vessels in the microvasculature mesh, so the simulation can be set up with an appropriate distribution of T_2 relaxation.

References

Ehsan Abadi, William P Segars, Benjamin MW Tsui, Paul E Kinahan, Nick Bottenus, Alejandro F Frangi, Andrew Maidment, Joseph Lo, and Ehsan Samei. Virtual clinical trials in medical imaging: a review. *Journal of Medical Imaging*, 7(4):042805, 2020.

Ehsan Abadi, W Paul Segars, Hamid Chalian, and Ehsan Samei. Virtual imaging trials for coronavirus disease (covid-19). *AJR. American journal of roentgenology*, 216(2): 362, 2021.

Nor Aishah Ahad, Teh Sin Yin, Abdul Rahman Othman, and Che Rohani Yaacob. Sensitivity of normality tests to non-normal data. *Sains Malays.*, 40(6):637–641, 2011.

Claire L Allen, Naseeb K Malhi, Jacqueline L Whatmore, David O Bates, and Kenton P Arkill. Non-invasive measurement of retinal permeability in a diabetic rat model. *Microcirculation*, 27(6):e12623, 2020.

Claire L Allen, Katarzyna Wolanska, Naseeb K Malhi, Andrew V Benest, Mark E Wood, Winfried Amoaku, Roberta Torregrossa, Matthew Whiteman, David O Bates, and Jacqueline L Whatmore. Hydrogen sulfide is a novel protector of the retinal glycocalyx and endothelial permeability barrier. *Frontiers in Cell and Developmental Biology*, 9:724905, 2021.

Isaac Amidror. Scattered data interpolation methods for electronic imaging systems: a survey. *Journal of electronic imaging*, 11(2):157–176, 2002.

Steven S Andrews. Smoldyn: particle-based simulation with rule-based modeling, improved molecular interaction and a library interface. *Bioinformatics*, 33(5):710–717, 2017.

David A Antonetti, Erich Lieth, Alistair J Barber, and Thomas W Gardner. Molecular mechanisms of vascular permeability in diabetic retinopathy. In *Seminars in ophthalmology*, volume 14, pages 240–248. Taylor & Francis, 1999.

Piero Anversa, Marcello Rota, Konrad Urbanek, Toru Hosoda, Edmund H Sonnenblick, Annarosa Leri, Jan Kajstura, and Roberto Bolli. Myocardial aging: a stem cell problem. *Basic research in cardiology*, 100:482–493, 2005.

Leon Axel, Van J Wedeen, and Daniel B Ennis. Probing dynamic myocardial microstructure with cardiac magnetic resonance diffusion tensor imaging, 2014.

HE Abdel Baieth. Physical parameters of blood as a non-newtonian fluid. *International journal of biomedical science: IJBS*, 4(4):323, 2008.

Gregory T Balls and Lawrence R Frank. A simulation environment for diffusion weighted mr experiments in complex media. *Magnetic Resonance in Medicine: An Official Journal of the International Society for Magnetic Resonance in Medicine*, 62 (3):771–778, 2009.

Peter J Basser, James Mattiello, and Denis LeBihan. Mr diffusion tensor spectroscopy and imaging. *Biophysical journal*, 66(1):259–267, 1994.

B Bastide, T Jarry-Guichard, J.P. Briand, J DÃ©lÃ¨ze, and D Gros. Effect of anti-peptide antibodies directed against three domains of connexin43 on the gap junctional permeability of cultured heart cells. *J. of Membr. Biol.*, 150(3):243–253, 1996.

Joanne Bates. *A computational model to understand the relationship between cardiac microstructure and diffusion MRI*. PhD thesis, University of Oxford, 2016.

Joanne Bates, Irvin Teh, Darryl McClymont, Peter Kohl, Jürgen E Schneider, and Vicente Grau. Monte carlo simulations of diffusion weighted mri in myocardium: validation and sensitivity analysis. *IEEE transactions on medical imaging*, 36(6): 1316–1325, 2017.

JE Beare, L Curtis-Whitchurch, AJ LeBlanc, and JB Hoying. Microvasculature in health and disease. 2018.

Hildebrando G Benedicto, Pedro P Bombonato, Guido Macchiarelli, Giuseppe Stifano, and Isaura MM Prado. Structural arrangement of the cardiac collagen fibers of healthy and diabetic dogs. *Microsc. Res. and Tech.*, 74(11):1018–1023, 2011.

Jonathan Guy Bensley, Robert De Matteo, Richard Harding, and Mary Jane Black. Three-dimensional direct measurement of cardiomyocyte volume, nuclearity, and ploidy in thick histological sections. *Sci. Rep.*, 6:23756, 2016.

Miguel O Bernabeu, Martin L Jones, Jens H Nielsen, Timm Krüger, Rupert W Nash, Derek Groen, Sebastian Schmieschek, James Hetherington, Holger Gerhardt, Claudio A Franco, et al. Computer simulations reveal complex distribution of haemodynamic forces in a mouse retina model of angiogenesis. *Journal of The Royal Society Interface*, 11(99):20140543, 2014.

Miguel O Bernabeu, Martin L Jones, Rupert W Nash, Anna Pezzarossa, Peter V Coveney, Holger Gerhardt, and Claudio A Franco. Polnet: A tool to quantify network-level cell polarity and blood flow in vascular remodeling. *Biophysical journal*, 114(9): 2052–2058, 2018.

Olivier Bernus, Aleksandra Radjenovic, Mark L Trew, Ian J LeGrice, Gregory B Sands, Derek R Magee, Bruce H Smaill, and Stephen H Gilbert. Comparison of diffusion tensor imaging by cardiovascular magnetic resonance and gadolinium enhanced 3d image intensity approaches to investigation of structural anisotropy in explanted rat hearts. *J. Cardiovas. Magn. Reson.*, 17(1):1–27, 2015.

Paul J Besl and Neil D McKay. Method for registration of 3-d shapes. In *Sensor fusion IV: control paradigms and data structures*, volume 1611, pages 586–606. Spie, 1992.

Roberto Bolli, Hossein Ardehali, and Douglas W Losordo. *Manual of Research Techniques in Cardiovascular Medicine.* John Wiley & Sons, 2014.

Lindsay Brown. Cardiac extracellular matrix: a dynamic entity. *American Journal of Physiology-Heart and Circulatory Physiology*, 289(3):H973–H974, 2005.

Sok-Sithikun Bun, Frank Kober, Alexis Jacquier, Leon Espinosa, Jérôme Kalifa, Marie-France Bonzi, Francis Kopp, Nathalie Lalevee, Stephane Zaffran, Jean-Claude Deharo, et al. Value of in vivo t2 measurement for myocardial fibrosis assessment in diabetic mice at 11.75 t. *Investigative radiology*, 47(5):319–323, 2012.

Paul T Callaghan. A simple matrix formalism for spin echo analysis of restricted diffusion under generalized gradient waveforms. *Journal of Magnetic Resonance*, 129 (1):74–84, 1997.

Virginie Callot, Eric Bennett, Ulrich KM Decking, Robert S Balaban, and Han Wen. In vivo study of microcirculation in canine myocardium using the ivim method. *Magnetic Resonance in Medicine: An Official Journal of the International Society for Magnetic Resonance in Medicine*, 50(3):531–540, 2003.

W Carver, ML Nagpal, M Nachtigal, TK Borg, and L Terracio. Collagen expression in mechanically stimulated cardiac fibroblasts. *Circulation research*, 69(1):116–122, 1991.

Mara RN Celes, Diego Torres-Dueńas, Cibele M Prado, Erica C Campos, Jorge E Moreira, Fernando Q Cunha, and Marcos A Rossi. Increased sarcolemmal permeability as an early event in experimental septic cardiomyopathy: a potential role for oxidative damage to lipids and proteins. *Shock.*, 33(3):322–331, 2010.

Biyi Chen, Caimei Zhang, Ang Guo, and Long-Sheng Song. In situ single photon confocal imaging of cardiomyocyte t-tubule system from langendorff-perfused hearts. *Frontiers in physiology*, 6:134, 2015.

Yang Chen and Gérard Medioni. Object modelling by registration of multiple range images. *Image and vision computing*, 10(3):145–155, 1992.

Yue-Feng Chen, Suleman Said, Scott E Campbell, and A Martin Gerdes. A method to collect isolated myocytes and whole tissue from the same heart. *Am. J. Physiol.-Heart and Circ. Physiol.*, 293(3):H2004–H2006, 2007.

Lena Claesson-Welsh. Vascular permeabilityâ€"the essentials. *Upsala journal of medical sciences*, 120(3):135–143, 2015.

PA Cook, Y Bai, SKKS Nedjati-Gilani, KK Seunarine, MG Hall, GJ Parker, and D Cq Alexander. Camino: open-source diffusion-mri reconstruction and processing. In *14th scientific meeting of the international society for magnetic resonance in medicine*, volume 2759, page 2759. Seattle WA, USA, 2006.

Benedicte MA Delattre, Magalie Viallon, Hongjiang Wei, Yuemin M Zhu, Thorsten Feiweier, Vinay M Pai, Han Wen, and Pierre Croisille. In vivo cardiac diffusion-weighted

magnetic resonance imaging: quantification of normal perfusion and diffusion coefficients with intravoxel incoherent motion imaging. *Investigative radiology*, 47(11): 662–670, 2012.

Jelle Demeestere, Anke Wouters, Soren Christensen, Robin Lemmens, and Maarten G Lansberg. Review of perfusion imaging in acute ischemic stroke: from time to tissue. *Stroke*, 51(3):1017–1024, 2020.

Stefanie A Doppler, Catarina Carvalho, Harald Lahm, Marcus-André Deutsch, Martina Dreßen, Nazan Puluca, Rüdiger Lange, and Markus Krane. Cardiac fibroblasts: more than mechanical support. *Journal of thoracic disease*, 9(Suppl 1):S36, 2017.

Ivana Drobnjak, Hui Zhang, Matt G Hall, and Daniel C Alexander. The matrix formalism for generalised gradients with time-varying orientation in diffusion nmr. *Journal of Magnetic Resonance*, 210(1):151–157, 2011.

Albert Einstein. Über die von der molekularkinetischen theorie der wärme geforderte bewegung von in ruhenden flüssigkeiten suspendierten teilchen. *Annalen der physik*, 4, 1905.

Gary L Engelmann, John C Vitullo, and Ross G Gerrity. Morphometric analysis of cardiac hypertrophy during development, maturation, and senescence in spontaneously hypertensive rats. *Circulation research*, 60(4):487–494, 1987.

Emil K S Espe, Jan Magnus Aronsen, Morten Eriksen, Ole M Sejersted, Lili Zhang, and Ivar Sjaastad. Regional dysfunction after myocardial infarction in rats. *Circ. Cardiovasc. Imaging.*, 10(9):e005997, 2017.

Majid Ezzati, Ziad Obermeyer, Ioanna Tzoulaki, Bongani M Mayosi, Paul Elliott, and David A Leon. Contributions of risk factors and medical care to cardiovascular mortality trends. *Nature Reviews Cardiology*, 12(9):508, 2015.

Qianqian Fang and David A Boas. Tetrahedral mesh generation from volumetric binary and grayscale images. In *2009 IEEE international symposium on biomedical imaging: from nano to macro*, pages 1142–1145. Ieee, 2009.

Christian Federau. Intravoxel incoherent motion mri as a means to measure in vivo perfusion: A review of the evidence. *NMR in Biomedicine*, 30(11):e3780, 2017.

Christian Federau, Philippe Maeder, Kieran Oâ€™Brien, Patrick Browaeys, Reto Meuli, and Patric Hagmann. Quantitative measurement of brain perfusion with intravoxel incoherent motion mr imaging. *Radiology*, 265(3):874–881, 2012.

Christian Federau, R Meuli, K O'Brien, P Maeder, and P Hagmann. Perfusion measurement in brain gliomas with intravoxel incoherent motion mri. *American journal of neuroradiology*, 35(2):256–262, 2014a.

Christian Federau, Kieran O'Brien, Reto Meuli, Patric Hagmann, and Philippe Maeder. Measuring brain perfusion with intravoxel incoherent motion (ivim): initial clinical experience. *Journal of Magnetic Resonance Imaging*, 39(3):624–632, 2014b.

Vesselina Ferferieva, Nicholas Dâ€™Elia, Brecht Heyde, Petr Otahal, Frank Rademakers, and Jan Dâ€™hooge. Serial assessment of left ventricular morphology and function in a rodent model of ischemic cardiomyopathy. *The International Journal of Cardiovascular Imaging*, 34(3):385–397, 2018.

Els Fieremans and Hong-Hsi Lee. Physical and numerical phantoms for the validation of brain microstructural mri: A cookbook. *Neuroimage*, 182:39–61, 2018.

Gabrielle Fournet, Jing-Rebecca Li, Alex M Cerjanic, Bradley P Sutton, Luisa Ciobanu, and Denis Le Bihan. A two-pool model to describe the ivim cerebral perfusion. *Journal of Cerebral Blood Flow & Metabolism*, 37(8):2987–3000, 2017.

Claudio Areias Franco, Mathias Mericskay, Ara Parlakian, Guillaume Gary-Bobo, Jacqueline Gao-Li, Denise Paulin, Erika Gustafsson, and Zhenlin Li. Serum response factor is required for sprouting angiogenesis and vascular integrity. *Developmental cell*, 15(3):448–461, 2008.

A Fraticelli, R Josephson, R Danziger, Edward Lakatta, and H Spurgeon. Morphological and contractile characteristics of rat cardiac myocytes from maturation to senescence. *Am. J. Physiol. Heart Circu. Physiol.*, 257(1):H259–H265, 1989.

Carsten Funck, Frederik Bernd Laun, and Andreas Wetscherek. Characterization of the diffusion coefficient of blood. *Magnetic resonance in medicine*, 79(5):2752–2758, 2018.

A Martin Gerdes and Alessandro Pingitore. Assessment of cardiomyocyte size. *Manual of Research Techniques in Cardiovascular Medicine*, pages 378–385, 2014.

GA Gray, IS Toor, RFP Castellan, M Crisan, and M Meloni. Resident cells of the myocardium: more than spectators in cardiac injury, repair and regeneration. *Current opinion in physiology*, 1:46–51, 2018.

Denis S Grebenkov. Pulsed-gradient spin-echo monitoring of restricted diffusion in multilayered structures. *Journal of Magnetic Resonance*, 205(2):181–195, 2010.

Denis S Grebenkov. From the microstructure to diffusion nmr, and back. *Diffusion NMR of Confined*, pages 52–110, 2016.

Joachim Greiner, Aparna C Sankarankutty, Gunnar Seemann, Thomas Seidel, and Frank B Sachse. Confocal microscopy-based estimation of parameters for computational modeling of electrical conduction in the normal and infarcted heart. *Frontiers in physiology*, 9:239, 2018.

Giorgia Grisot. *Validation of dMRI techniques for mapping brain pathways*. PhD thesis, Massachusetts Institute of Technology, 2019.

RA Guyer and KR McCall. Lattice boltzmann description of magnetization in porous media. *Physical Review B*, 62(6):3674, 2000.

Seyyed MH Haddad and Abbas Samani. A novel micro-to-macro approach for cardiac tissue mechanics. *Comput. Methods Biomech. Biomed. Eng.*, 20(2):215–229, 2017.

Patrick W Hales, Jürgen E Schneider, Rebecca AB Burton, Benjamin J Wright, Christian Bollensdorff, and Peter Kohl. Histo-anatomical structure of the living isolated rat heart in two contraction states assessed by diffusion tensor mri. *Prog. Biophys. Mol. Biol.*, 110(2-3):319–330, 2012.

Kylian Haliot, Julie Magat, Valéry Ozenne, Emma Abell, Virginie Dubes, Laura Bear, Stephen H Gilbert, Mark L Trew, Michel Haissaguerre, and O. Quesson, Bernus. 3d high resolution imaging of human heart for visualization of the cardiac structure. In *Lect. Notes Comput. Sci.*, pages 196–207. Springer, 2019.

Matt G Hall and Daniel C Alexander. Convergence and parameter choice for monte-carlo simulations of diffusion mri. *IEEE transactions on medical imaging*, 28(9): 1354–1364, 2009.

A Alexander Holmes, D F Scollan, and Raimond L Winslow. Direct histological validation of diffusion tensor mri in formaldehyde-fixed myocardium. *Magn. Reson. Med.*, 44(1):157–161, 2000.

Mami Iima and Denis Le Bihan. Clinical intravoxel incoherent motion and diffusion mr imaging: past, present, and future. *Radiology*, 278(1):13–32, 2016.

Dmitrii N Ilin and Marc Bernacki. Advancing layer algorithm of dense ellipse packing for generating statistically equivalent polygonal structures. *Granul. Matter*, 18(3): 43, 2016.

Oscar Jalnefjord, Mats Andersson, Mikael Montelius, Göran Starck, Anna-Karin Elf, Viktor Johanson, Johanna Svensson, and Maria Ljungberg. Comparison of methods for estimation of the intravoxel incoherent motion (ivim) diffusion coefficient (d) and perfusion fraction (f). *Magnetic Resonance Materials in Physics, Biology and Medicine*, 31:715–723, 2018.

Neil Peter Jerome, Anna Caroli, and Alexandra Ljimani. Renal diffusion-weighted imaging (dwi) for apparent diffusion coefficient (adc), intravoxel incoherent motion (ivim), and diffusion tensor imaging (dti): basic concepts. In *Preclinical MRI of the Kidney*, pages 187–204. Humana, New York, NY, 2021.

Stephen E Jones, Bradley R Buchbinder, and Itzhak Aharon. Three-dimensional mapping of cortical thickness using laplace's equation. *Hum. Brain Mapp.*, 11(1):12–32, 2000.

Yukihiro Kaneko, Gen Shinohara, Masato Hoshino, Hiroyuki Morishita, Kiyozo Morita, Yoshihiro Oshima, Masashi Takahashi, Naoto Yagi, Yutaka Okita, and Takuro Tsukube. Intact imaging of human heart structure using x-ray phase-contrast tomography. *Pediatr. Cardiol.*, 38(2):390–393, 2017.

Dimitrios C Karampinos, Kevin F King, Bradley P Sutton, and John G Georgiadis. Intravoxel partially coherent motion technique: characterization of the anisotropy of skeletal muscle microvasculature. *Journal of Magnetic Resonance Imaging: An Official Journal of the International Society for Magnetic Resonance in Medicine*, 31 (4):942–953, 2010.

Zohya Khalique, Pedro F Ferreira, Andrew D Scott, Sonia Nielles-Vallespin, Ana Martinez-Naharro, Marianna Fontana, Phillip Hawkins, David N Firmin, and Dudley J Pennell. Diffusion tensor cardiovascular magnetic resonance in cardiac amyloidosis. *Circulation: Cardiovascular Imaging*, 13(5):e009901, 2020.

Mojtaba Lashgari, Nishant Ravikumar, Irvin Teh, Jing-Rebecca Li, David L Buckley, Jurgen E Schneider, and Alejandro F Frangi. Three-dimensional micro-structurally informed in silico myocardiumâ€"towards virtual imaging trials in cardiac diffusion weighted mri. *Medical Image Analysis*, 82:102592, 2022.

Bhagwandas Pannalal Lathi. *Modern digital and analog communication systems*. Oxford university press, 1998.

Denis Le Bihan. What can we see with ivim mri? *Neuroimage*, 187:56–67, 2019.

Denis Le Bihan and E Breton. Imagerie de diffusion in-vivo par résonance magnétique nucléaire. *Comptes-Rendus de l'Académie des Sciences*, 93(5):27–34, 1985.

Denis Le Bihan, Eric Breton, Denis Lallemand, Philippe Grenier, Emmanuel Cabanis, and Maurice Laval-Jeantet. Mr imaging of intravoxel incoherent motions: application to diffusion and perfusion in neurologic disorders. *Radiology*, 161(2):401–407, 1986.

Hong-Hsi Lee. *Revealing brain microstructure with time-dependent diffusion MRI*. PhD thesis, New York University, 2019.

Ian LeGrice, Adéle Pope, and Bruce Smaill. The architecture of the heart: myocyte organization and the cardiac extracellular matrix. In *Interstitial Fibrosis in Heart Failure*, pages 3–21. Springer, 2005.

Ian J LeGrice, Adèle J Pope, Gregory B Sands, Gillian Whalley, Robert N Doughty, and Bruce H Smaill. Progression of myocardial remodeling and mechanical dysfunction in the spontaneously hypertensive rat. *American Journal of Physiology-Heart and Circulatory Physiology*, 303(11):H1353–H1365, 2012.

Hao Lei, Yi Zhang, Xiao-Hong Zhu, and Wei Chen. Changes in the proton t2 relaxation times of cerebral water and metabolites during forebrain ischemia in rat at 9.4 t. *Magnetic Resonance in Medicine: An Official Journal of the International Society for Magnetic Resonance in Medicine*, 49(6):979–984, 2003.

Jing-Rebecca Li, Van-Dang Nguyen, Try Nguyen Tran, Jan Valdman, Cong-Bang Trang, Khieu Van Nguyen, Duc Thach Son Vu, Hoang An Tran, Hoang Trong An Tran, and Thi Minh Phuong Nguyen. Spindoctor: A matlab toolbox for diffusion mri simulation. *NeuroImage*, 202:116120, 2019.

Ai-Ling Lin, Qin Qin, Xia Zhao, and Timothy Q Duong. Blood longitudinal (t 1) and transverse (t 2) relaxation time constants at 11.7 tesla. *Magnetic Resonance Materials in Physics, Biology and Medicine*, 25:245–249, 2012.

Rajaprasad Loganathan, Mehmet Bilgen, Baraa Al-Hafez, and Irina V Smirnova. Characterization of alterations in diabetic myocardial tissue using high resolution mri. *The international journal of cardiovascular imaging*, 22(1):81–90, 2006.

Julie Magat, Valéry Ozenne, Nicolas Cedilnik, Jérôme Naulin, Kylian Haliot, Maxime Sermesant, Stephen H Gilbert, Mark Trew, Michel Haissaguerre, and O. Quesson, Bernus. 3d mri of explanted sheep hearts with submillimeter isotropic spatial resolution: comparison between diffusion tensor and structure tensor imaging. *Magn. Reson. Mater. Phys. Biol. Med.*, pages 1–15, 2021.

Marco D Mazzeo and Peter V Coveney. Hemelb: A high performance parallel lattice-boltzmann code for large scale fluid flow in complex geometries. *Computer Physics Communications*, 178(12):894–914, 2008.

Laura-Ann McGill, Pedro Ferreira, Andrew D Scott, Sonia Nielles-Vallespin, Ranil Silva, Philip J Kilner, David Firmin, and Dudley J Pennell. Comparison of cardiac dti parameters between systole and diastole. *Journal of Cardiovascular Magnetic Resonance*, 16(1):1–2, 2014.

Choukri Mekkaoui, Timothy G Reese, Marcel P Jackowski, Himanshu Bhat, and David E Sosnovik. Diffusion mri in the heart. *NMR in Biomedicine*, 30(3):e3426, 2017.

George A Mensah. Hypertension and target organ damage: donâ€™t believe everything you think! *Ethnicity & Disease*, 26(3):275, 2016.

Nathan Mewton, Chia Ying Liu, Pierre Croisille, David Bluemke, and João AC Lima. Assessment of myocardial fibrosis with cardiovascular magnetic resonance. *Journal of the American College of Cardiology*, 57(8):891–903, 2011.

Anna Mou, Chen Zhang, Mengying Li, Fengqiang Jin, Qingwei Song, Ailian Liu, and Zhiyong Li. Evaluation of myocardial microcirculation using intravoxel incoherent motion imaging. *Journal of Magnetic Resonance Imaging*, 46(6):1818–1828, 2017.

Kevin Moulin, Pierre Croisille, Thorsten Feiweier, Benedicte MA Delattre, Hongjiang Wei, Benjamin Robert, Olivier Beuf, and Magalie Viallon. In vivo free-breathing dti and ivim of the whole human heart using a real-time slice-followed se-epi navigator-based sequence: A reproducibility study in healthy volunteers. *Magnetic resonance in medicine*, 76(1):70–82, 2016.

Meghdoot Mozumder, Leandro Beltrachini, Quinten Collier, Jose M Pozo, and Alejandro F Frangi. Simultaneous magnetic resonance diffusion and pseudo-diffusion tensor imaging. *Magnetic resonance in medicine*, 79(4):2367–2378, 2018.

M Nahrendorf. Myeloid cells in cardiovascular organs. *Journal of internal medicine*, 285(5):491–502, 2019.

Noel Naughton and John Georgiadis. Connecting diffusion mri to skeletal muscle microstructure: Leveraging meta-models and gpu-acceleration. In *Proceedings of the Practice and Experience in Advanced Research Computing on Rise of the Machines (learning)*, pages 1–7. 2019.

Noel M Naughton, Caroline G Tennyson, and John G Georgiadis. Lattice boltzmann method for simulation of diffusion magnetic resonance imaging physics in multiphase tissue models. *Physical Review E*, 102(4):043305, 2020.

Barun K Nayak and Avijit Hazra. How to choose the right statistical test? *Indian J. Ophthalmol.*, 59(2):85, 2011.

Sonia Nielles-Vallespin, Zohya Khalique, Pedro F Ferreira, Ranil de Silva, Andrew D Scott, Philip Kilner, Laura-Ann McGill, Archontis Giannakidis, Peter D Gatehouse, Daniel Ennis, et al. Assessment of myocardial microstructural dynamics by *in vivo* diffusion tensor cardiac magnetic resonance. *J. Am. Coll. Cardiol.*, 69(6):661–676, 2017.

Sonia Nielles-Vallespin, Andrew Scott, Pedro Ferreira, Zohya Khalique, Dudley Pennell, and David Firmin. Cardiac diffusion: Technique and practical applications. *Journal of Magnetic Resonance Imaging*, 2019.

Maartje Noorman, Marcel AG van der Heyden, Toon AB van Veen, Moniek GPJ Cox, Richard NW Hauer, Jacques MT de Bakker, and Harold VM van Rijen. Cardiac cell–cell junctions in health and disease: electrical versus mechanical coupling. *J. Mol. Cell. Cardiol.*, 47(1):23–31, 2009.

Dmitry S Novikov, Jens H Jensen, Joseph A Helpern, and Els Fieremans. Revealing mesoscopic structural universality with diffusion. *Proc. Natl. Acad. Sci. U. S. A.*, 111(14):5088–5093, 2014.

Dmitry S Novikov, Els Fieremans, Sune N Jespersen, and Valerij G Kiselev. Quantifying brain microstructure with diffusion mri: Theory and parameter estimation. *NMR Biomed.*, page e3998, 2016.

João dos Santos Periquito, Katharina Paul, Till Huelnhagen, Min-Chi Ku, Yiyi Ji, Kathleen Cantow, Thomas Gladytz, Dirk Grosenick, Bert Flemming, Erdmann Seeliger, et al. Diffusion-weighted renal mri at 9.4 tesla using rare to improve anatomical integrity. *Scientific reports*, 9(1):1–12, 2019.

Jean-Claude Perriard, Alain Hirschy, and Elisabeth Ehler. Dilated cardiomyopathy: a disease of the intercalated disc? *Trends Cardiovasc. Med.*, 13(1):30–38, 2003.

Carlo Pierpaoli. Quantitative brain mri, 2010.

Christian Pinali, Hayley J Bennett, J Bernard Davenport, Jessica L Caldwell, Tobias Starborg, Andrew W Trafford, and Ashraf Kitmitto. Three-dimensional structure of the intercalated disc reveals plicate domain and gap junction remodeling in heart failure. *Biophys. J.*, 108(3):498–507, 2015.

Alexander R Pinto, Alexei Ilinykh, Malina J Ivey, Jill T Kuwabara, Michelle L Dâ€™antoni, Ryan Debuque, Anjana Chandran, Lina Wang, Komal Arora, and M.D. Rosenthal, Tallquist. Revisiting cardiac cellular composition. *Circ. Res.*, 118 (3):400–409, 2016.

Adèle J Pope, Gregory B Sands, Bruce H Smaill, and Ian J LeGrice. Three-dimensional transmural organization of perimysial collagen in the heart. *Am. J. Physiol. Heart Circ. Physiol.*, 295(3):H1243–H1252, 2008.

Eva A Rog-Zielinska, Callum M Johnston, Eileen T Oâ€™Toole, Mary Morphew, Andreas Hoenger, and Peter Kohl. Electron tomography of rabbit cardiomyocyte

three-dimensional ultrastructure. *Progress in biophysics and molecular biology*, 121 (2):77–84, 2016.

Jan N Rose, Sonia Nielles-Vallespin, Pedro F Ferreira, David N Firmin, Andrew D Scott, and Denis J Doorly. Novel insights into in-vivo diffusion tensor cardiovascular magnetic resonance using computational modeling and a histology-based virtual microstructure. *Magnetic Resonance in Medicine*, 81(4):2759–2773, 2019.

Thomas J Sauer, Ehsan Abadi, Paul Segars, and Ehsan Samei. Anatomically and physiologically informed computational model of hepatic contrast perfusion for virtual imaging trials. *Medical Physics*, 49(5):2938–2951, 2022.

Jutta Schaper, Eckhardt Meiser, and Gerhard StÃ¤mmler. Ultrastructural morphometric analysis of myocardium from dogs, rats, hamsters, mice, and from human hearts. *Circ. Res.*, 56(3):377–391, 1985.

David F Scollan, Alex Holmes, Raimond Winslow, and John Forder. Histological validation of myocardial microstructure obtained from diffusion tensor magnetic resonance imaging. *Am. J. Physiol. Heart Circ. Physiol.*, 275(6):H2308–H2318, 1998.

W Paul Segars, G Sturgeon, S Mendonca, Jason Grimes, and Benjamin MW Tsui. 4d xcat phantom for multimodality imaging research. *Medical physics*, 37(9):4902–4915, 2010.

Thomas Seidel, J-C Edelmann, and Frank B Sachse. Analyzing remodelling of cardiac tissue: a comprehensive approach based on confocal microscopy and 3d reconstructions. *Annals of biomedical engineering*, 44:1436–1448, 2016.

Gen Shinohara, Kiyozo Morita, Masato Hoshino, Yoshihiro Ko, Takuro Tsukube, Yukihiro Kaneko, Hiroyuki Morishita, Yoshihiro Oshima, Hironori Matsuhisa, Ryuma Iwaki, et al. Three dimensional visualization of human cardiac conduction tissue in whole heart specimens by high-resolution phase-contrast ct imaging using synchrotron radiation. *World J. Pediatr. Congenit. Heart Surg.*, 7(6):700–705, 2016.

J N Skepper and V Navaratnam. Ultrastructural features of left ventricular myocytes inactive and torpid hamsters compared with rats: a morphometric study. *J. Anat.*, 186(Pt 3):585â€“592, 1995.

Mathangi Soundararajan and Suresh Kannan. Fibroblasts and mesenchymal stem cells: Two sides of the same coin? *Journal of cellular physiology*, 233(12):9099–9109, 2018.

Georg Spinner. *Magnetic Resonance Intravoxel Incoherent Motion Mapping in Heart and Brain.* PhD thesis, ETH Zurich, 2019.

Georg R Spinner, Christian T Stoeck, Linda Mathez, Constantin von Deuster, Christian Federau, and Sebastian Kozerke. On probing intravoxel incoherent motion in the heart-spin-echo versus stimulated-echo dwi. *Magnetic resonance in medicine*, 82(3): 1150–1163, 2019.

Luc St-Pierre, Eva HÃ©riprÃ©, Marie Dexet, Jérôme CrÃ©pin, Graciela Bertolino, and Nicolas Bilger. 3d simulations of microstructure and comparison with experimental microstructure coming from oim analysis. *Int. J. Plast.*, 24(9):1516–1532, 2008.

Edward O Stejskal and John E Tanner. Spin diffusion measurements: spin echoes in the presence of a time-dependent field gradient. *The journal of chemical physics*, 42 (1):288–292, 1965.

Daniel D Streeter Jr, Henry M Spotnitz, Dali P Patel, JOHN Ross Jr, and Edmund H Sonnenblick. Fiber orientation in the canine left ventricle during diastole and systole. *Circ. Res.*, 24(3):339–347, 1969.

Andrew M Stuart and AT Peplow. The dynamics of the theta method. *SIAM journal on scientific and statistical computing*, 12(6):1351–1372, 1991.

Yi Su, Liang Zhong, Chi-Wan Lim, Dhanjoo Ghista, Terrance Chua, and Ru-San Tan. A geometrical approach for evaluating left ventricular remodeling in myocardial infarct patients. *Comput. Methods Programs Biomed.*, 108(2):500–510, 2012.

Karri Suvila and Teemu J Niiranen. Interrelations between high blood pressure, organ damage, and cardiovascular disease: no more room for doubt, 2022.

Woo-Suk Tae, Byung-Joo Ham, Sung-Bom Pyun, Shin-Hyuk Kang, and Byung-Jo Kim. Current clinical applications of diffusion-tensor imaging in neurological disorders. *Journal of Clinical Neurology*, 14(2):129–140, 2018.

Irvin Teh, Darryl McClymont, Rebecca AB Burton, Mahon L Maguire, Hannah J Whittington, Craig A Lygate, Peter Kohl, and Jürgen E Schneider. Resolving fine

cardiac structures in rats with high-resolution diffusion tensor imaging. *Sci. Rep.*, 6: 30573, 2016.

Anh Phong Tran, Shijie Yan, and Qianqian Fang. Improving model-based functional near-infrared spectroscopy analysis using mesh-based anatomical and light-transport models. *Neurophotonics*, 7(1):015008, 2020.

Wen-Yih I Tseng, Van J Wedeen, Timothy G Reese, R Neal Smith, and Elkan F Halpern. Diffusion tensor mri of myocardial fibers and sheets: correspondence with visible cut-face texture. *J. Magn. Reson. Imaging.*, 17(1):31–42, 2003.

Valerie Phi Van, Franca Schmid, Georg Spinner, Sebastian Kozerke, and Christian Federau. Simulation of intravoxel incoherent perfusion signal using a realistic capillary network of a mouse brain. *NMR in Biomedicine*, 34(7):e4528, 2021.

Lihui Wang, Yue-Min Zhu, Hongying Li, Wanyu Liu, and Isabelle E Magnin. Simulation of diffusion anisotropy in dti for virtual cardiac fiber structure. In *International Conference on Functional Imaging and Modeling of the Heart*, pages 95–104. Springer, 2011.

Lihui Wang, Yuemin Zhu, Hongying Li, Wanyu Liu, and Isabelle E Magnin. Multiscale modeling and simulation of the cardiac fiber architecture for dmri. *IEEE Trans. Biomed. Eng.*, 59(1):16–19, 2012.

Jean-Luc Wautier and Marie-Paule Wautier. Vascular permeability in diseases. *International Journal of Molecular Sciences*, 23(7):3645, 2022.

Feng Wei, Tingzhong Wang, Juanjuan Liu, Yuan Du, and Aiqun Ma. The subpopulation of mesenchymal stem cells that differentiate toward cardiomyocytes is cardiac progenitor cells. *Experimental cell research*, 317(18):2661–2670, 2011.

Harlan F Weisman, David E Bush, John A Mannisi, and Bernadine Healy Bulkley. Global cardiac remodeling after acute myocardial infarction: a study in the rat model. *J. Am. Coll. Cardiol.*, 5(6):1355–1362, 1985.

Christos G Xanthis, Ioannis E Venetis, AV Chalkias, and Anthony H Aletras. Mrisimul: a gpu-based parallel approach to mri simulations. *IEEE Transactions on Medical Imaging*, 33(3):607–617, 2013.

Andriy Yabluchanskiy, Yonggang Ma, Ying Ann Chiao, Elizabeth F Lopez, Andrew P Voorhees, Hiroe Toba, Michael E Hall, Hai-Chao Han, Merry L Lindsey, and Yu-Fang Jin. Cardiac aging is initiated by matrix metalloproteinase-9-mediated endothelial dysfunction. *American Journal of Physiology-Heart and Circulatory Physiology*, 306 (10):H1398–H1407, 2014.

Qiang Yu, David Reutens, Kieran O'Brien, and Viktor Vegh. Tissue microstructure features derived from anomalous diffusion measurements in magnetic resonance imaging. *Human brain mapping*, 38(2):1068–1081, 2017.

Xingxing Zhang, Carson Ingo, Wouter M Teeuwisse, Zhensen Chen, and Matthias JP van Osch. Comparison of perfusion signal acquired by arterial spin labeling–prepared intravoxel incoherent motion (ivim) mri and conventional ivim mri to unravel the origin of the ivim signal. *Magnetic resonance in medicine*, 79(2):723–729, 2018.

Pingzhu Zhou and William T Pu. Recounting cardiac cellular composition, 2016.

Guangming Zhu, Christian Federau, Max Wintermark, Hui Chen, David G Marcellus, Blake W Martin, and Jeremy J Heit. Comparison of mri ivim and mr perfusion imaging in acute ischemic stroke due to large vessel occlusion. *International Journal of Stroke*, 15(3):332–342, 2020.